

# Journal Pre-proof

A comprehensive review: Discussed the effect of high-entropy alloys as reinforcement on metal matrix composite properties, fabrication techniques, and applications

Vivek Pandey, R Seetharam, H. Chelladurai



PII: S0925-8388(24)01682-7

DOI: <https://doi.org/10.1016/j.jallcom.2024.175095>

Reference: JALCOM175095

To appear in: *Journal of Alloys and Compounds*

Received date: 29 February 2024

Revised date: 31 May 2024

Accepted date: 4 June 2024

Please cite this article as: Vivek Pandey, R Seetharam and H. Chelladurai, A comprehensive review: Discussed the effect of high-entropy alloys as reinforcement on metal matrix composite properties, fabrication techniques, and applications, *Journal of Alloys and Compounds*, (2024)  
doi:<https://doi.org/10.1016/j.jallcom.2024.175095>

This is a PDF file of an article that has undergone enhancements after acceptance, such as the addition of a cover page and metadata, and formatting for readability, but it is not yet the definitive version of record. This version will undergo additional copyediting, typesetting and review before it is published in its final form, but we are providing this version to give early visibility of the article. Please note that, during the production process, errors may be discovered which could affect the content, and all legal disclaimers that apply to the journal pertain.

© 2024 Elsevier B.V. All rights are reserved, including those for text and data mining, AI training, and similar technologies.

**A comprehensive review: Discussed the effect of high-entropy alloys as reinforcement on metal matrix composite properties, fabrication techniques, and applications**

Vivek Pandey<sup>1\*</sup>, R Seetharam<sup>2</sup>, H. Chelladurai<sup>1</sup>

<sup>1</sup>*Severe Plastic Deformation Laboratory, Department of Mechanical Engineering,*

*PDPM Indian Institute of Information Technology Design and Manufacturing Jabalpur-482005, India*

<sup>2</sup>*Department of Mechanical Engineering, Indian Institute of Information Technology Design and Manufacturing Kurnool-518008, India*

\*Email: 22pmeo04@iiitdmj.ac.in

**Abstract:**

In research, high-entropy alloy-reinforced metal matrix composites (HEAs-MMCs) have attracted academicians, researchers, and scientists to achieve extraordinary properties unobtainable by ceramic-reinforced metal matrix composites. HEAs have potential to improve the properties of weak metal matrices due to their superior properties such as high strength, stability in high-temperature applications, improved corrosion, and wear resistance. HEA has novel properties over conventional alloy system including exceptional performance at high temperatures, improved mechanical properties in cryogenic environments and high strength with ductility. The rapidly evolving needs of industries require high-performance materials, and HEA-MMCs are suitable for fulfilling the demands of newly established application fields. In this review article, the author discusses fabrication methods, microstructural evolution, mechanical, wear, thermal, electrical and corrosion properties, effects of heat treatment and strengthening mechanisms of HEA-MMC materials. HEA-MMC is suitable for large-scale and mass production with complex and precise HEA-MMC parts fabricated by commercialization of the casting process and additive manufacturing technology. The core-shell structure is formed by the diffusion action between the matrix and the reinforced and acts as a transition layer, leading to an improvement in mechanical properties. Finally, from the strengthening mechanisms, it was concluded that fine grain strengthening, Orowan strengthening and coefficient of thermal expansion (CTE) imbalanced strengthening mechanisms were more effective than others in improving properties. At the end of the review paper, the main importance, applications, challenges and perspectives of HEAs-MMCs are discussed, which will help the development of advanced materials with improved performance that can increase progress and innovation in the scientific community.

**Keywords:** HEAs-MMCs, Interdiffusion layer, Core-shell Structure, Corrosion, Wear and Strengthening Mechanism

**1. Introduction:**

The economic success of any country is mainly dependent on its industrial development. Due to globalization, any industry in our country is expected to be global market standard. For the above reason, our Indian product should be of very high quality, and this can be done through new and advanced materials

with enhanced properties. Over the past 7000 years, from the copper age on, alloys have been cast [1]. Metal has played an important role in human life since that time, but the pure form of metal has never been true for engineering applications. As man's lifestyle improves, it becomes necessary to use stronger, harder, and better materials. Thus, alloy fabrication takes shape so that one can get enhanced property materials. At the earlier stages of metallurgy, the development of alloys contains one principal element as a matrix. This matrix acts as a host for alloying metals that improve the properties of the base metal [2]. Thus, conventional alloying design systems are composed of single or double principal elements with other minor elements and are also called low-entropy alloys [3][4]. Among such traditional alloys are aluminum, copper, iron, and nickel used to form alloys. Furthermore, metal-matrix composites have attracted much attention for the properties and performance improvements of the matrix. Mainly, aluminum alloys have attracted the attention of researchers due to their extensive use in industries. Based on the single principal element system, bulk multi-component alloys were fabricated with amorphous phases. This study is due to the need for improvements in the properties of composites, such as high wear and corrosion resistance, strength improvement, and high fatigue, impact, and hardness.

The HEAs have exhibited superior mechanical properties, excellent wear and corrosion resistance, good stability at elevated temperatures, and high fatigue and fracture resistance as compared to conventional alloys [5][6][7][8]. Moreover, a wide variety of properties and microstructures have been found due to different compositions and processing routes; now, the HEAs have become the most desirable research as well as industrial application fields to work on. Research is being done to find better composites in three directions: one is the fabrication of new compositions, the second is the standardization of new processes for fabrication, and the third is the combination of new combinations and processes [9]. It is the new way to develop alloys with multiple principal elements in equimolar or near-equimolar ratios. This new type of alloy design is known as high-entropy alloys (HEAs). The new concept of alloy formation came into existence in 2003, when S. Ranganathan (India) [10] remembered panchaloha (alloys of five metals) and ashtadhatu (alloys of eight metals) in his paper. Also, in 2004, Jien-Wei Yeah (Taiwan) and Brian Cantor (United Kingdom) published fundamental papers for high entropy alloys (HEA), and then they became popular with the name of multi-principal element alloys (MPEAs), or "high entropy alloys (HEA)."

In 2004, a change was adopted by metallurgists for the development of alloys. At that time, Cantor et al. [9] from the United Kingdom studied multicomponent ( $Fe_{20}Cr_{20}Mn_{20}Ni_{20}Co_{20}$ ) alloys of equiatomic proportions and found the FCC phase. Also, Jien-Wei Yeh et al. [3] from National Tsing Hua University, Taiwan define High Entropy Alloys (HEAs) as the alloys in which participating principal elements are five or more in equiatomic or near equi-atomic scale. One can design multiple alloys by taking concentration of each element in between 5 to 35 % in weight. **Fig. 1** represents the alloying system in both conventional and HEAs. The size of black circles are principal elements in conventional alloy and red, yellow, and blue circles are other elements whereas in HEA system black, red, yellow, and blue circles are principal elements but in the range of 5 to 35 vol% of whole alloy.

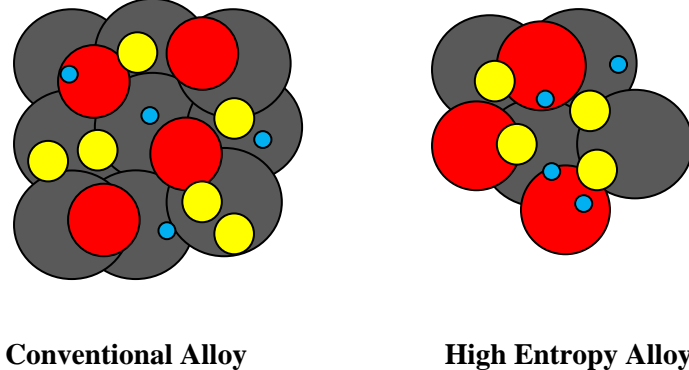


**Fig. 1** Alloy design in conventional and High Entropy Alloy (HEA) system

Eighteen years have passed since these initial papers on HEAs and researchers have published more than 12000 papers on HEAs. Based on year wise publications on HEAs, it is clear that HEAs got much attention after 2014 and is a growing research topic among researchers. These papers cover HEAs fundamental, their fabrication methods, microstructure, and properties (mechanical) evaluation. So many databases are now available for HEA in review papers [11–15]. Some of the research articles are published focusing on special HEAs itself. N.D. Stepanov et al. [16] and Sun et al. [17] reported mechanical properties of CoCrFeNiMn based HEA. Yih-Farn Kao et al. [18] studied microstructure and mechanical properties of  $\text{Al}_x\text{CoCrFeNi}$  in  $x$  from 0 to 2 at as-cast, homogenized and cold rolled conditions. Books are also published on HEA by Dr.BS Murty [19] and MC Gao et al. [20]. Resent studies have been performed on the catalyst nature of HEA by Dohun Kim et al. [21] and Sejin Im et al. [22]. Some of the researchers Iso focused on different methods of manufacturing HEAs. These processing methods of fabricating HEA-MMC are discussed in the following successive sections.

Mixed metal nanocomposites show improved properties compared to composite materials, and the method of mixing mixed metal nanocomposites has a key role in the field of MMCs. Dippong et al [23–26] have done a lot of work in this field with the sol-gel method. Dippong et al. [27] studied the effect of heat treatment annealing process on  $(\text{Co}_{0.4}\text{Mn}_{0.6}\text{Fe}_2\text{O}_4)_\delta (\text{SiO}_2)_{100-\delta}$  ( $\delta = 0\text{--}100\%$ ) nanocomposites, developed by a well-established sol-gel method. Structural and magnetic properties were evaluated by adding ferrite content in silica. The particle size increases from 2 to 74 nm at higher annealing temperatures with higher ferrite content. Similarly, Marcela Stoia et al. [28] performed studies of temperature on  $\text{Co}_2\text{SiO}_4/\text{SiO}_2$  nanocomposite prepared by sol-gel method too and M. tefanescu et al. [29] studied the properties of cobalt oxides nanoparticles.

In this paper the history and development of HEA is studied. From the beginning of a single major element alloy to a multi-major element alloy called HEA, this alloy has gone through various alloy design stages. Now HEA-MMC is new research interest area in the field of HEA. Further this paper describes the detailed processing methods and running parameters of HEA-MMCs. The mechanisms involved in these methods are also explained for better understanding. The microstructural analysis of these different HEA-composites

has been studied. The enhancement found in mechanical properties like hardness, strength, corrosion, wear, thermal and electrical properties of composite were examined. The heat treatment effect on HEA-MMC and findings of that is described. At the end the strengthening mechanism of HEA-MMC is explained. The summary, future scope, and conclusions are discussed at the end of this paper.

The prime novelty of this work is to determine the structural morphology of HEA reinforcement-based composites with different metal matrices formed by different processing methods. An effort has been made to increase the understanding of the research community on the characterization study of HEA-matrix interfaces such as core-shell structure, diffusion layer and interface layer. Relationship of microstructure with physical, mechanical, chemical, tribological, electrical and thermal properties of composites. On the other hand, heat treatment affects the microstructure of the alloy. Discussion of the strengthening mechanism behind the improvement of mechanical properties. Ultimately, this review paper tries to find the research gaps written in the future scope section based on the literature available in open source.

## 2. Processing Methods of HEA-MMCs:

Multiple researchers have used many methods to fabricate Al-HEAs MMCs. Some methods get popularity on feasibility and demand such as powder metallurgy, microwave sintering, stir casting, additive manufacturing, laser powder bed fusion, spark plasma sintering, submerged friction stir processing. The processes that are used for fabrication purposes of HEAs-MMCs are shown in **Fig. 2**

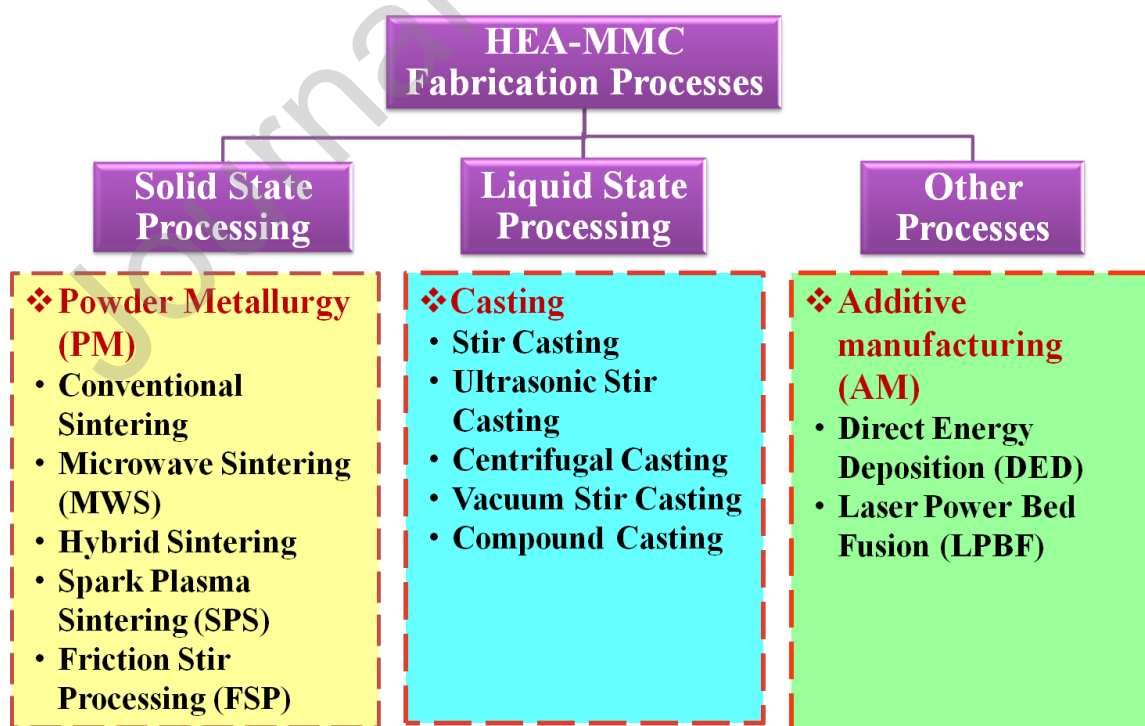


**Fig. 2** Different Fabrication routes of HEA-MMCs

## 2.1 Solid State Processing:

It is the fabrication process of metal matrix composite (MMC) in which dispersion phase particles diffuse with the matrix phase of composite in a solid state under pressure at some elevated temperature. This can be done by powder metallurgy process, which contains conventional sintering, microwave sintering and hybrid sintering. Selected field sintering, hot isostatic pressing, spark plasma sintering, and submerged friction stir processing techniques can also be used to facilitate the fabrication of metal matrix composite.

### 2.1.1 Powder metallurgy (PM) methods

#### *(I) Conventional sintering*

In the PM method of composite fabrication both matrix and reinforcement are involved as a powder in the initial stage. Firstly, the synthetization of HEAs with equal or near equal amounts of atomic weight takes place in ball milling. A suitable ball to powder ratio was taken at suitable rpm for the ball milling process. The material of the ball can be stainless steel or chrome steel in a steel bottle. Only a few studies have countered the effect of process control agents, such as acetone, ethanol [30], or toluene, which are used to prevent oxidation and cold welding of powders with the inner surface of the crystal along with the ball. A longer blending time reduces the particle size of powders and improves the wetting of reinforcement with the matrix. The XRD results with high blending time show the lower and broader peaks of intensity [31,32] which confirm equal particle size of elements. The compaction of blended powders done under the die and punch assembly. Ananiadis et al. [33] has applied 7.6 tons used to make a 14 mm diameter cylindrical pellet and Prabakaran et al. [32] used a compaction load of 650 MPa in die and punch assembly to obtain green compact parts. Sintering of cold compacted parts done below the melting point of the matrix, Ananiadis et al. [33] used 550°C for AA-1050 aluminum powder. The sintering can be done by conventional heating from a furnace or through a microwave furnace or a combination thereof as required. The standard polishing procedure was used for characterization of samples and further study such as mechanical and tribological etc. are carried out. The **Fig. 3** represents the process of powder metallurgy method of material fabrication.

Chen et al. [31] prepared AlCoNiCrFe HEA reinforcement and fabricated Cu-HEA metal matrix composite through a powder metallurgy route. The Al, Co, Ni, Cr and Fe were selected in equiautomic composition with 99.5% purity and  $\leq 60\mu\text{m}$  particle size. A rotational speed of 300 rpm and a ball-to-powder ratio of 15:1 is selected for ball milling and the powder is tested every 6 hours for XRD analysis for up to 60 hours. The finer 10 and 20 wt. % HEA powder reinforcements were mixed with Cu powder for 3 hrs at 250 rpm to fabricate the Cu-HEAs MMC composite. The sintering is performed for composite and pure copper powders for 30 min. at 800°C and microstructure was analyzed by SEM and TEM and EDS was used to identify chemical composition and the phase of elements was determined by the XRD examination.

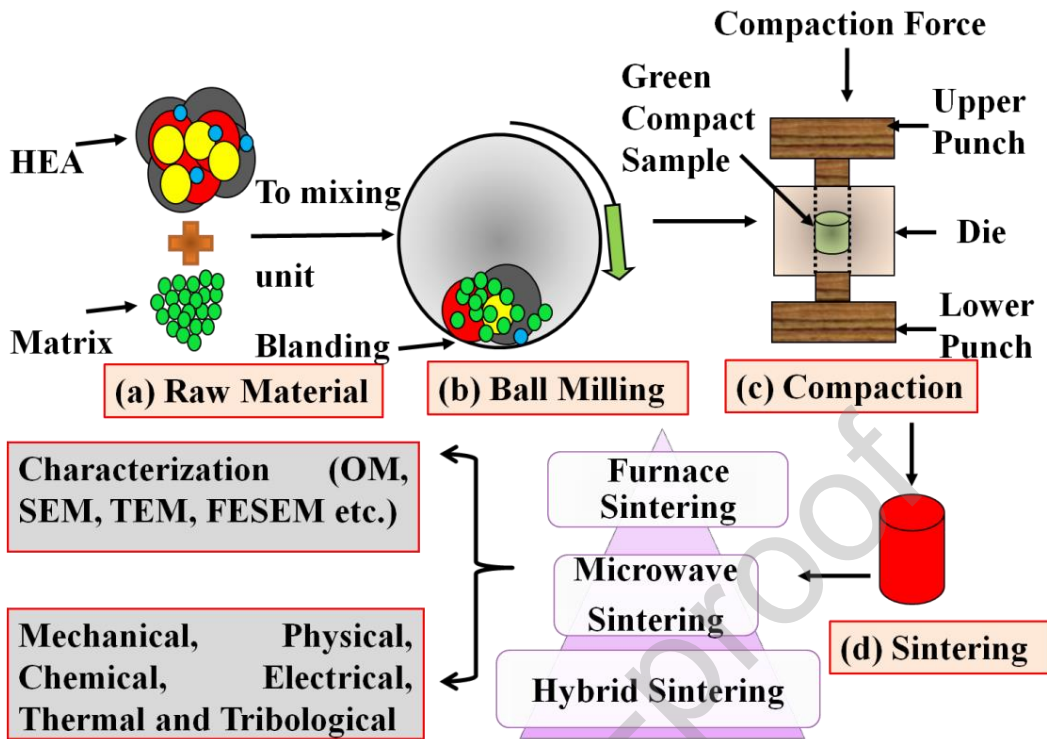


**Fig. 3** Powder Metallurgy Process for HEA-MMC

## (II) Microwave sintering (MWS)

**(a) Introduction of MW:** The electromagnetic waves that have a range of wavelength from 1m to 1mm or 300 MHz to 300 GHz are known as microwave (MW). The use of microwaves started from food processing [34] and now it is widely applied in the field of materials. Materials like polymers, ceramics [35], metal and different composites [36] can also be facilitated by microwaves. Microwave sintering shows presence in metal matrix composites like Dinesh Agrawal [37] studied ceramic, glass, metallic materials and composite for sintering with microwaves. Microwaves can be used for sintering of pure metal powders [38]. The application of microwaves in the materials field extends from sintering to cladding, joining, welding, casting, and coating. Industries such as polymer [39], pharmaceutical, chemical and wood processing [40] are using established microwave technology. The microwave sintering process is also environmentally friendly as it is a fast process, time saving energy efficient and thus cost effective. The microwave sintering parameters such as ball-to-powder ratio, milling speed in rpm and milling time are the same as powder milling technique, the only difference being the sintering technique. Wang et al. [30] fabricated Al-HEA MMC by mechanical alloying and sintering in a low-temperature microwave. To obtain the green compact the dry powders were cold compacted through isostatic pressing for 2 min. at the static pressure of 300 MPa. A microwave sintering furnace was set for 2 kW output power to sinter the green compaction and an operating frequency of 2.45 GHz at a temperature of 460°C for different sintering times of 20, 30, 40, 50 and 60 minutes was set to study the effect of different sintering temperature.

**(b) Comparison between conventional and microwave processes:** From the initiation of microwave energy, microwave processing has been initiated and found to be advantageous over using traditional processes. The high densification, enhancement in mechanical, corrosion, and tribological properties, less processing time, choice of different processing modes, the fine grain structure of the processed material, diffusion on the surface, and the requirement of less space are some advantages of microwave processing (MWP) over the conventional processing. Oghbaei et al. briefly reviewed the advantages, fundamentals, and application of conventional and microwave sintering (MWS) [41].

The use of microwaves in the sintering process of material processing offers advantages such as efficiency, cost-effectiveness and environmental impact compared to traditional methods [42] . After the year 2000, MWS became popular in the field of ceramics, polymers and semiconductors as well as metals. In conventional sintering method after obtaining a green compacted part the object is placed in an electric or resistance furnace or a fossil fuel furnace for indirect sintering. But this includes the cost of heating elements, inner lining of refractory materials and electric power or fuel for prolonged heating to maintain uniform temperature in the furnace. The efficiency of the whole system is reduced due to indirect heating, because first the internal volume of the furnace is heated, and then the object is heated by conduction, convection and radiation. Therefore, the time taken in conventional sintering is much longer as compared to direct heating in microwave sintering. Direct heating in microwave sintering starts at the atom level of an object and takes much less time. It saves energy and makes the process cost effective as well as environment friendly as no hazardous material and scraps are generated after processing. Environmental damage and energy loss are minimal. The microwave sintering process is now approved for all types of materials in all applications filed.

Conventional sintering of material occurs when three modes of heat transfer conduction, convection and radiation take place. The direction or effect of heating starts from the surface of the sample to the interior, because in conventional sintering the entire chamber of the furnace is first heated and then the heat *AM is about layer-by-layer* transfer takes place. On the other hand, the MWS process occurs when molecules of material absorb electromagnetic energy. The heating of a material is due to vibration of molecules initiated by electromagnetic energy. The overall heating takes place from the core to the surface of the material and this improves the diffusion of the surface and thus the density of the material is improved due to the bonding of the particles and porosity is reduced. **Fig. 4** represents the heating pattern of conventional as well as the microwave processing.

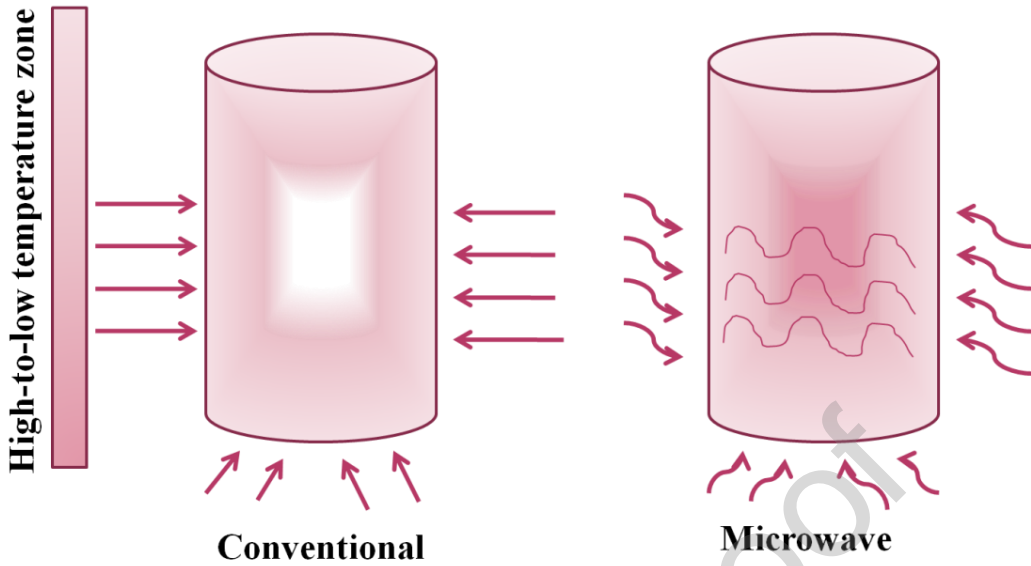


**Fig. 4** Schematic of heating pattern in conventional and microwave mode.[43]

Difficulty in casting materials, after solidification control of grain structure along grain boundaries for mechanical properties, are some of the drawbacks of conventional casting. In microwave casting (MWC) the metals absorbed the microwave energy and thus this energy melts the metal, thereby improving the bond between particles. Better incorporation of reinforcement into the matrix results in improved casting compared to conventional casting. The proper frequency level and intensity of the electromagnetic force control the skin depth of the MWC and this skin depth is the root phenomenon capability of MWC process. Sharma et al. [44,45] use an in-situ microwave casting process with 2.45 GHz frequency and 1400 W electromagnetic energy. Currently for increasing production rate this microwave processing is used in all manufacturing processes such as casting, welding, cladding, coating, joining, sintering, and finished cutting, due to shorter processing time, instead of conventional processing.

**(c) Progress in technique of microwave for metal materials:** Fig. 5 shows the year in which modification happens in microwave processing for metals. The high heating rate was achieved for electrically conductive metals until 1979 and complete sintering with microwave was reported in 1999 [46], cladding to brazed materials in 2005, for melting bulk metal and metal powders, brazing was achieved in 2006, casting of ceramic and metal coating in 2008, similar and dissimilar bulk metal joining by microwave in 2009, drilling of sheet metals in 2012 and bulk metal/sheet metal casting done at 2013.

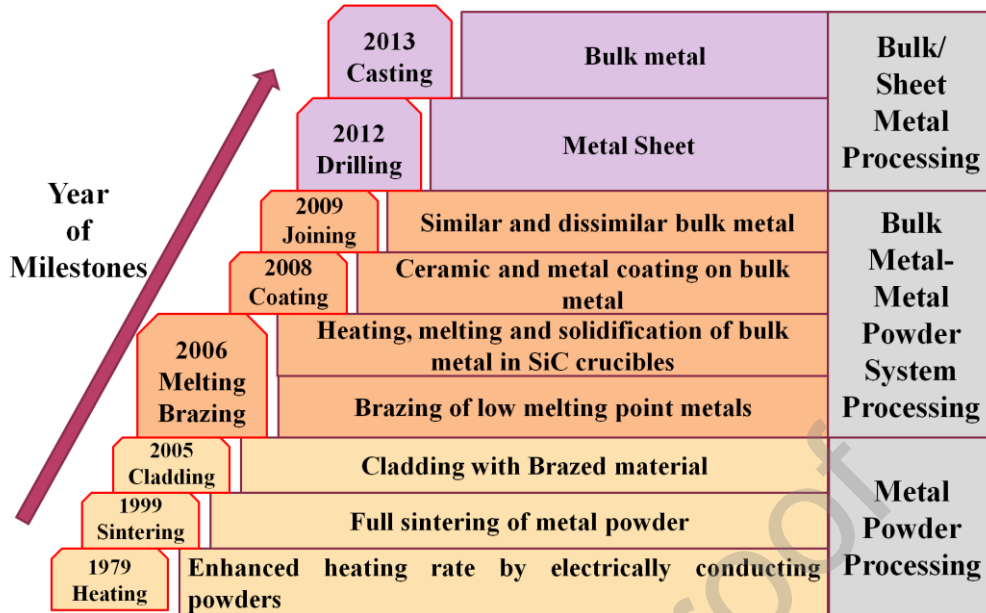


**Fig. 5** Microwave techniques developed for different metal materials [45]

**(d) Mechanism of microwave sintering (MWS):** Sintering is a process in which a blended, compacted green part is heated by any mode of heating below 70 to 80 % of its melting point ( $T_m$ ) or near ( $T_m$ ). MWS heats the material volumetrically in all directions so that a finer microstructure and better properties are obtained. A microwave cavity is used to hold the compacted part. A transparent material is used between the compact sample and the cavity to avoid direct contact with the microwave radiation.

The skin depth is the penetration of microwave in material which causes uniform heating of material. The microwave penetrates the material and heats the material at the molecular level, resulting in a uniform distribution of temperature at and within the mating surface of the material. The skin depth is known as the penetration depth of the microwave from the surface of material. The skin depth ( $\delta$ ) depends on the frequency of microwave ( $f$ ) in Hz, Magnetic permeability ( $\mu$ ) in H/m, and electrical conductivity ( $\sigma$ ) in S/m and is given by the following relation as:

$$\delta = \frac{1}{\sqrt{(\pi f \mu \sigma)}} \quad (1)$$

The skin depth can be defined as the depth of microwave penetration from the surface of the material where the current density drops to 36.79% of its surface. It is a phenomenon divided into three categories based on the depth of penetration materials; (i) low penetration-microwave reflectors due to conductor materials reflecting MW and do not absorb MW ex. All bulk metals, (ii) medium penetration- microwave absorber; due to dielectric materials which absorb MW ex. water and SiC (iii) high penetration- microwave transparent; due to insulating material property low loss of MW happen and MW doesn't absorb; get passed ex. Quartz and Teflon.

There is another category of composite absorbent material such as multicomponent composites, HEAs, or composites such as MMC, PMC and CMC in which some phases have low dispersion (conductors), some phases have medium penetration (absorber) and some phases have high penetration (transparent) property and these are called advanced materials. **Fig. 6** is a pictorial representation of a reflector, absorber, and transparent material under microwave heating.

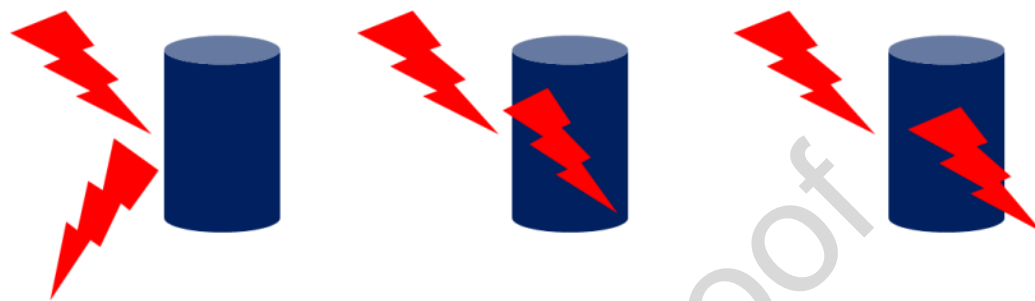


**Fig. 6** Behavior of material with microwave as reflector, absorber, transparent

(e) **Flow process of microwave sintering (MWS):** The MWS process for any material generally involves three steps (a) blending (2) compaction and (3) sintering. The selected ratio or weight % matrix and reinforcement for MMC fabrication are weighed in an electronic weighing machine and blending done in planetary ball mill to achieve uniform mixing and fine powder. The green compaction is done in dies and punches assembly by hot or cold compaction procedure and then proceeds to sintering process. Sintering can be done by using a susceptor material to perform pure microwave sintering or hybrid microwave sintering. High penetration of MW, densification, and diffusion rate are some advantages of hybrid microwave sintering over microwave sintering. To improve the properties of the sintered materials secondary processes such as extrusion, rolling, etc. will be performed. The characterization studies such as optical microscopy (OM), scanning electron microscopy (SEM), transmission electron microscopy (TEM) etc. done to analysis the morphology of material and evaluated by property evaluation by different tests. Tensile and compression tests for physical, surface roughness tests and corrosion tests used for chemical property evaluation and process are shown in **Fig.7**.

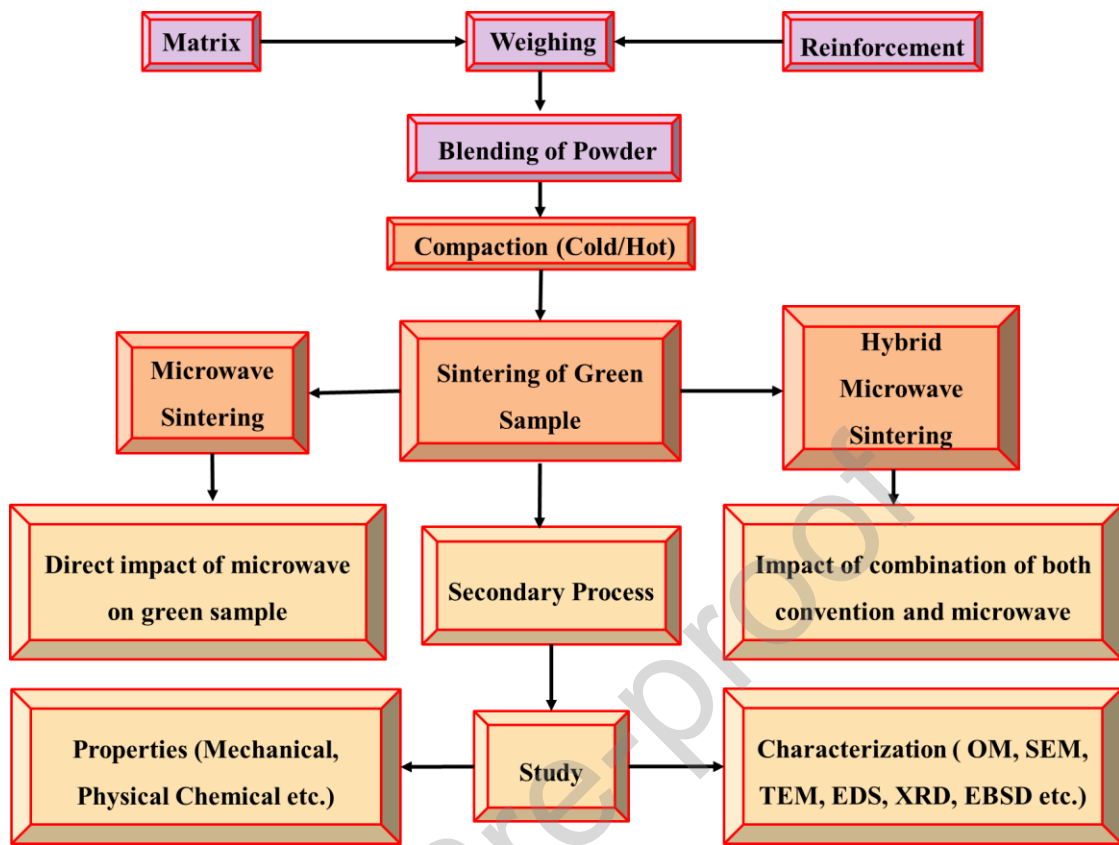


**Fig. 7** Flow diagram of microwave sintering process (MWS)

**(III) Microwave Hybrid Heating:** The use of hybrid heating instead of microwave heating has increased the uniformity of heating. Hybrid microwave heating uses a susceptor in which electromagnetic energy is absorbed and converted into heat. These susceptor materials such as graphite, charcoal and silicon carbide are used when a low skin depth sample needs to be sintered. In normal microwave sintering the core of the material starts heating, but the surface takes time to heat up by conduction, however, in conventional heating, the furnace gives heat to the surface part of the material. The overall and uniform heating occurs in combination with both called hybrid microwave heating. This susceptible material absorbs the heat of electromagnetic energy and brings that in the form of heat to the sample surface. The microwave hybrid heating process is shown in **Fig. 8** and **9**.

Hybrid microwave heating of materials using susceptors such as graphite, charcoal and silicon carbide increases the uniformity of heating in processing or sintering compared to microwave heating or conventional heating. Susceptors absorb microwave energy and convert it into heat, which is then transferred to the material being processed [47]. This helps reduce issues like hot spots and temperature gradients, leading to more consistent and predictable processing outcomes. Microwave heating alone may struggle to uniformly heat some materials with high absorption coefficients or low dielectric properties. Adding susceptors with high absorption coefficients such as graphite or silicon carbide hybrid heating improves energy absorption and penetration depth, providing more assurance by heating throughout the material. Overall hybrid microwave heating with susceptors such as graphite, charcoal and silicon carbide represents

a versatile and effective approach to enhance the uniformity of heating in material processing, providing advantages in terms of speed, control and energy efficiency [48].

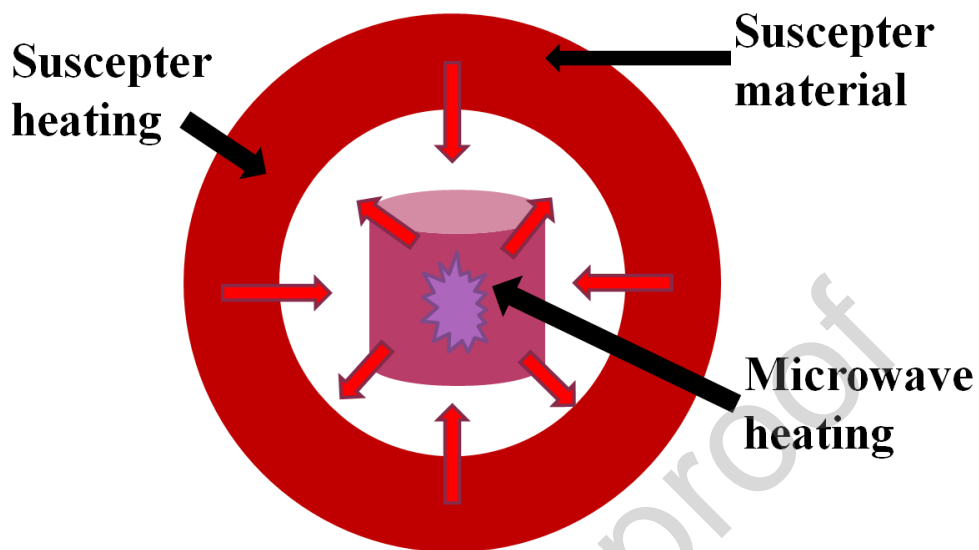


**Fig. 8** Heating phenomenon of hybrid microwave heating.

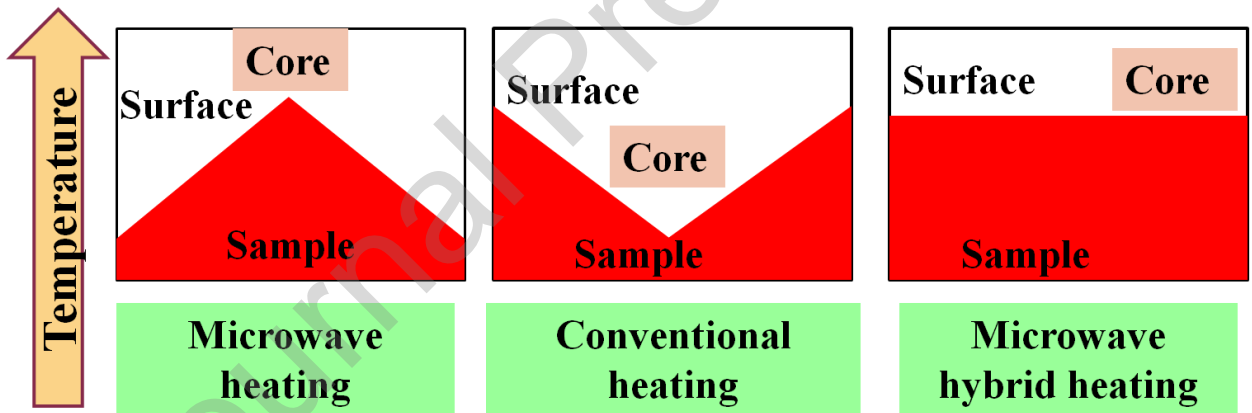


**Fig. 9** Temperature profile of sample when heating in microwave, conventional and hybrid microwave sintering.

### 2.1.2 Spark Plasma Sintering (SPS):

**(a) History and development of SPS:** The concept of the SPS method comes from the first patent, published in 1913 in the US for sintering material by electric current. The SPS method was initiated in 1930 but commercialization did not begin until later in the 1980s, researchers in Japan improved SPS method in laboratories. After 50 years of early stages and 20 patents based on pulse current, Kiyoshi Inoue discovered the theory of "spark sintering". Later commercialization of methods to produce functionally graded material (FGMs), net shaped parts, and production of small and large parts started slowly. After Inoue's patent expired in 1990, Japanese companies began producing SPS machines for industry, notably Sumitomo Coal Mining Co., Ltd. After that, Germany (FCT System GmbH) and USA (Thermal Technology) based on the same DC

pulse current system companies. Now Japan, China, and Korea are also part of the production of SPS machine setup for industries.

**(b) Introduction of SPS:** Spark plasma sintering (SPS) also known as pulsed electric current sintering (PECS) technique is based on powder metallurgy process. It is widely used due to the ease of preparation and time saving of MMC at low temperatures. In this method firstly both HEA and matrix are taken in powder form and mixed by ball milling machine method with the optimum parameters such as ball to powder ratio, ball milling speed and milling time. The powders are placed between an electrically conducting graphite die and uniaxial pressure is applied to the top and bottom of the die and then sintering is performed through high electric current and low voltage supply for 5-20 minutes to obtain uniform sintering. This SPS process is particularly beneficial in hard refractory materials. **Fig. 10** illustrates the methodology of spark plasma sintering (SPS) technique.

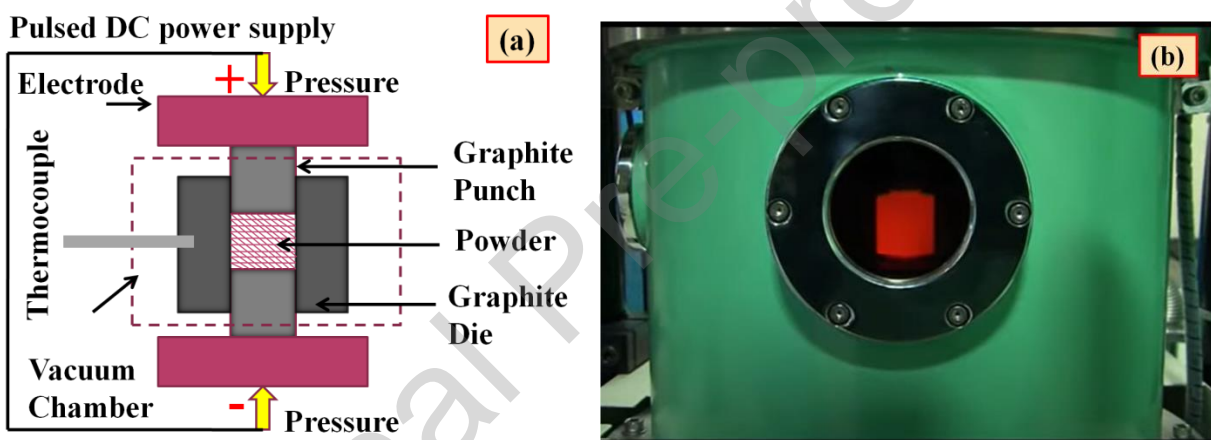


**Fig. 10** (a) Schematic of Spark Plasma Sintering (SPS) and (b) heating of Graphite by DC power supply

**(c) Mechanism of spark plasma sintering:** The mechanism of SPS is totally dependent on sintering of materials. Heat is used for sintering the material produced by direct current and low voltage. The diffusion of particles occurs by producing sparking between particles due to applications of DC current. A DC current supply in the SPS passes through the sample powder and conducts the die causing internal and external heating [49]. The application of external pressure during sintering improves the density of compact powders. A highly dense material can be made by SPS because no grain growth occurs during sintering and no coarse grain is formed. Sintering of nano sized powders without grain growth can be achieved in a very short time.

Various processing theories have been proposed for SPS process modeling, of which the micro spark or microplasma theory is the most popular theory in SPS process molding. The application of DC current generates heat and this initiates a spark between the particles, which brings local high temperatures to the powder particle surface, causing the surface to melt. The particle surface melting causes the particle mating region to start melting in a “neck” shape and with increasing sintering time a cloud of plastic particles is

formed, resulting in highly dense compacted parts. The controlled particle growth is achieved because of the surface heating of particles. The sintering phenomenon is described in **Fig. 11**.

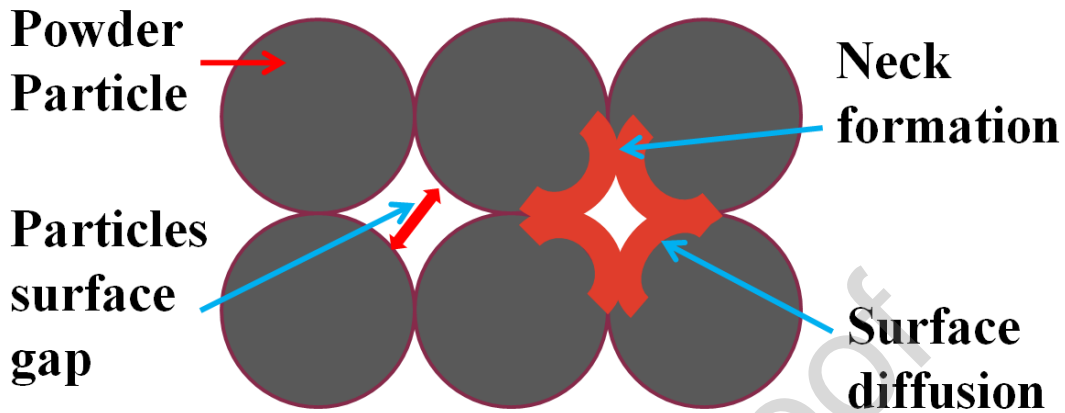


**Fig. 11** Micro spark theory of SPS process

To carry out the SPS process, mainly four steps are required as illustrated in **Fig. 12**. In the first stage, gases are removed and vacuum is created. In the second stage, pressure is applied at the upper punch for compaction of powder and in the third stage resistance heating is provided. The fourth step cools the entire SPS system [50]. In the current state, a spark starts between the particle surface and the interstices of the particles and this raises the temperature of the surface and starts necking between the particles due to melting of the surface. Improvement of heating rate and reduction of sintering time facilitate resistance to grain growth. Applying pressure to the powders filled in the graphite die and in a current flow produces a highly dense or fully dense material with the required mechanical properties.

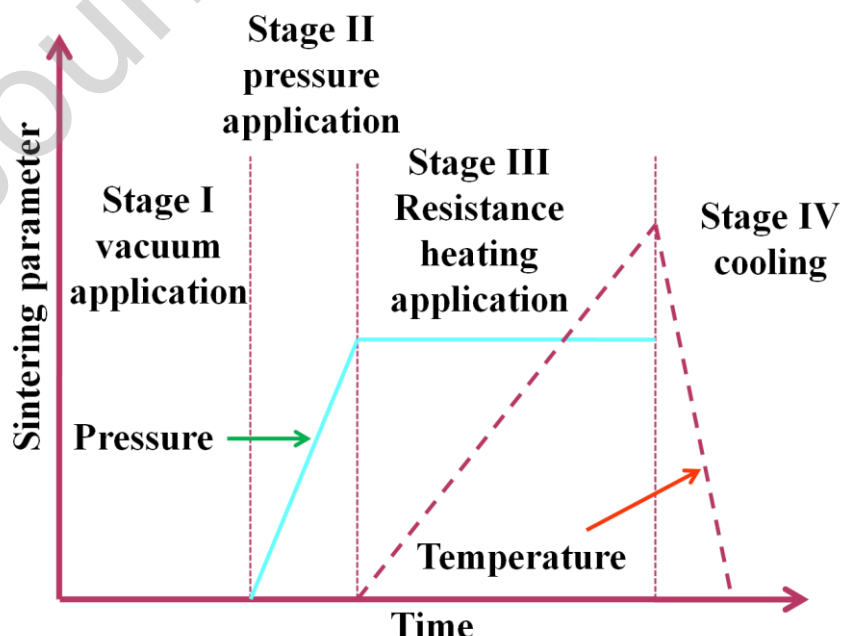


**Fig. 12** Stages in SPS process [50]

### 2.1.3 Submerged friction stir processing (FSP):

Submerged friction stir processing (FSP) is one of the popular solid state processing techniques in the metal matrix composite research field. In this method, the matrix is used as a base material whose property is to be improved and the HEA powder is used as a reinforcement which can be prepared by ball milling or gas atomization method. A series of blind holes (diameter 1.5 mm and depth 4 mm) centered on the matrix plates are machined so that the HEA reinforcement powder resets on them. A flat rotating tool is selected to press the particles so that they do not come out of the matrix pores. After the tool passes a series of blind holes in one direction and then in the opposite direction, it ensures an even distribution of HEA in the matrix. A water circulation system is provided throughout the process, which provides resistance to friction generated during tool workpiece interaction. **Fig. 13** is illustrated the manufacturing process of HEA based reinforcement MMC through submerged friction stir processing (SFSP). Yang et al. [51] performed the submerged friction stir processing on AA-5083 alloys by incorporating the AlCoCrFeNi HEA powder. They revealed that the yield strength (YS) and ultimate tensile strength (UTS) of the AA-5083-HEA composite increased by incorporating HEA reinforcement through submerged friction stir processing (SFSP).

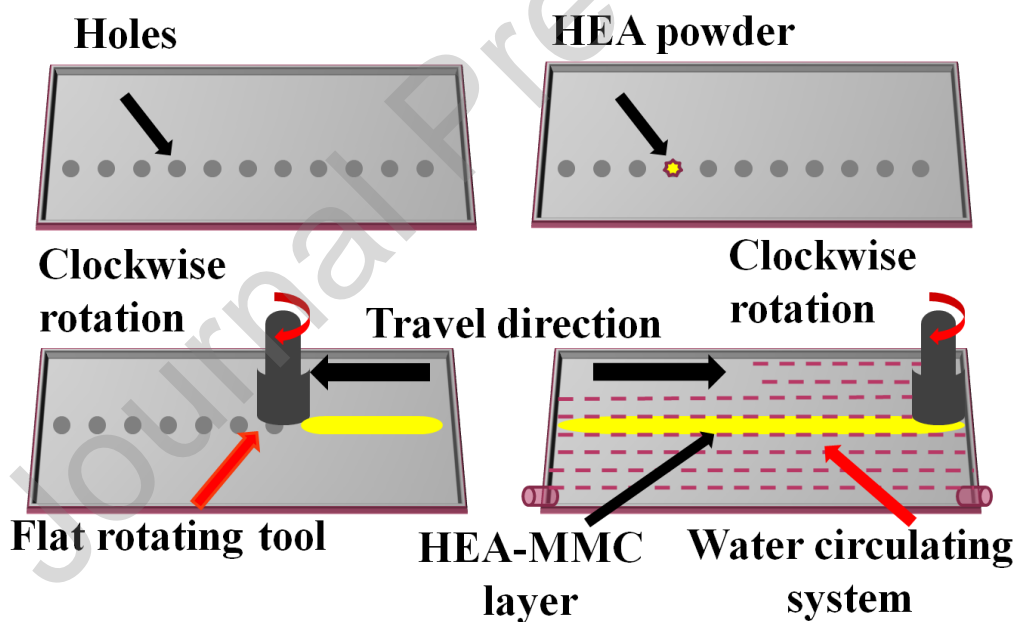


**Fig.13** Manufacturing process of HEA-MMC through submerged friction stir processing (SFSP)

### 2.2 Liquid State Processing

It is a processing technique to make a metal matrix composite in which dispersion phase particles are mixed with a molten metal matrix. This technique works at the liquid state of the matrix and reinforcement and MMC can be fabricated by different casting methods.

### 2.2.1 Stir Casting

The fabrication of MMC can be done by various casting methods, the most popular in the research field are stir casting, ultrasonic stir casting, gravity die casting, vacuum casting, centrifugal casting, and compound casting. In this section, the working mechanism of the casting process i.e. the most popular stir casting is discussed.

In the case of the casting method the ball milling process is not required for the matrix component, however, it is required for mixing the HEA powder prior to incorporation into the molten matrix. Li et al. [52] and Luo et al. [53] used the conventional casting methods to fabricate  $\text{Al}_{0.5}\text{CoCrFeNi}$  AA2024–HEAp MMC. They found that the wettability of the aluminium- $\text{Al}_{0.5}\text{CoCrFeNi}$  composite (between matrix and reinforcement particles) was enhanced. In the casting process, the matrix phase is selected as billet and HEAp in powder form. The metal is heated in the crucible by an electric resistance furnace above its melting point so that it is completely melted, and then the preheated HEAp powder will be added to the molten metal. A mechanical stirrer with two, three or four rectangular or circular blades was used to stir the material for 2–4 min so that uniform mixing of the HEA in the matrix was obtained. The furnace temperature selected by various researchers for aluminum is 850°C until complete melting. Molten MMC was poured into a preheated die and left to solidify. The obtained ingots can be homogenized below the melting point for 8–10 h to remove the internal stresses that occur during casting of the metal. The stir casting procedure of HEA-MMC is shown in **Fig. 14**.

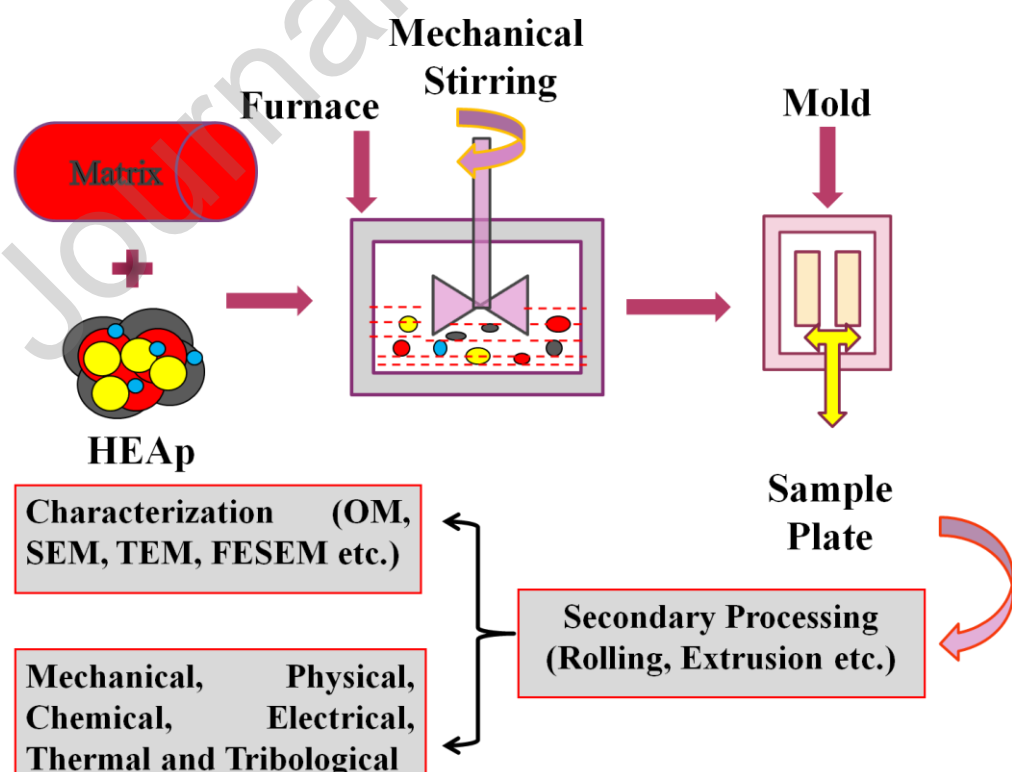


**Fig. 14** Stir casting process of HEA-Metal Matrix Composite (MMC) fabrication

### 2.2.2 Ultrasonic Stir Casting:

It was observed by the researchers that after stir casting all the agglomeration, clustering, sedimentation, and uneven distribution of particles take place in the matrix. This problem can be overcome by using an ultrasonic probe-assisted stir-casting method. The ultrasonic-assisted stir casting method uses an ultrasonic probe that generates ultrasonic waves on the molten metal pool and breaks up the agglomerated reinforce particles as result of this uniformity of MMC can be achieved. Zhang et al. [42, 43] used ultrasonic stir casting process to fabricate the HEA-AMMC composite. Mechanical stirring was performed in a furnace at a rotation speed of 300 rpm for 5–10 min, and an external preheated ultrasonic (UT) probe was inserted into the molten pool with an ultrasonic frequency of 19–22 kHz and 400 W output power. The schematic diagram of the processes of UT probe assisted stir casting is illustrated in **Fig. 15**. The other process parameters and process will remain same as normal casting process.

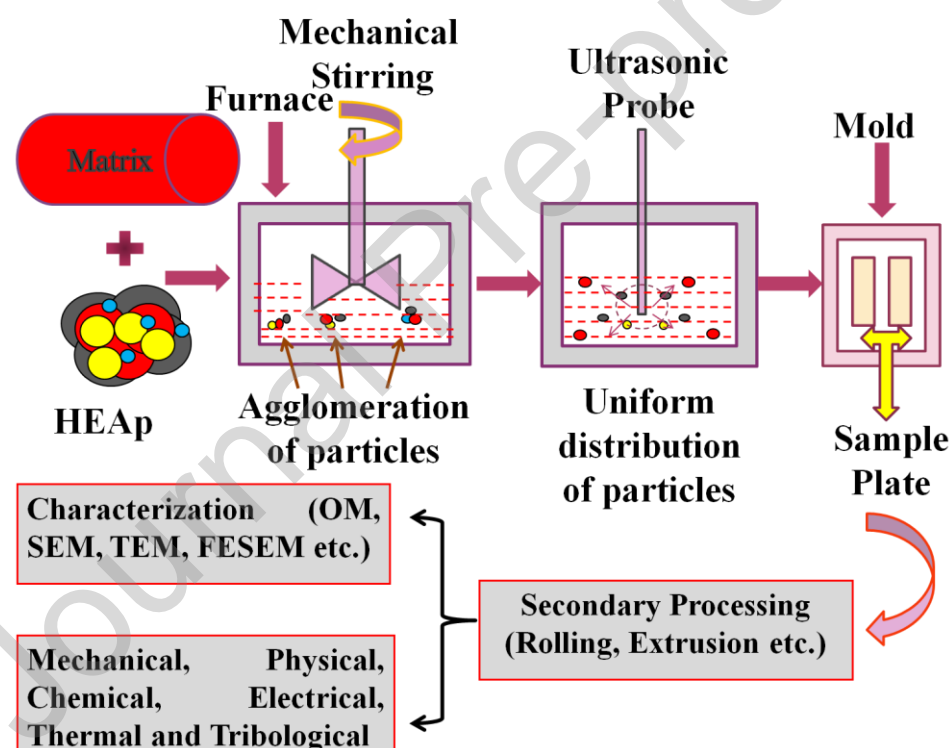


**Fig. 15** Ultrasonic assisted stir casting set up

Vacuum stir casting is one of the best methods of mechanical stirring, vacuum is provided to prevent oxidation of molten metal during casting of MMC. In case of centrifugal casting hollow circular sections of MMCs are prepared and the uniformity of the mixture achieved is very satisfactory. The substrate material is the reinforcing component of the casting compound and the clad material is the matrix component of the MMC. The substrate material was deposited on the preheated clad above the melting point and good interfacial bonding was achieved. Further, the secondary processing such as cold rolling can be done to improve strength with satisfactory ductility. Along with solid-state manufacturing and liquid-state manufacturing techniques, additive manufacturing (AM) is one of the advanced techniques for fabricating

HEA reinforcement-based MMCs in recent years by many researchers. A detailed description of the method, mechanism and fabrication route is presented in the following section.

### **2.3 Additive Manufacturing (AM):**

Additive manufacturing (AM) is the process of incrementally depositing layered materials to create a three-dimensional structure based on a computer-aided design (CAD) model. There are various fundamental AM processes such as direct energy deposition, powder bed fusion, material extrusion, binder jetting, material jetting, sheet lamination and vat polymerisation. Among these processes, the direct energy deposition (DED) and powder bed fusion (PBF) processes are well suited to process metallic materials. The DED process is illustrated in first part of **Fig. 16**. In the last decade, DED and PBF processes have been extensively used to process various metallic alloys and composites [44-47]. These rapid solidification processes not only enable the manufacturing of complex geometry but also provides alloy design freedom owing to its non-equilibrium solidification. According to the literature, DED and PBF processes have gained enormous attention to process novel alloys especially high entropy alloys (HEAs) [60-64].

The historical development of HEAs and its background is already discussed in previous section 1. Although HEAs have been processed by various routes including powder metallurgy [65], induction or arc melting [66], mechanical alloying followed by spark plasma sintering [67], the processing of HEAs through DED and PBF processes has remained the prime focus in last few years [63]. Several reports have recently been published on the processing of HEAs by AM processes [49-51]. However, the HEAs reinforcement in metal matrices and hard particle reinforcement in HEAs through AM processes are less explored [22, 56, 57]. A number of reports have depicted the addition of hard particles such as SiC, TiC, nano diamonds,  $\text{Sc}_2\text{O}_3$ , h-BN, c-BN, TiC etc. in HEAs matrix [70]. The addition of bulk metallic glasses in HEAs is another type of multi component system which has been explored by few researchers [71]. The processing of HEAs-MMCs by AM falls within the scope of this review. Therefore, the processing methodology of the HEAs-MMCs through DED and PBF processes is schematically shown in **Fig. 16. (b) and (c)** and briefly discussed.

AM is about layer-by-layer fabrication of components and reducing process time and material, specifically Direct Energy Deposition (DED) and Powder Bed Fusion (PBF) processes. For high entropy alloys (HEAs) and their composites, these processes have indeed revolutionized the production, alloy design and fabrication of complex geometries. **Complex geometry manufacturing:** HEAs exhibit superior properties compared to conventional alloys and are difficult to fabricate or process by conventional machining methods due to their high strength, brittle phase behavior, and high melting point. The AM process enables complex design shapes or geometries that are difficult to produce by traditional methods in the required properties. Through AM processes, especially the PBF method material is used only where the final part geometry requires it, which reduces material waste, which increases production tooling consistency in the field of HEAs and their composites. **Alloy Design Flexibility:** HEAs have superior combinations of properties such as good hardness, high strength, and wear and corrosion resistance, adequate thermal and electrical properties. DED

and PBFs provide flexibility in alloy/composite design using HEAs, allowing researchers to use combinations of elements to form HEAs and their to create materials with desired properties for specific applications. By adjusting process parameters, element composition and microstructure, high-performance optimized HEAs and their new composites can be developed. The rapid processing of AM will be beneficial in creating innovative new HEAs and composites and help commercialize the use of HEA-based composites and products. AM facilitates the composition and distribution of reinforcement in the desired area of the produced part in the composite enabling new engineering materials with properties tailored to specific applications. AM facilitates valuable control over the microstructure and reinforcement architecture for designing HEA reinforcement-based composites. Overall, the DED and PBF AM process specifically for HEAs and their composites offers less waste of material, faster fabrication process, unparalleled design flexibility, and fabrication of complex internal and external geometries.

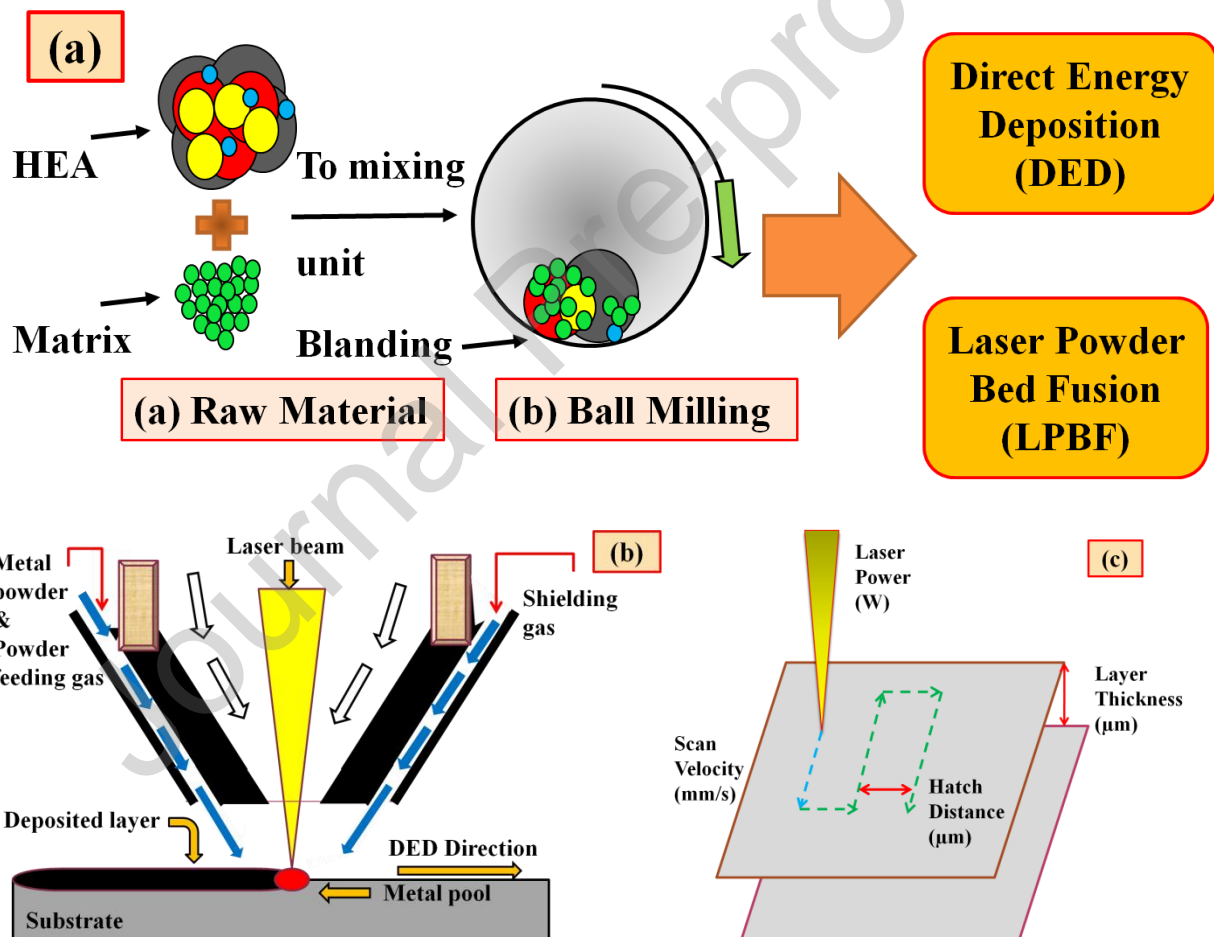


**Fig. 16** shows schematic diagram of (b) direct energy deposition (DED) and (c) powder bed fusion (PBF) processes

**(a) Direct Energy Deposition (DED):** Several research articles have been presented to describe the processing of the DED method to generate HEA-MMC [60-62]. The researchers explained the material design, fabrication, and challenges of the DED process; the application of the DED process, and the study of layer thickness in the DED setup. The DED process is defined as a “3D printing process in which material

will fuse via thermal energy of focused laser beam". The cladding and welding phenomena occur in the DED process [63–68]. Welding heat flux, laser electron beam, electric arc, etc. have been used for thermal energy, which is focused on previously prepared layers [69, 70]. The powders were deposited in the thermal energy-focused region from the feedstock [71, 72]. This thermal energy forms a pool of molten metal with the layer and feed powder and surrounds the focused thermal beam as shown **Fig. 16 (b)**. This cycle of layer-by-layer formation is repeated until a 3-D metallic part or component is fabricated [84].

**(b) Laser Power Bed Fusion (LPBF):** HEA-MMC fabrication in the PBF process begins with the preparation of 3-dimensional (3-D) files in computer-aided design (CAD) software. The 3-D structure is divided into two dimensional (2-D) sliced layers. In the PBF process layer formation occurs on a base plate or previously formed layers. According to each sliced layer profile the high energy laser beam starts melting the localized powder particles. Before each layer building the platform is lowered according to the predetermined layer thickness and this cycle runs until the last layer is formed to complete the component [85]. LPBF metal additive manufacturing technology offers several advantages over traditional manufacturing processes such as casting, powder metallurgy, and machining or forging Complex geometries and integral shapes that are sometimes impossible or difficult to fabricate by conventional methods can be fabricated by LPBF. This enables manufacturers to produce lightweight products in the desired design with less material consumption and without compromising the performance of the part. LPBF uses material in the design only where it is needed and it saves material compared to traditional subtractive methods such as machining. This makes it a cost-saving method for expensive materials such as nickel alloys and titanium metal. Also, in the case of traditional manufacturing methods for low-volume production tooling, setup cost increases the total cost of production. No tooling is required in LPBF, which is advantageous for low-volume production. The LPBF method makes it possible to control the microstructure of the produced parts, thereby ensuring the desired mechanical properties and surface finish. Layer-by-layer fabrication allows better bonding of fabricated components, resulting in consistent performance and quality. In addition, complex intricate internal structures can be fabricated by LPBF that are difficult to fabricate by conventional methods or require a combination of machining methods. LPBF eliminates the need for product assembly and a potential point of failure, thereby improving the reliability of the final product. Oliveira et al. [86] studied different process parameters like Laser power (W), scan velocity (mm/s), hatch distance ( $\mu\text{m}$ ), and layer thickness ( $\mu\text{m}$ ) used in the PBF process effects on residual stress, microstructure, porosity, and composition. The **Fig. 16 (c)** represents the process parameters of PBF process. The LPBF process is less time-consuming and cost-effective because it does not require a mold design to create a 3-D component design [87]. Zhang et al. [88] used LPBF method for fabricating stainless steel metal matrix composite reinforced with high entropy alloy for improving mechanical properties. The 5 wt. % of HEA reinforcement and 95 wt. % matrix powder were ball milled before proceeding to LPBF process. The HBD-100 printer machine was used with maximum laser power of 200 W. The printing parameters were set for component printing to study the microstructural analysis, tensile and corrosion properties.

### **3. Micro structural evaluation of high entropy alloy based metal matrix composite:**

It is necessary to conduct microstructural analysis to study the effect of HEA reinforcement on matrix phase after fabrication of HEA based reinforced MMC. The OM, SEM, FESEM, EDS, XRD, TEM, HRTEM, EBSD are the microstructural studies which provide detailed information of HEA based reinforced MMC. The OM, SEM, FESEM and EBSD can be used to study the distribution and bonding of HEA particles in the matrix and XRD and EDS analysis provide information about element identification in the composite. These sections discuss the microstructural study of HEA based reinforced MMC and evaluate the behavior of HEA with the matrix and relate it to mechanical properties.

The copper and its alloys have wide applications in the electrical industries, equipment such as electrical wiring, automotive components and heat exchangers, due to their good electrical and high thermal properties. Copper does not show high strength at higher temperature and its hardness and strength also decrease at room temperature. Some of the applications of copper are restricted due to high wear rate and less hardness. Therefore, researchers found HEA as a good reinforcing agent for improving the mechanical and electrical properties of copper by observing the structural characterization of composite. For this Chen et al. [31] used SEM and TEM for characterization study of Cu-HEA alloy prepared by powder metallurgy route. The Cu-AlCoNiCrFe composite was fabricated with addition of 10 and 20 wt. % of HEA to study the microstructure analysis as shown in **Fig. 17 (a, b)**. The dark area shows the presence of HEA is confirmed by EDS analysis with constituent elements of Al, Co, Cr, Fe and Ni and the bright area shows the presence of Cu metal matrix. The images reveal that there are no pores and voids in the mixture, thereby Archimedes' principal value suggests that with increasing the wt.% of HEA in composite it increases the density of composite and got compacted after sintering process. It is also observed that HEA is free from any intermetallic phase during process and no interface reaction occurs between the interface of HEA and Cu matrix as shown **Fig. 18 (a-d)**. No grain growth of HEA was observed during sintering and an average grain size of 20 nm of HEA was found in the composite which was higher compared to 60h milled HEA powder.

More work is reported for aluminum matrix reinforced by HEAp content, some studies are reported in forthcoming reviews. Ananiadis et al. [33] fabricated the Al 1050 alloys based composite with reinforcing MoTaNbVW HEA powder (0, 1, 3, and 5 wt.%) through powder metallurgy process. Prior to compaction the matrix and reinforcement powders are stirred into methanol and left to dry so that no aggregation occurs between the particles. The monolith and each composite were pressed with a force of 7.6 tons to produce a cylindrical pellet of 14 mm diameter and then sintered at 550°C with an increase of 50°C/min. After 1 h specimens were pressed by 6500 N with a gradual loading rate of 1000 N/min for 30min. Then samples were left for the furnace to cool. The samples were cleaned with SiC sandpaper and cloth. Samples were gone through a metallographic procedure to do SEM and XRD analysis.

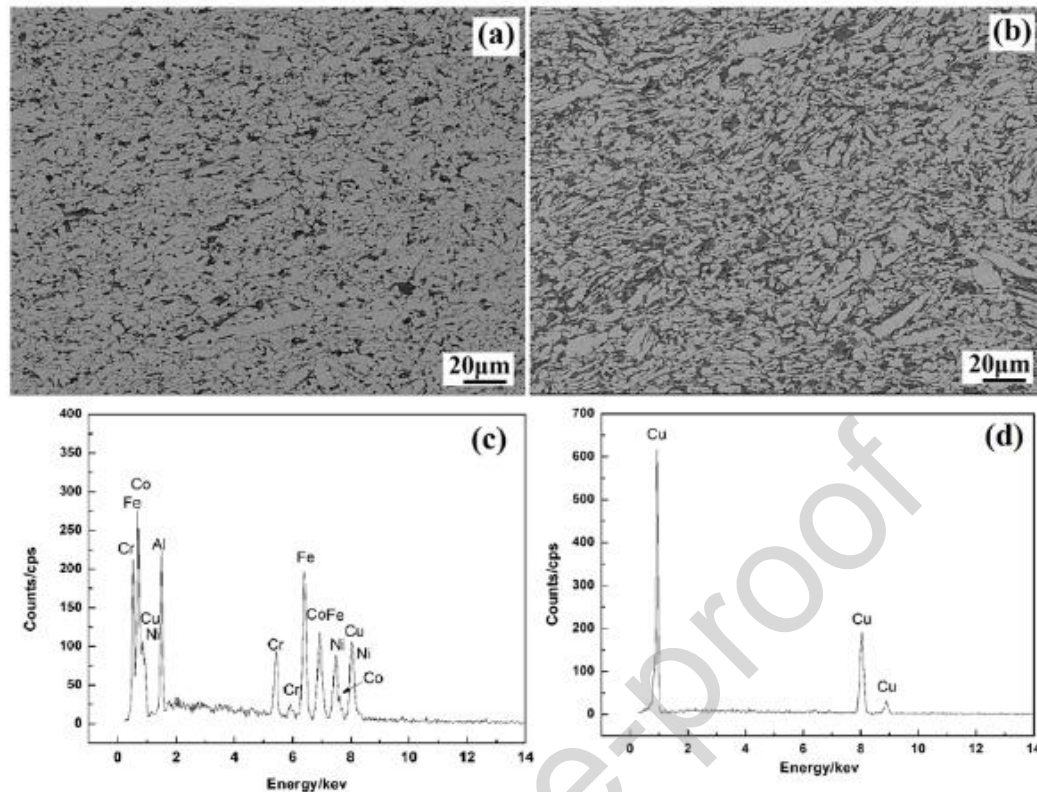


**Fig. 17** SEM image (a, b) and EDS analysis (c, d) of composite with 10 wt. % and 20 wt. % HEA respectively [31].

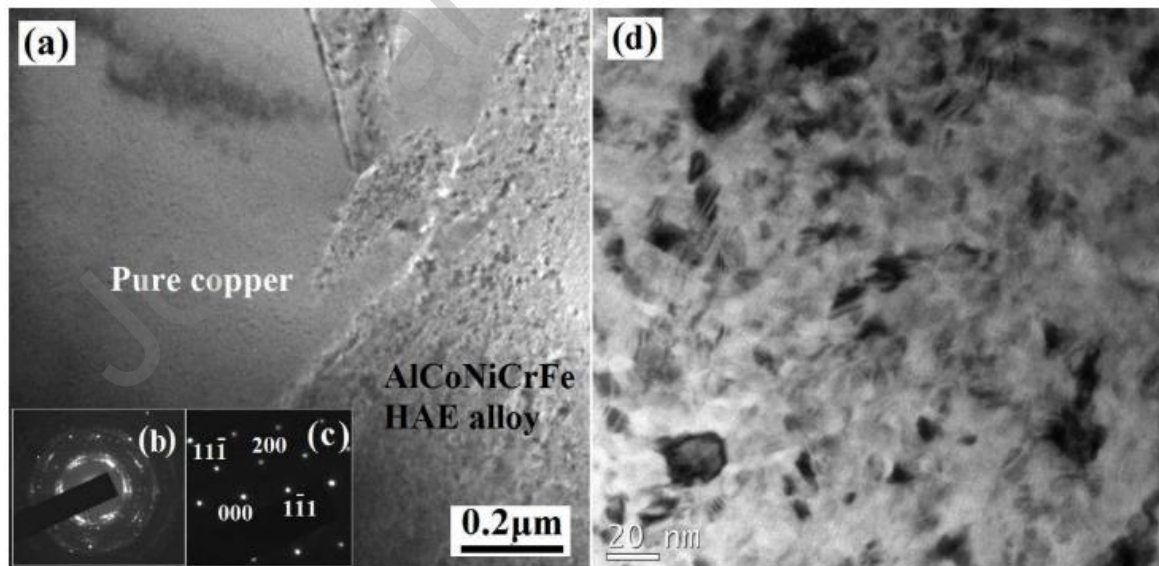


**Fig. 18** TEM image of (a) 20 wt.% HEA-Cu composite, (b) HEA, (c) Cu, (d) high magnification of HEA reinforcement [31].

**Fig. 19 (a)** represents SEM in secondary electron imaging mode and EDS analysis of HEAp. The results show that there are angular-shaped HEA particles with sizes ranging from 1 μm to 30 μm. At different particle area, EDS analysis shows an average at.% composition of HEA which represents the near equiatomic

nature of HEAp. When MoTaNbVW HEA powder is added to aluminum matrix at varying wt.% from 0 to 5, it changes the XRD pattern of HEA-Al composites. It is observed that the peak intensity of aluminum decreases in XRD (**Fig. 19 (b)**) and the peak intensity of HEA increases with increasing the wt.% of HEA from 0 to 5. Both BCC solid solutions phase one MoTaW and NbV have small peaks and higher peaks in all XRD composites corresponding to the FCC phase of the aluminum matrix. The two BCC phases of HEAp are separated after fabrication and solidification of the composites, which supports the solid solution nature of HEAp and was also reported in previous studies of MoTaNbVW refractory HEA [89]. The SEM images in **Fig. 20** show the presence of 1,3 and 5 wt.% HEAp in the HEA-Al alloy. An increase in HEAp content in the aluminum matrix is reflected in the SEM images, with an increase in small, submicron and bulk particles of HEA in good agreement with the reinforcement particle content. Homogeneous distribution and uniformity of reinforcing particles were ensured by using powder metallurgy method in the microstructure. The sintering process removes defects in the alloys and ensures solid, rigid and dense products. There was no evidence of microvoids or microcracks in the system with increasing HEAp content. An EDS study was performed around the bulk HEAp-Al composite system as shown in **Fig. 21**. EDS confirms the presence of constituent elements of MoTaNbVW refractory HEAp. It shows no voids or pores on the surface as observed at the interface between HEA and matrix and reflects good bonding of particles. There is no brittle intermetallic phase that reduces the overall strength of the final alloy. The absence of an oxygen phase has also been reported to be associated with the Al matrix.

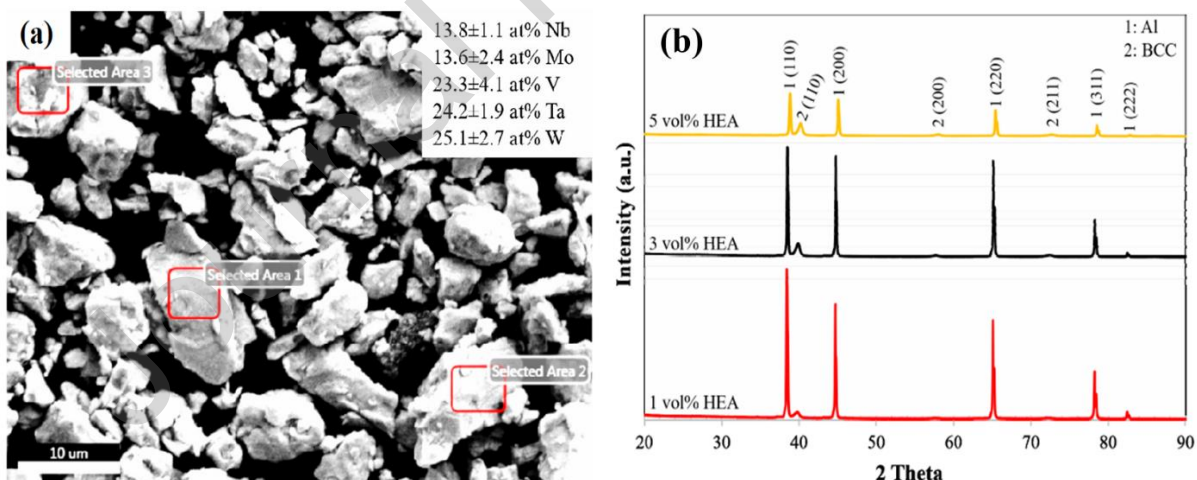


**Fig. 19** (a) HEAp SEM+EDS image (b) XRD of Al-HEA composite-[33].

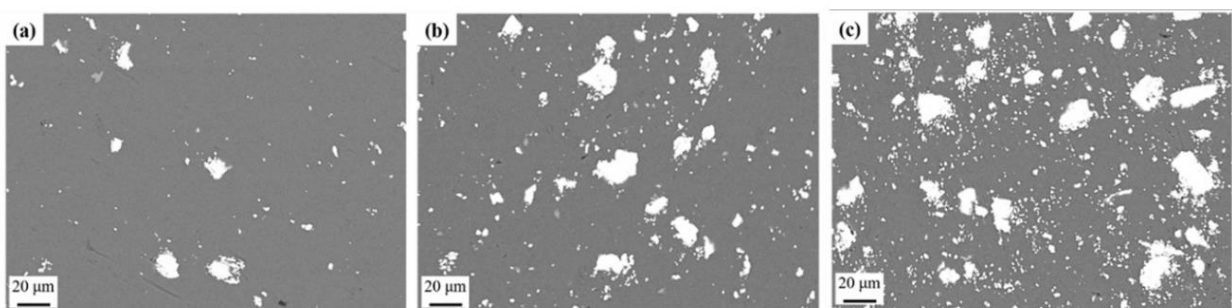


**Fig. 20** SEM images of composites (a) 1 wt.% HEA-Al, (b) 3 wt.% HEA-Al and (c) 5 wt.% HEA-Al [33].

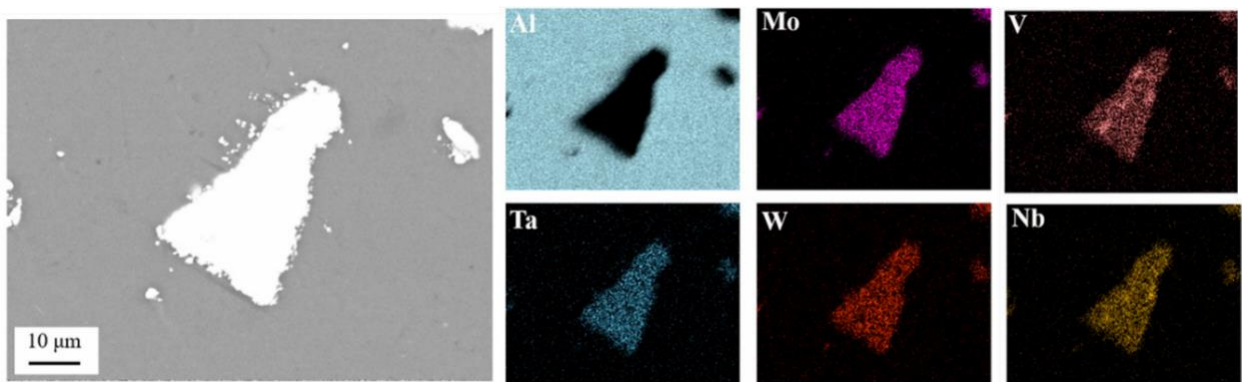


**Fig. 21** EDS and elemental mapping of HEA-Al composite [33].

The same powder metallurgy method was used by Prabakaran et al. [32] to prepare the AA 6061 composite by reinforcing 10 and 20 wt. % of CrMnFeNiCu HEA with different sintering temperatures and times. The HEAs were ball milled for 10, 20, and 40 hrs. and examined by the XRD technique as shown in **Fig. 22**. The XRD pattern indicates a solid solution HEA powder with a low BCC and high FCC phase during all milling due to the CrFeMnNi metal system. The peaks broaden with the increase in milling time and from Scherrer's equation the minimum crystallite size and maximum lattice strain were found for 40 hours milling HEA powder, no further improvement was found after 40 hours. HEA of 40 hrs milled powder was mixed with AA-6061 through a ball milling process for 5 h. The mixed powder was compacted and then sintered at 560°C and 600°C with a soaking time of 1 h and 2 h. In **Fig. 23** SEM images of matrix, reinforcement and composites are seen. The flat particles were found due to presence of more ductile phase in matrix. After 40 hrs of milling particle size of HEA got reduced as seen in **Fig. 23 (b)**. HEAs adhered to the matrix very easily and evenly distributed in composite as shown in **Fig. 23 (c & d)**. Small particles of HEA bond tightly with the matrix and it results in low porosity and increased strength.

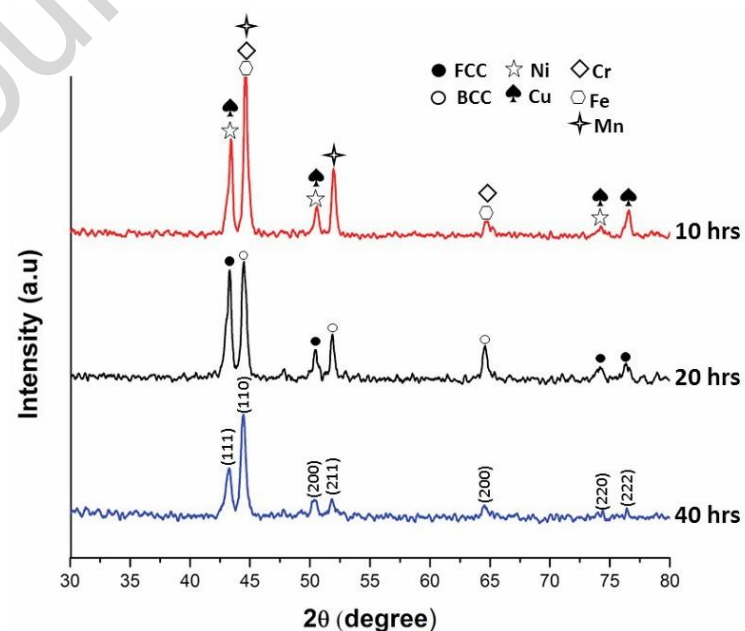


**Fig. 22** XRD pattern of HEA powder after 10, 20 and 40 hrs milling [32]

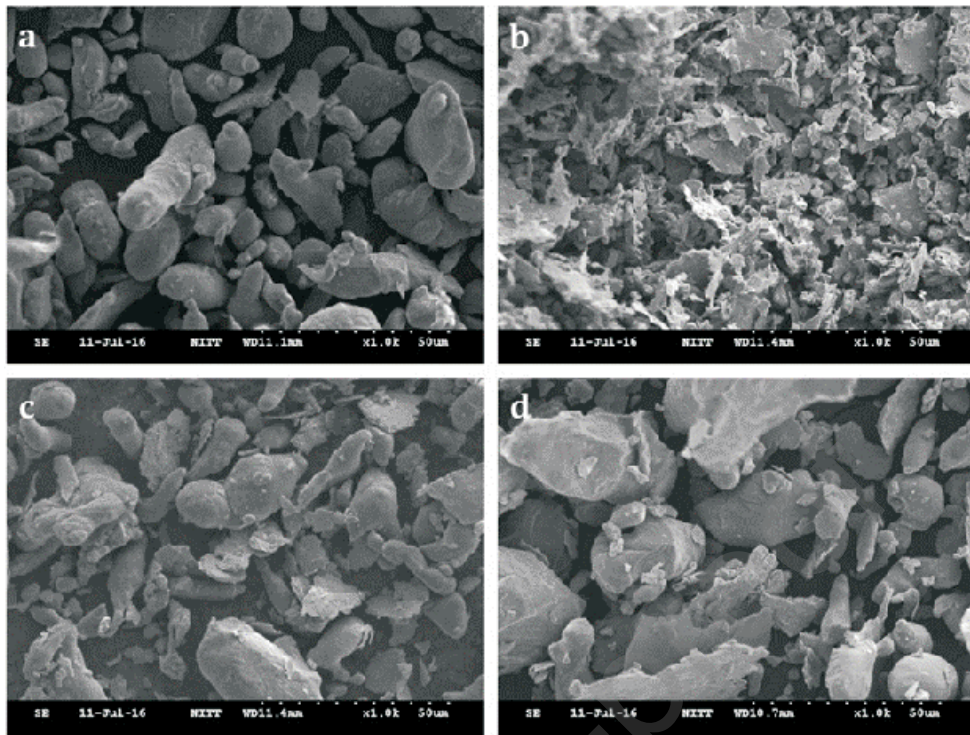


**Fig. 23** SEM images of (a) AA6061 (b) HEA (c) AA6061 + 10% HEA (d) AA6061 + 20% HEA [32]

Zhang et al. [54] fabricated the Al-HEA MMC with different wt. % of HEAs as a reinforcement with ultrasonic stir casting method. It is observed that the white bright phases are seen along the grain boundaries of matrix these might be  $\text{Al}_2\text{Cu}$  as reported in other study shown in **Fig. 24** [90]. The presence of gray phases is attributed as HEAp in composites and agglomeration of particles shown as increase of HEAp addition from 0.5 to 5 wt.%. A different interplanar spacing between the Al matrix and the reinforcement is found in the composite and is represented by the red line causing lattice distortion, while Al has 0.205 nm and HEA shows an interplanar spacing of 0.301 nm as measured from **Fig. 25 (a & b)** and BCC phase were observed in **Fig. 25 (c)**. In TEM image **Fig. 25 (d)** rod shaped with red circle shows presence of  $\theta$  precipitates and plate-like shape with yellow circle shows Al matrix.

The inter-diffusion (ID) layer between the HEA and the matrix has found a key role in improving the mechanical properties of the composites. The researchers discussed the effect of the transition layer on the composite through microstructure characterization and evaluation of different mechanical properties. It has been found from studies that the powder metallurgy process sets up an ID layer around the HEAp directly bonding with the matrix, and no study has yet been conducted for casting and additive manufacturing method in composite manufacturing.

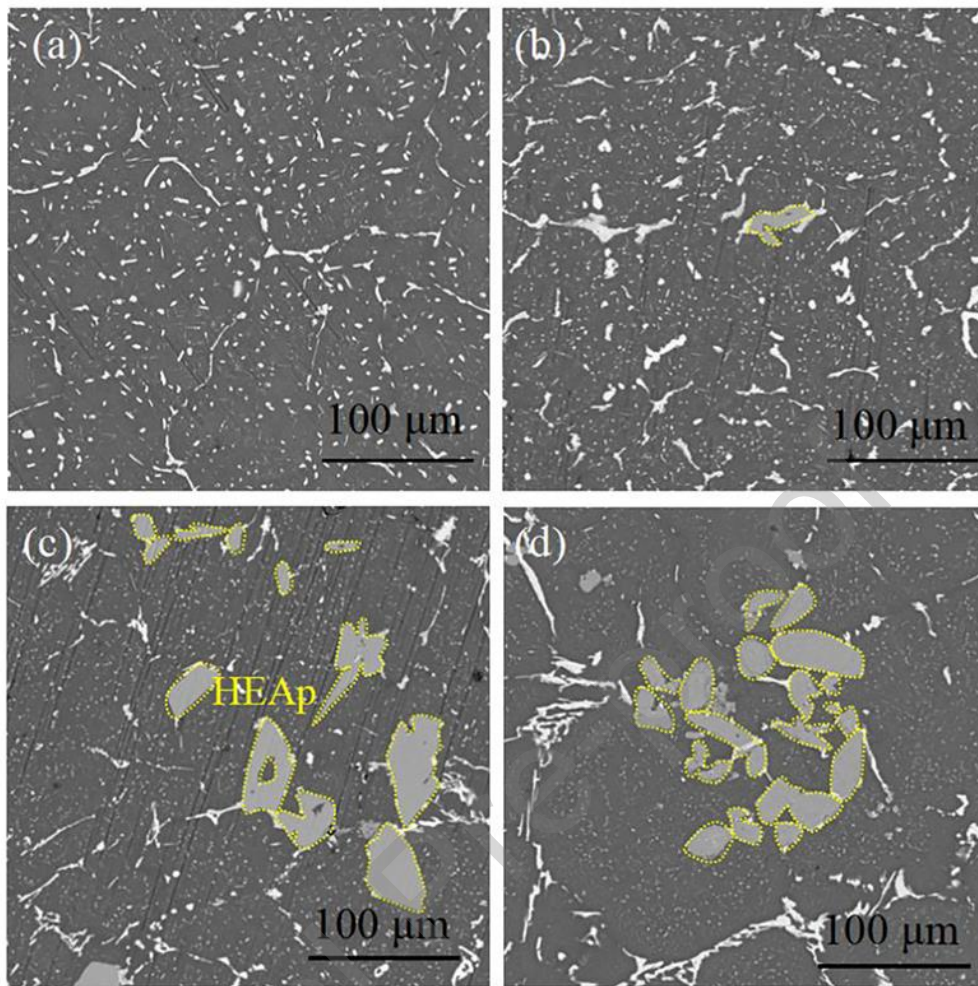


**Fig. 24** SEM microstructure images of HEA/AMC with (a) 0, (b) 0.5, (c) 3 and (d) 5 wt. % HEA [54].

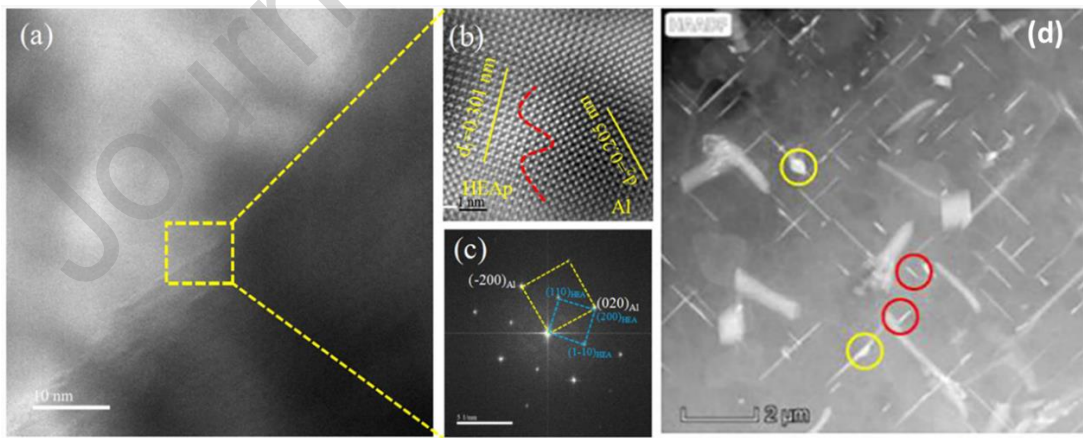


**Fig. 25** (a) (b) and (c) HRTEM (d) TEM of 1.5 wt.% HEA-AMC [54].

Yuan et al. [91] used a spark plasma sintering method to fabricate an aluminum 2024 alloy-based composite reinforced by CoCrFeMnNi high entropy alloy particles. The diffusion and composition of layers between the HEA and matrix were investigated with SEM images, EDS and XRD. The inter-diffusion (ID) layer found between the matrix and reinforcement particles is attributed to the enhanced stiffness of the composite. In XRD test (**Fig. 26**) new  $\text{AlCu}_2\text{Mn}$  and  $\text{MnAl}_6$  phases were detected in the composite along with matrix and HEAp phase. These new phases were formed by reaction of surrounding Al atoms with Mn and Cu

atoms. This shows that due to the sintering and heating process, the interaction between the matrix and the reinforcement takes place, resulting in the formation of an interface phase layer. **Fig. 26 (a)** is low magnification SEM of HEA, showing smooth spherical shape with particle size  $< 50 \mu\text{m}$ . **Fig. 27 (a, b)** indicates SEM of composite, gray matrix phase and the presence of white spherical particles phase are evenly distributed in the matrix to develop the composite. From the SEM it is confirmed that no change in HEAp shape occurs after ball milling, however, the diffusion layer forms a ring shape near the HEA and between the matrix. The diffusion layer has a different color compared to the matrix and HEA. Dark gray in ring shape near HEA and light bright color with irregular shape at outer edge of diffusion layer. The reason for the irregular shape of the layer is the non-uniform dispersion of elements and diffusion of HEA with the matrix. The elements near HEA reacts fast and near matrix high growth happens so that flat diffusion layer found near HEA and serrated near matrix. The diffusion tackiness found to be  $6 \mu\text{m}$  with less porosity and highly dense. The variation of compositional elements in ID layer is characterized by EDS imaging, HEA particles were evenly distributed in ID layer shown in **Fig. 28** and reported that the densification of ID layer depends on current flow between metal particles. Tan et al. [92] found that around the HEAp temperature above the melting point of matrix was produced. The thermal environment created by the current is insufficient to exceed the melting point of HEA, so that diffusion of particles occurs not only between HEA and Al but also between HEAp. Al and Cu elements do not diffuse, but Fe, Ni and Co form a large area near the inner diffusion layer due to their large diffusion coefficient.

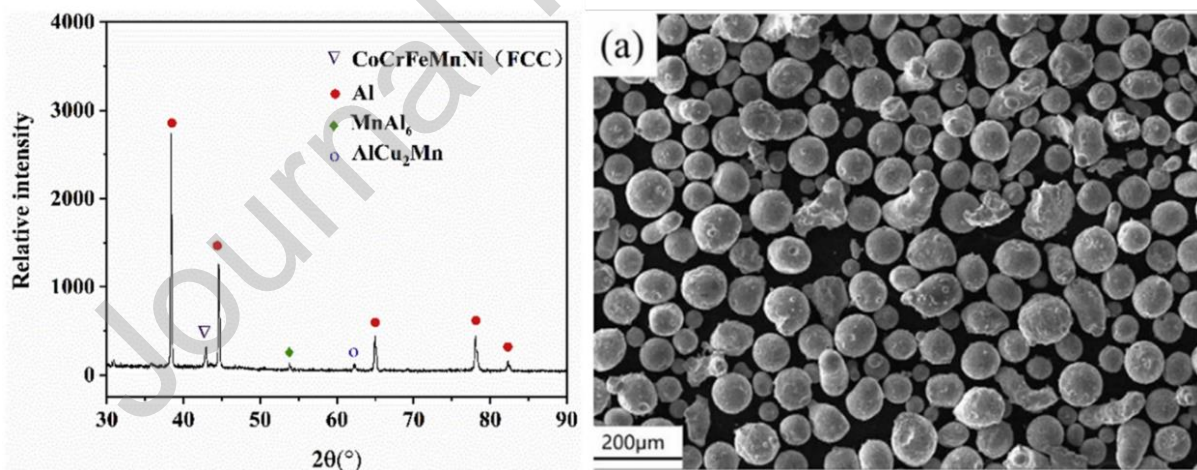


**Fig. 26** XRD pattern of composite and SEM image of (a) HEA in low magnification [91].

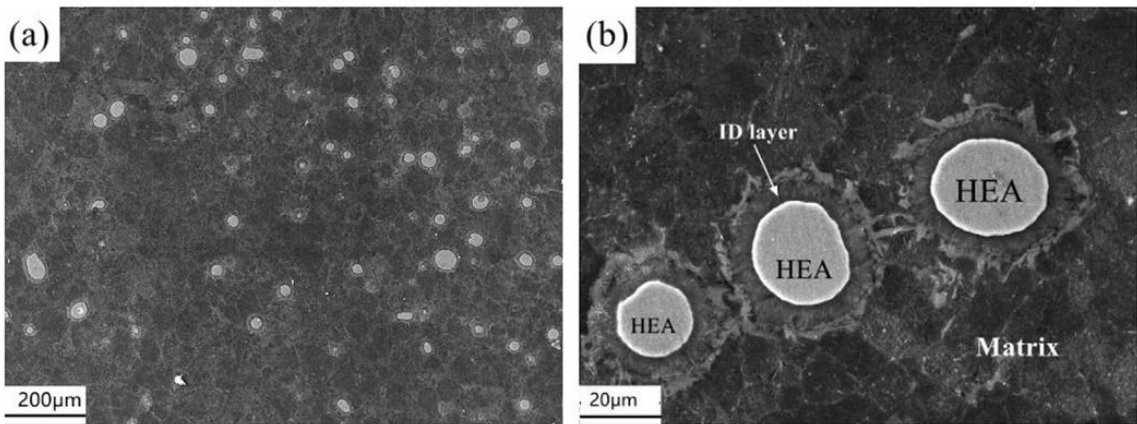


**Fig. 27** SEM image of composite in (a) low magnification and (b) high magnification [91]

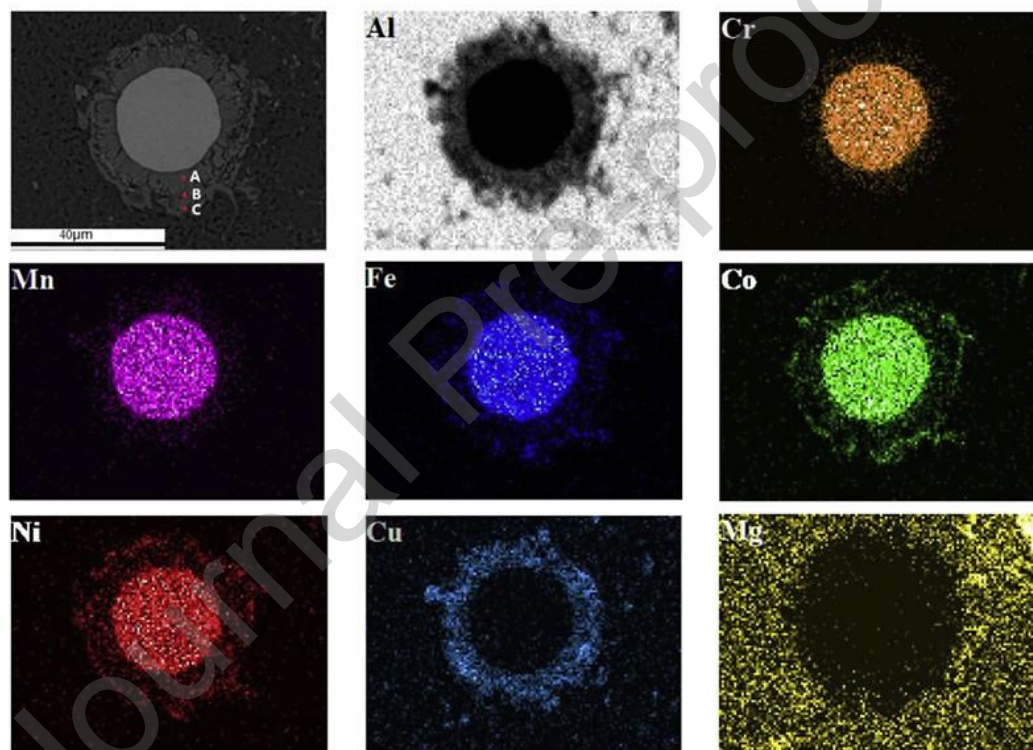


**Fig. 28** EDS result of HEA-Al composite [91].

Liu et al. [93] studied the effect of the transition layer formed between the reinforcement and the matrix on the mechanical properties by fabricating the Al-AlCoCrFeNi composite. Firstly XRD, SEM and EDS were performed on the HEA reinforcement powder for the evolution of HEA powder's characterization. From **Fig. 29** the XRD pattern shows a body-centered cubic (BCC) phase and a spherically smooth structure in shape of HEA. Spot EDS analyzed the chemical composition and confirm the equiatomic ratio and equal distribution of elements. From **Fig. 30 (a-d)** it is observed that the HEA is well bonded with Al matrix and no defects were found in the composite. A transition layer of about  $4\text{ }\mu\text{m}$  was produced between the matrix and the reinforcement particle when sintered at  $560^\circ\text{C}$ . As the sintering temperature increases, the transition layer thickness expands and its average thickness increases. Thickness of this layer was found  $7.6\text{ }\mu\text{m}$  and  $15.1\text{ }\mu\text{m}$  at  $580^\circ\text{C}$  and  $600^\circ\text{C}$  respectively. The chemical composition of Al-5 vol % HEA was found at

different regions A (HEA), B (transition layer) and C (Al matrix) at 600°C are shown in **Fig. 30 (b)** and in **Table 1**. The FCC phase was found at the transition layer in Al-HEA MMC, with a high amount of Al matrix (82.79%), however, the atomic ratio of other elements Fe, Cr, Co and Ni remained the same.

A further study was carried out by TEM analysis to gain a further understanding of the transition layer in the AlCoCrFeNi HEAs reinforced Al matrix composite. It is observed that the smooth transition layer between the HEA particle and Al matrix as shown in **Fig. 31**. The selected area electron diffraction (SAED) in **Fig. 31 (d-e)** represents an ordered BCC phase of HEA near the transition and the transition layer should have an ordered FCC structure. The transition layer has a high Al content and equal amounts of other Co, Cr, Fe, and Ni elements, which ensures good solubility of HEA in the Al alloy. **Fig. 31 (c-d)** shows the grains of the 600 nm transition layer, which is less than 20 µm and 4 µm of Al matrix and AlCoCrFeNi HEA reinforcement, respectively. The mechanism of transition layer formed between HEA and Al matrix is demonstrated in **Fig. 32**. In the SPS method, the temperature distribution throughout the composite is not homogeneous, the neck (contact) zone of the particles has a higher temperature and it drops dramatically within the surface layer. The lattice-distorted HEA particles have a low thermal conductivity, about one-third that of pure Al, and these Al particles quickly transfer the heat contained in the transition layer due to this thermal gradient generated and columnar grains formed near the HEAp in the transition layer of composite.

**Table 1** Chemical composition of the 5 vol.% AlCoCrFeNi HEA reinforced Al matrix composite sintered at 600 °C (at. %).

Regions	Al	Fe	Cr	Co	Ni
HEA particle	20.86 ± 0.95	19.60 ± 0.52	18.98 ± 0.68	20.49 ± 0.39	20.37 ± 0.55
Transition Layer	82.79 ± 0.16	4.38 ± 0.35	4.39 ± 0.12	4.40 ± 0.09	4.04 ± 0.28
Matrix	100	--	--	--	--

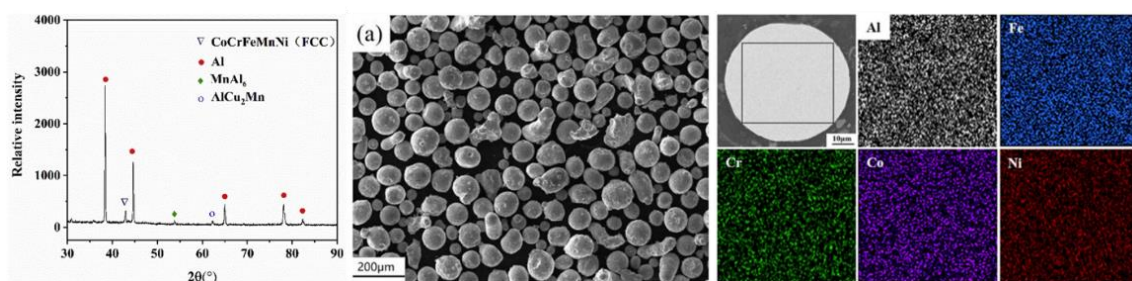


**Fig. 29** (a) XRD pattern, (b) SEM image and EDS analysis of AlCoCrFeNi HEA powders [93].

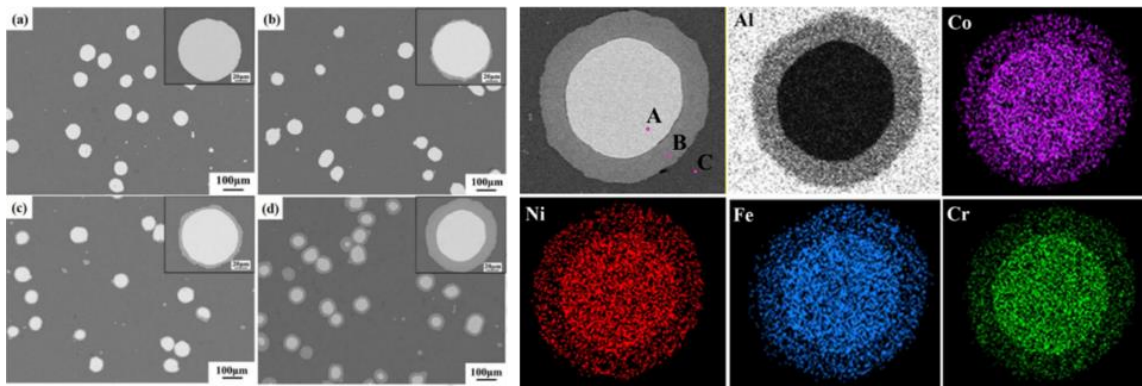


**Fig. 30** SEM images (A) of Al-HEA-MMC sintered at (a) 540°C (b) 560°C (c) 580°C and (d) 600°C, (B) EDS result of 5vol% AlCoCrFeNi HEA reinforced Al matrix composite at 600°C sintering temperature [93].

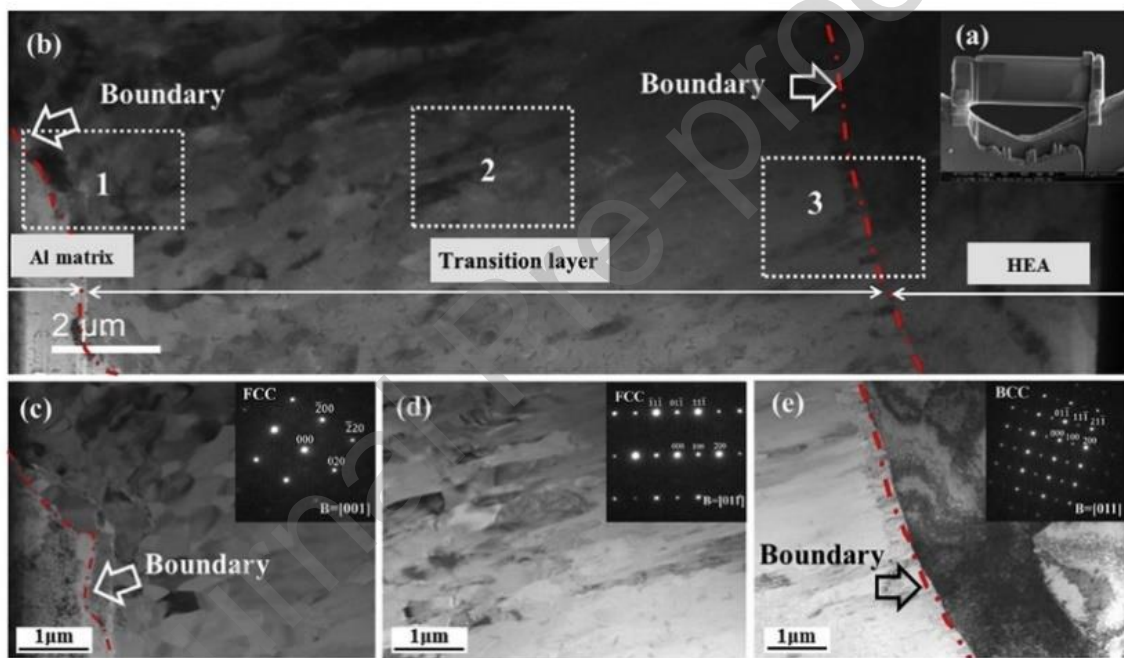


**Fig. 31 (a-b)** TEM diagram of 5 wt.% HEA-Al composite in 600°C sintered temperature, (c-e) images of regions indicated by 1, 2, and 3 in (b) [93].

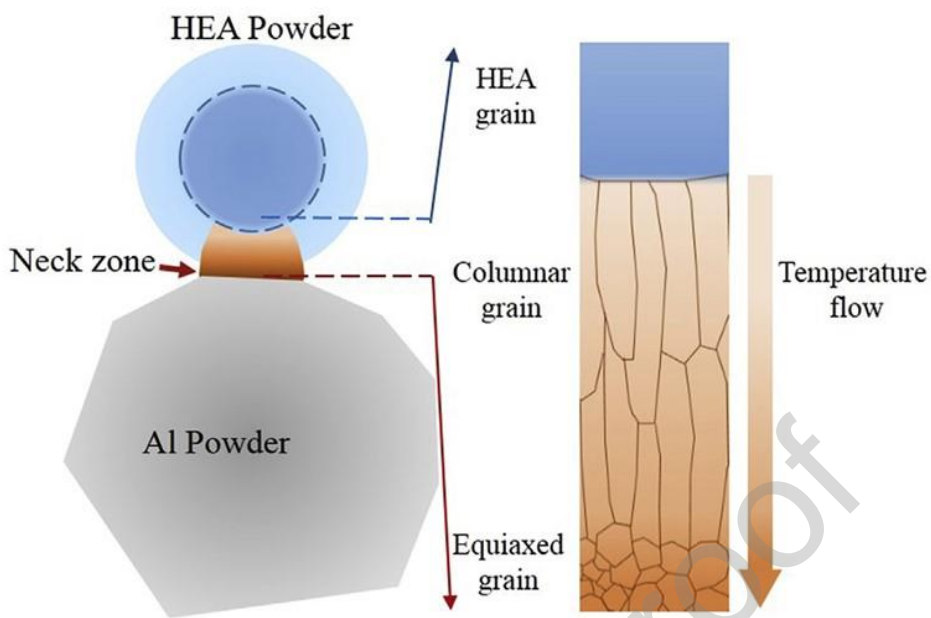


**Fig. 32** Diagrammatic representation of the mechanism of transition layer creation [93].

Yuan et al. [94] fabricated the HEA ( $\text{Al}_{0.6}\text{CoCrFeNi}$ )-Al composite by hot pressing sintering technique and studied the microstructural analysis of HEA-AMC under various heat treatment conditions. The results revealed that gray sphere particles show the presence of HEA and light yellow represents the matrix phase as shown in **Fig. 33**. In the as-received state of the composite and the initial stage of heat treatment, a very thin layer was found between the matrix and the reinforcement. It did not start diffusion in interface due to low temperature of sintering and activation energy not reach up to  $500\text{ }^{\circ}\text{C}$  as shown in **Fig. 33 (a-b)**. The interface layer thickness increases with increasing holding time at a fixed heat treatment temperature of  $500\text{ }^{\circ}\text{C}$  due to a higher diffusion rate as shown in **Fig. 33 (c-e)**. However, less changes were obtained from 24 h to 48 h as the interface layer thickness increases at  $600\text{ }^{\circ}\text{C}$ , the diffusion rate of the Al matrix around the HEA becomes homogeneous due to higher acceleration. HEA shows a single BCC solid solution phase, but mixed Al,  $\text{Al}(\text{Co},\text{Fe})$  and  $\text{Al}_{12}\text{Mg}_{17}$  phases are formed during the sintering process as shown in **Fig. 34**. The strength of the new phase is not further observed and the strength of the new phase increases with the transfer of the peaks caused by the diffusion and distortion of the HEA in the Al matrix by the sintering process.

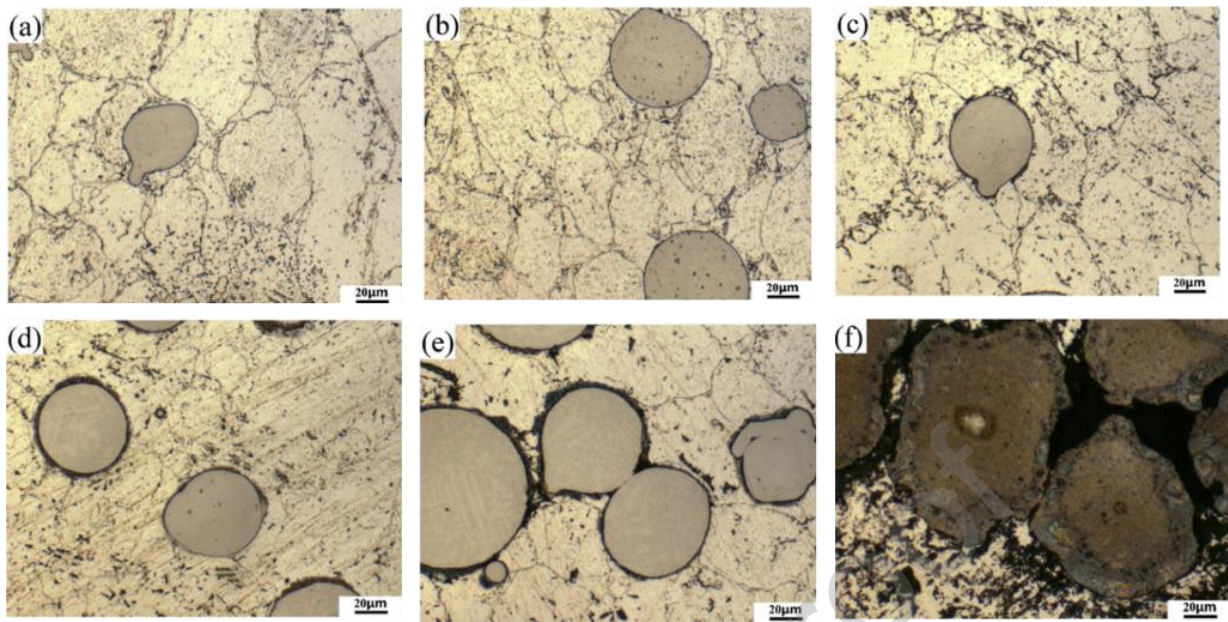


**Fig. 33** SEM images of composite at different heat treatment temperature and time. (a) Sintered sample (b) At 300 °C and 24 h (c) At 500°C and 12 h (d) At 500°C and 24 h (e) At 500°C and 48 h (f) At 600°C and 24 h [94].

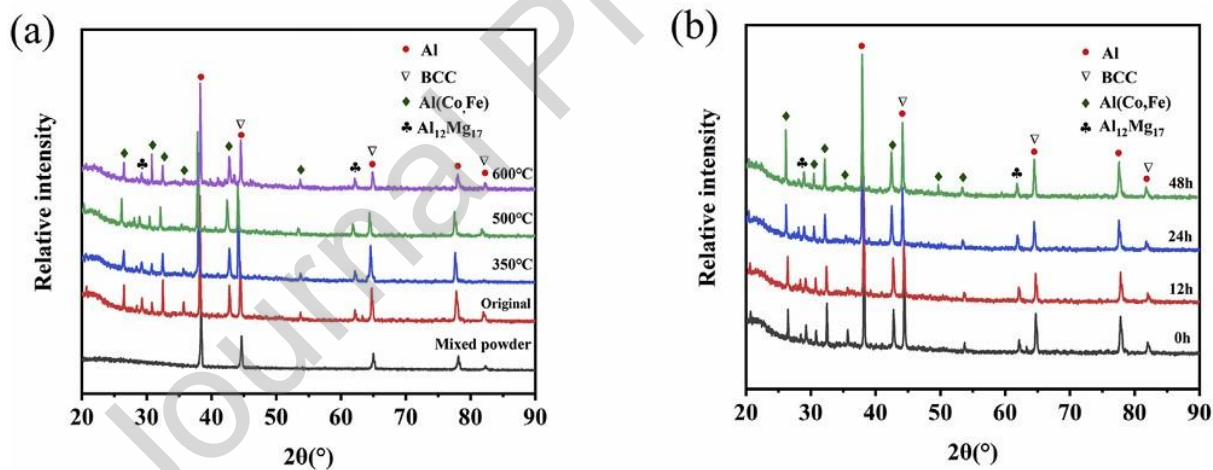


**Fig. 34** XRD pattern of composite at different temperature (a) for 24 hr and (b) for different time at 500 °C sintering temperature [94].

Yuan et al. [95] fabricated titanium matrix based composite reinforced with CoCrFeNiMo<sub>0.2</sub> HEA by vacuum hot sintering powder metallurgy method at different sintering temperatures. **Fig. 35** shows the microstructure of the composite at 700, 800, 850 and 900 °C sintering conditions. The white spherical shape confirms the presence of HEAp on the composite. The HEA is well bonded to the matrix, with no or little pores and defects at the interface. At 700 °C a very thin interface is shown between the spherically shaped HEA and the matrix, a small diffusion layer of HEA also appears on the matrix at that temperature. With increased sintering temperature from 800 and 850 °C, a thick diffusion layer is formed between HEAp and titanium matrix, at such high sintering temperature the component elements of HEA diffuse and make

irregular and uneven shapes of the diffusion layer, the same situation is repeated at 900 °C. The change in HEAp behavior at 700, 800, 850, and 900 °C is due to the dispersion and dissolution of HEA particles in the composites. The measured interface thicknesses show an increasing trend of  $1.3 \pm 0.1 \mu\text{m}$  at 700 °C,  $4.5 \pm 0.5 \mu\text{m}$  at 800 °C,  $6.8 \pm 0.8 \mu\text{m}$  at 850 °C, and  $14.5 \pm 0.2 \mu\text{m}$  at 850 °C and  $14.5 \pm 0.2 \mu\text{m}$  at 900 °C with increasing sintering temperature. This is also seen in the 900 °C sintered composite microstructure where the  $\beta$  titanium phase is transformed into the  $\alpha$ -titanium flake-shaped phase after 882 °C.

**Fig. 36** represents XRD analysis of Ti, HEA powder, and composites at different sintering temperatures. HEAp with diffraction angle of 76° and FCC phase with Ti powder in composite as shown in **Fig. 36 (a)**. After sintering the composite at 700 °C and comparing with the XRD results of the composite powders, two new peaks at 43° and 50° were observed, which confirmed the presence of HEAp. Other new phases TiCr2 and CrMo were found in the alloy at higher sintering temperatures of 800 °C and 850 °C, which are shown in **Fig. 36 (b)**. It can be observed that the dispersion of HEAp in the matrix forms a TiCr2 phase in the alloy and forms a diffusion layer with some thickness around each HEAp. A shift of peaks in XRD with increasing sintering temperature is also observed. This may be caused by the lattice distortion of HEAp on the matrix when the composite is sintered with a hot pressing process. **Fig. 37** shows the EDS analysis of the composites at different sintering temperatures of 700, 800 and 850 °C and the corresponding results are tabulated in Table 2. The insight phase structure is determined from the backscattered image of the composite in **Fig. 37 (a)**. White shows the presence of CoCrFeNiMo0.2 HEA phase, light gray thick diffusion layer composed of HEA and matrix, gray titanium matrix phase. The content distribution of HEA elements in the diffusion layer varies due to the different diffusion rates of each element of HEAp. CoCrFeNiMo0.2 HEAp elements Co, Ni and Fe are diffused at the outer edge of the diffusion layer with the titanium matrix. Some intermetallic compounds of Co, Fe and Ni may be present there. As the sintering temperature increases from 700 °C to 800 °C and 850 °C the diffusion layer thickness increases (**Fig. 37 (b & c)** backscattered image) and it becomes an inner and outer boundary. In the inner layer, it contains all five elements of HEA with a low titanium phase, while in the outer layer, it contains only Mo, Cr elements and rich Ti. Cr and Mo elements attain full diffusion at higher sintering temperatures compared to 700 °C. From the sintering temperature of 800 °C and above the Cr and Mo content of the HEA element is lower in the center compared to the outer layer and vice versa with the other three elements. From the EDS analysis results, it is confirmed that there is no titanium element at the HEA particle area, so unidirectional diffusion of HEA particle makes a diffusion layer between HEA and matrix in the composite. The composition of the diffuse layer at specific points labeled in **Fig. 37** is listed in Table 2. At the point at 700 °C the distribution of HEA particles is only with composite powder. At point B the amount of Co, Fe and Ni is higher than that of Cr and Mo because Co, Fe and Ni form the FCC phase in the composite. The content of Cr and Mo in the diffusion layer is higher than the other three elements. HEA elements decrease near the matrix at points C, D, E and F in the diffusion layer. As the sintering temperature increases, the precipitation of HEA in the diffusion layer increases.

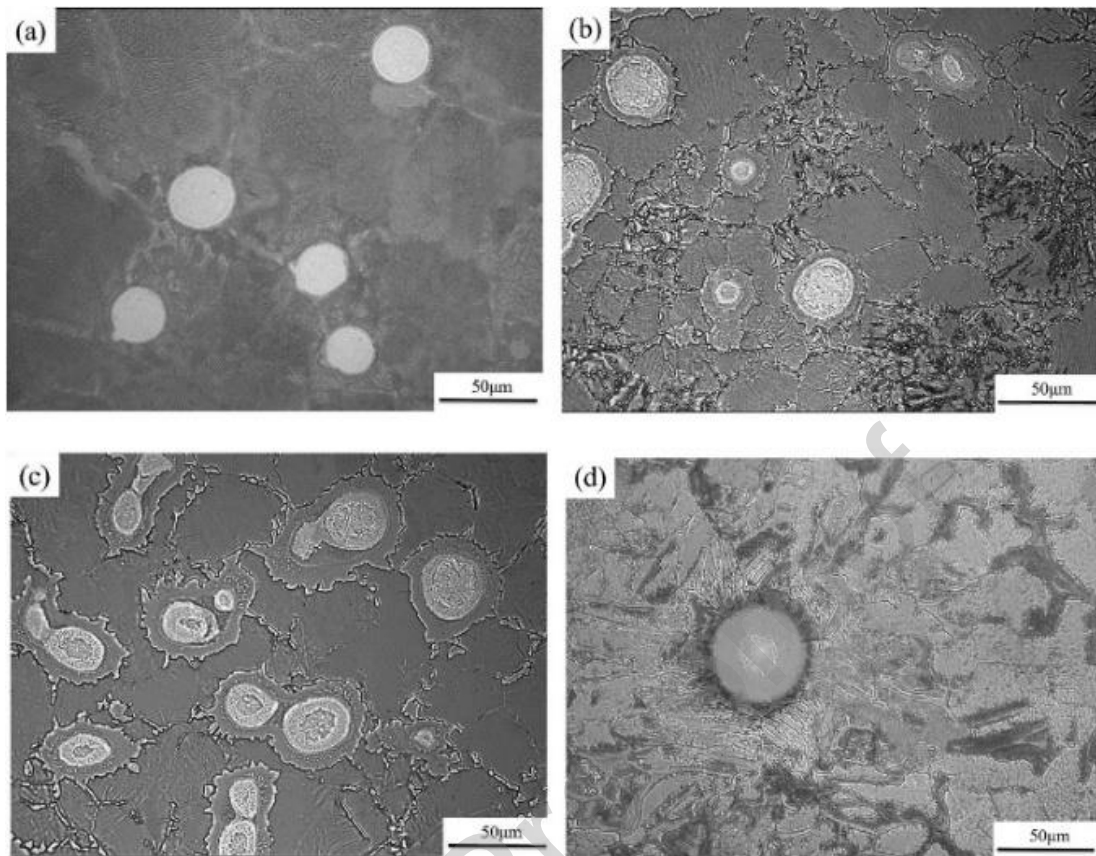


**Fig. 35** Micrograph of composite at (a) 700 °C, (b) 800 °C, (c) 850 °C, (d) 900 °C [95]

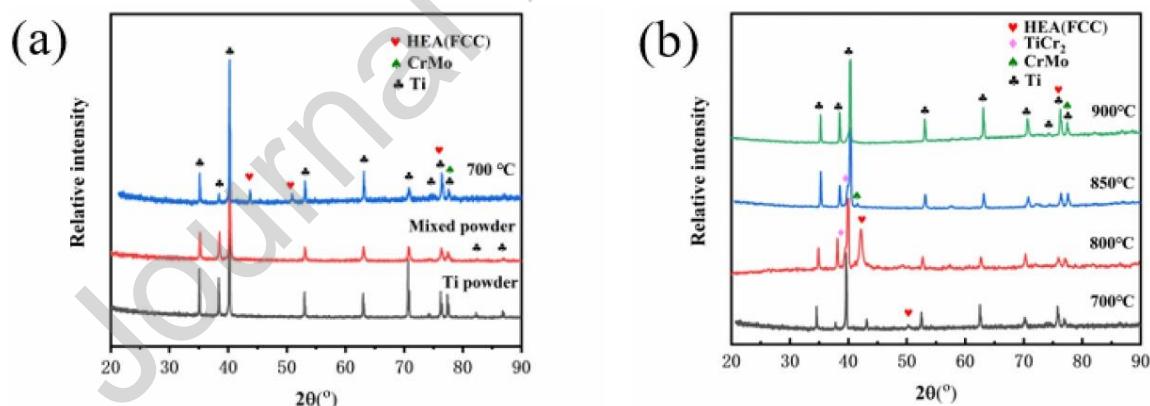


**Fig. 36** XRD pattern of (a) Ti powder, HEA, Composite (b) Composites at different temperature [95]

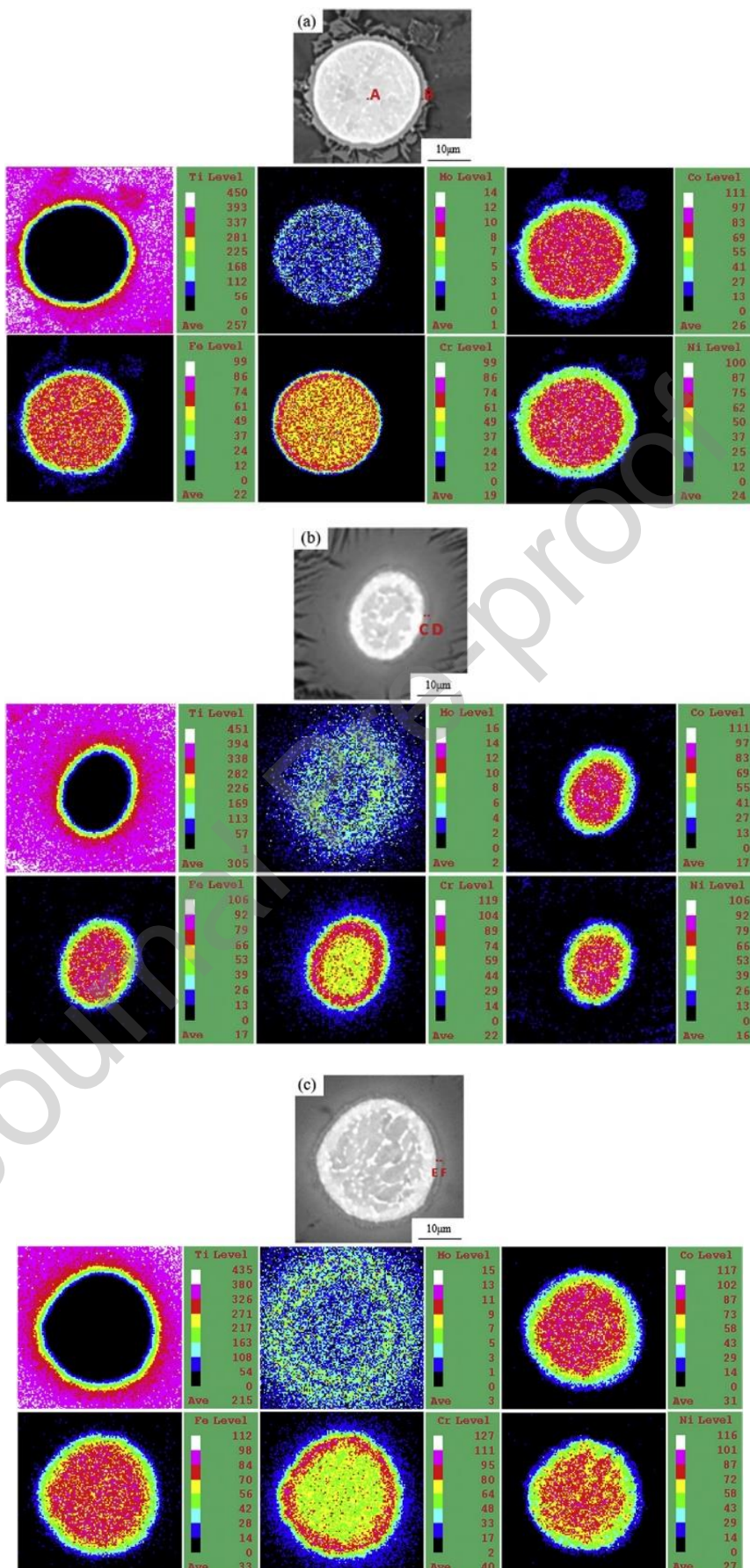


**Fig. 37** Distribution of elements in (a) 700 °C (b) 800 °C and (c) 850 °C sintering temperature [95].

**Table 2** Elemental distribution in diffusion layer [95].

Area	Ti	Co	Cr	Fe	Ni	Mo
A	0.69	23.63	26.75	23.64	20.81	4.58
B	62.86	11.64	3.86	8.97	12.22	0.44
C	35.71	5.60	38.89	11.70	2.56	5.51
D	46.98	4.04	34.74	8.39	2.19	3.66
E	24.79	9.46	38.39	15.73	4.82	6.81
F	38.99	7.93	31.71	13.22	3.88	4.26

Wang et al. [96] fabricated Al-HEA MMC by PM and SPS method with 10, 20, and 30 vol.% of CuZrAlTiNiW HEA to study the mechanical and corrosive properties. **Fig. 38** displays the XRD patterns of the Al-HEA and pure Al composites that were SPS-ed. In addition to the BCC phase and Al matrix, the primary constituents of the composites are the ordered BCC phase, or B2 phase, which is formed in situ, the WAl12 intermetallic compound, and a few other phases that are not yet known. The contents of the B2 and WAl12 phases rise in tandem with increasing HEA volume fractions. It implies that during the sintering process, certain main components of HEA may react with the Al matrix, causing the partial BCC phase to separate and further resulting in the in-situ formation of new phases. A high relative density is achieved in composites, which results in fewer defects or cracks and fewer pores in the material. In HEA 10 wt.% Al composite (**Fig. 39 (a)**) bright-white particle distribution seen in black matrix phase (V) with less than 16  $\mu\text{m}$  size. The composites show an egg-core-shell structure which is easily visible with the yellow line in **Fig. 39 (b)**. Where a bright white "core" I is surrounded by a 4  $\mu\text{m}$  thick "shell" II, the outer layer III surrounds this core shell and has a denser structure as compared to I and II. Some white particles in high amounts are concentrated in layer I and distributed in layers II and III with good agreement to matrix (V) as well. The EDS analysis from **Fig. 39 (b-1 to b-6)** shows equiatomic ratios of constituent elements of HEA in "core" I and confirms the presence of HEA. In the shell region (II) Al became enriched, while poor concentrations of Cu and Ni were found. Al and W are the main elements in region III which formed the WAl12 phase and are found around the HEA. Region III is accompanied by some black regions IV where Ni and Al show presence. **Fig. 40** shows the Al-HEA composite microstructures with 20 and 30 wt % of HEA. The number and intensity of core-shell structure increase due to the presence of a high percentage of HEA particles in the alloy. Region I\* represents euiatomic HEA particles and region II\* shows the presence of WAl<sub>12</sub> which makes strong continued bonds with the matrix as shown in **Fig. 40 (b)**. Region III\* shows a degradative outer dark gray phase similar to shown in the 10 wt.% HEA-Al composite.

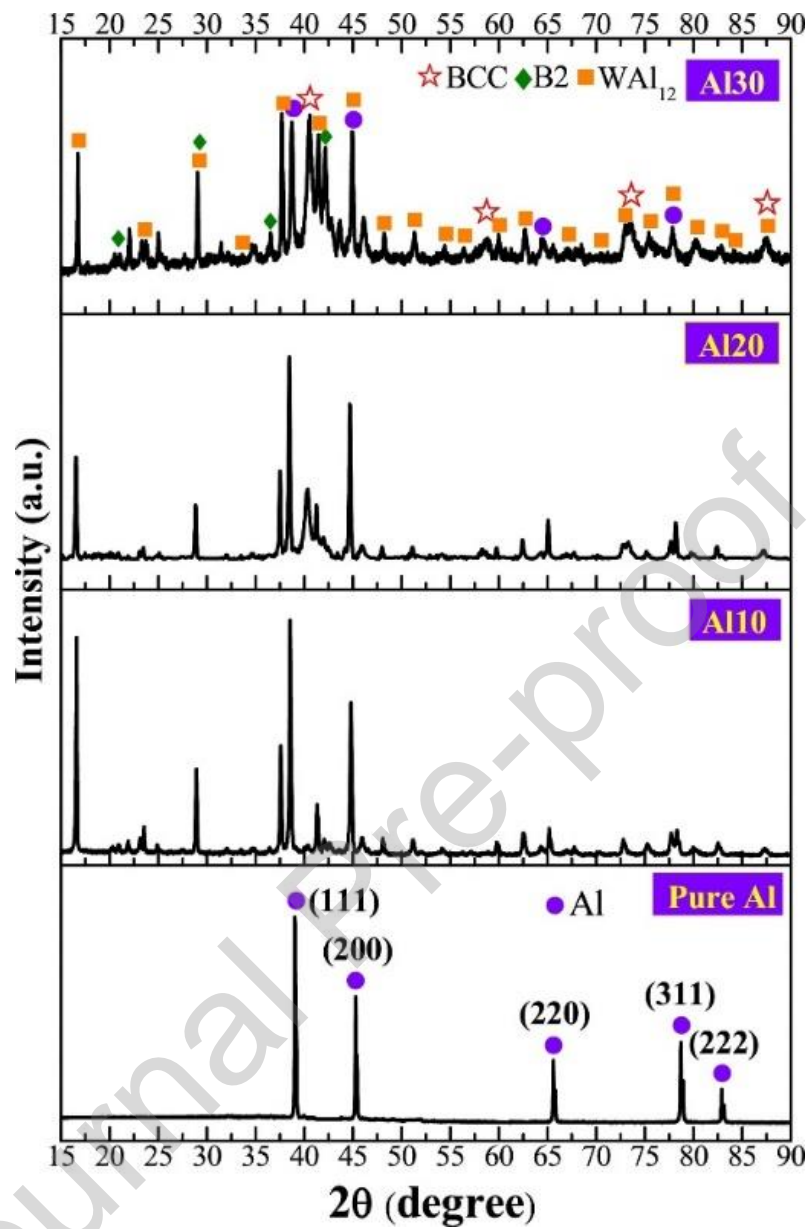


**Fig. 38** XRD patterns of pure Al and Al-HEA composites that were SPS-ed and had varying amounts of HEA reinforcement [96].

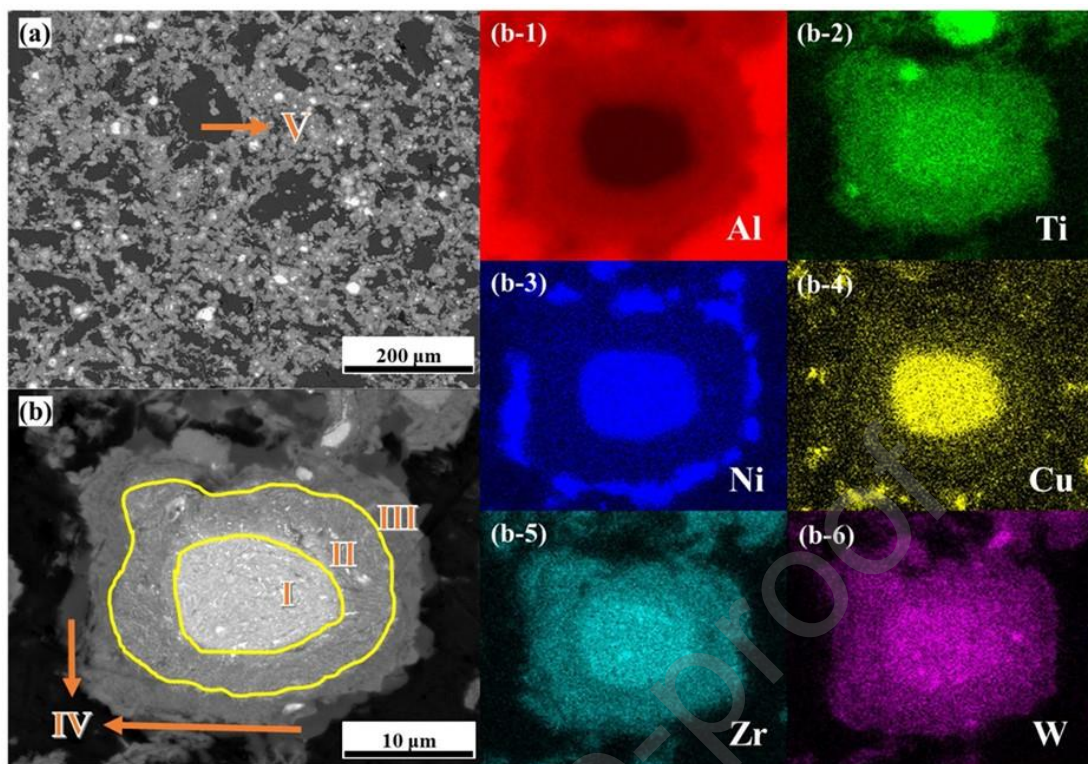


**Fig. 39** (a,b) HEA 10 wt.% Al composite FESEM image and (b-1 to b-6) elemental mapping of (b) [96].

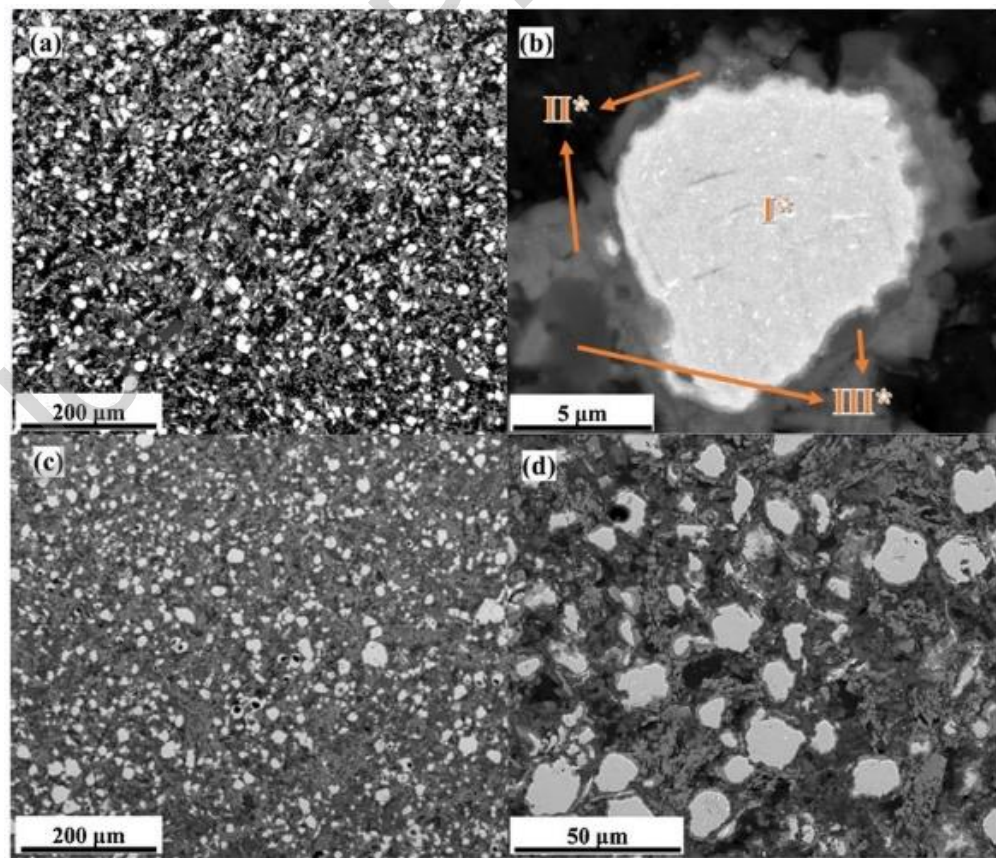


**Fig. 40** FESEM imaging of (a,b) HEA 20 wt.% Al and (c,d) HEA 30 wt.% Al composites [96].

Zhu et al. [97] used SPS and heat treatment process to fabricate HEA-Al composite through Al<sub>35</sub>Ti<sub>15</sub>Cu<sub>10</sub>Mn<sub>20</sub>Cr<sub>20</sub>. The 20, 30 and 40 wt. % HEA was selected for the fabrication of composites. For the SPS method firstly samples were sintered at 540 °C for 10 min. with a heating rate of 30 °C/min and for 15 min. at 500 °C thermal diffusion takes place. Then samples were water-cooled to get core-shell structure in composites. The formation of core-shell structure between the aluminum matrix and HEA core is studied by SEM and TEM. **Fig. 41** represents the SEM images of HEAp and composite having a core-shell structure. HEAps are spheres in shape and about 11 μm in size. In composite, the core-shell particles are uniformly distributed, and it is formed due to elemental diffusion between the aluminum matrix and HEA. The shell is the surrounding area ‘diffusion layer’ of core ‘HEA’. Results show that a very fine layer of the order of 0.4 to 1.6 μm thick cores-shell was established. The diffusion layer volume increases with the volume of the core increase.

**Fig. 42 (a)** shows the TEM imaging of a composite having a core-shell structure, the bright white side shows the presence of an Al matrix, the gray side is the HEA reinforcement particle, and the middle black river region is the diffusion layer between the HEA and matrix. The elemental distribution along the yellow line in **Fig. 42 (a)** is shown in **Fig. 42 (b)**. Elements are distributed but not seen either in the core or in the matrix. The presence of Al in the shell is less as compared to the matrix but high as compared to the core. For the other elements, such as Ti, Cu, Mn, and Cr, the elemental contents in the shell layer are higher than in the Al alloy matrix but lower than in the core. The volume fraction of the shell improves quickly as the volume fraction of the core increases. Elements distributions verify that the atomic diffusion between the Al alloy matrix and the HEA particles forms the shell.

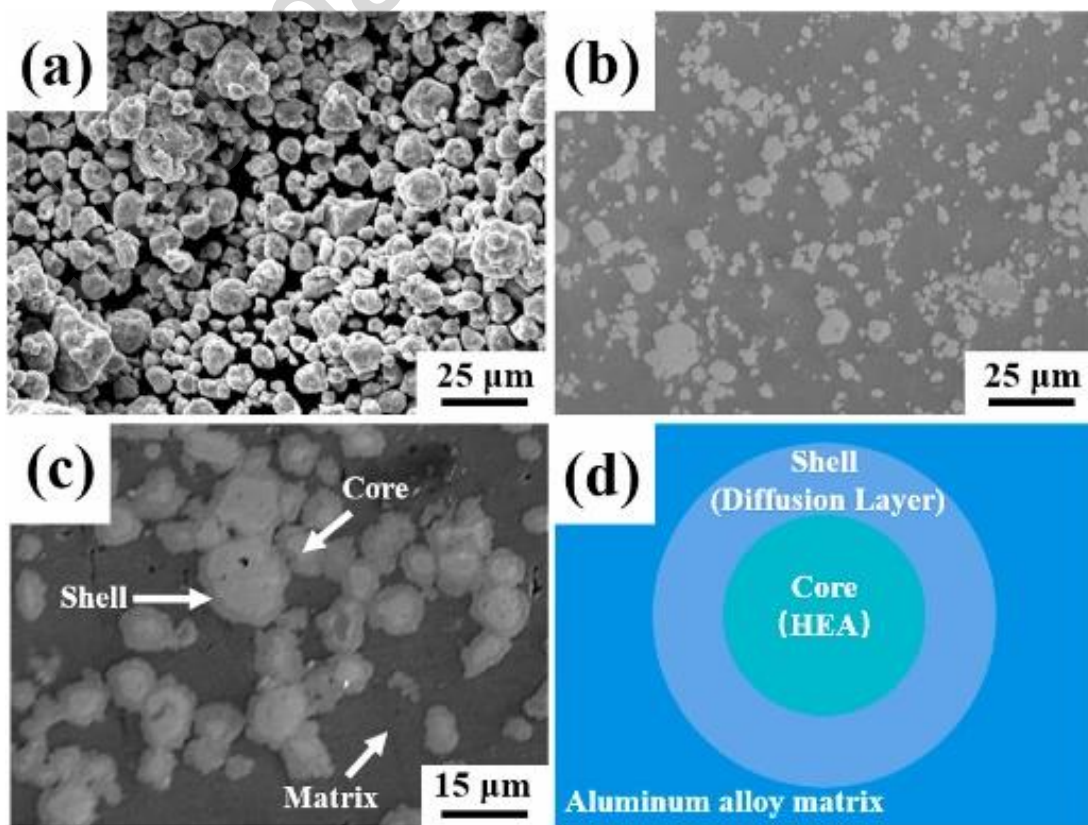


**Fig. 41** SEM image of (a) HEA, (b) 20 wt. % HEA-Al Composite. (c) Core-shell structure at composite, (d) Schematic diagram of single core-shell structure [97].

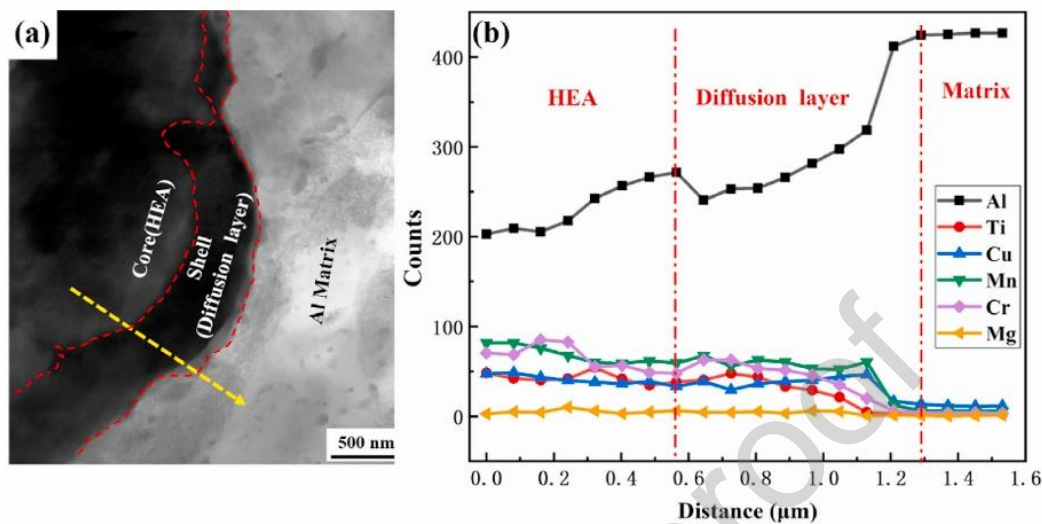


**Fig. 42** TEM image of the core-shell structure formed composite (a) bright field image showing diffusion layer (b) EDS line scene analysis of interface layer between HEA and matrix [97].

The compression study was conducted under dynamic and quasi-static compression conditions. The 30 wt.% HEA-Al composites show better properties as compared to other ceramic-Al composites. At dynamic compression, the highest 602 MPa flow stress and 45.3 % strain to failure, and at quasi-static compression 594 MPa compressive strength, and 26.7 % strain to failure were reported. Maximum hardness of 225 HB achieved at quasi-static compression. A similar study has been performed by Xiao et al. [98] on CoCrFeNi HEA-Al 6061 MMC, Li et al. [99] on  $\text{Al}_{12.37}\text{Co}_{22.96}\text{Cr}_{20.89}\text{Fe}_{21.81}\text{Ni}_{20.42}$  HEA- Al 2024 MMC, Zhang et al. [100] on AlCoCrFeNi HEA-2124 Al MMC, and Salifu et al. [101] on  $\text{Cr}_{20}\text{Mn}_{20}\text{Ni}_{20}\text{Cu}_{20}\text{Nb}_{10}\text{Co}_{10}$  HEA-Al fabricated by the SPS method and then solid solution heat treatment was adopted for the interface formulation study. Satyanarayana et al. [102] uses three different sintering techniques namely conventional, microwave, and spark plasma sintering for fabricating tungsten-based composite by reinforcing the high entropy alloy (CoCrFeMnNi). **Fig. 43** shows the SEM images of the composite and microstructure, which reveal bright, gray and dark shades in the composite, which support the presence of tungsten particles, binder (HEA) phase and oxide of Cr-Mn, respectively. The presence of dark Cr-Mn rich phase observed both in between reinforcement and composite phase along with tungsten particles this is also observed by Moravcik et al. [103] in their study. Compared to conventional and microwave sintering, the average grain of tungsten is refined in SPS, which is due to higher heating rate, shorter holding time and slower cooling of SPS, which stops the grain growth of tungsten particles. Conventional sintering results in grain size at 42  $\mu\text{m}$ , microwave sintering at 33  $\mu\text{m}$  and SPS refining at 15  $\mu\text{m}$ .

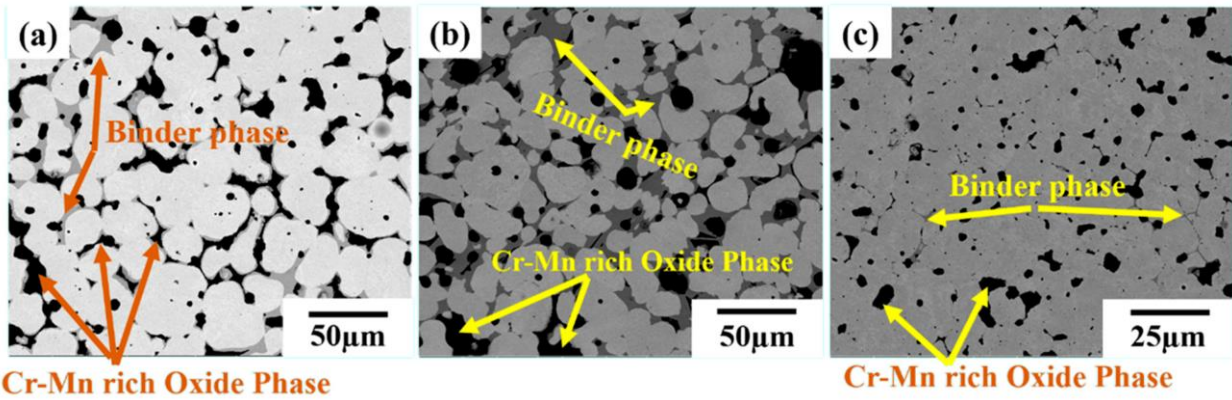


**Fig. 43** SEM of W-HEA composite prepared by (a) Conventional (b) Microwave (c) SPS technique [102].

Tun et al. [104] used microwave sintering powder metallurgy method to prepare magnesium-Al<sub>20</sub>Mg<sub>20</sub>Li<sub>20</sub>Cu<sub>20</sub>Zn<sub>20</sub> HEA alloy with 2.5, 5 and 7.5 wt % HEA content. The composites were homogenized at 400°C for 1 hour in a microwave oven at 640°C before extrusion at 350°C per 8 mm rod at an extrusion ratio of 20.25:1. **Fig. 44** shows the OM images of pure Mg and composites. The presence of HEA alone reduced the grain size of the alloys by only half compared to the pure magnesium matrix, but this was not affected by the content of HEAp in the composite. The distribution of reinforcement was observed in the composites in SEM images (Fig. 74) in which uniformity and homogeneity of particles were seen in all compositions. However, an increasing amount of HEAp addition in the mixture leads to reinforcement clustering. Second, the mechanism of particle-induced nucleation (PSN) in composites results in grain size reduction or refinement. In PSN during hot extrusion, the presence of hard heaps [105] initiates a continuous recrystallization process. A high strain gradient occurs around the hard particles in the composite due to the plastically deformed matrix and non-deformed hard heaps during the hot extrusion process. This results in the development of a high dislocation density, also known as a deformation zone, around each particle. These zones have become the perfect location for new grain production. PSN requires the use of a reinforcement particle larger than 1 μm in size [106]. In the present study a reinforcement of 1.5 μm particle size is used, which acts as a nucleation site for new grains after heat transformation [107].

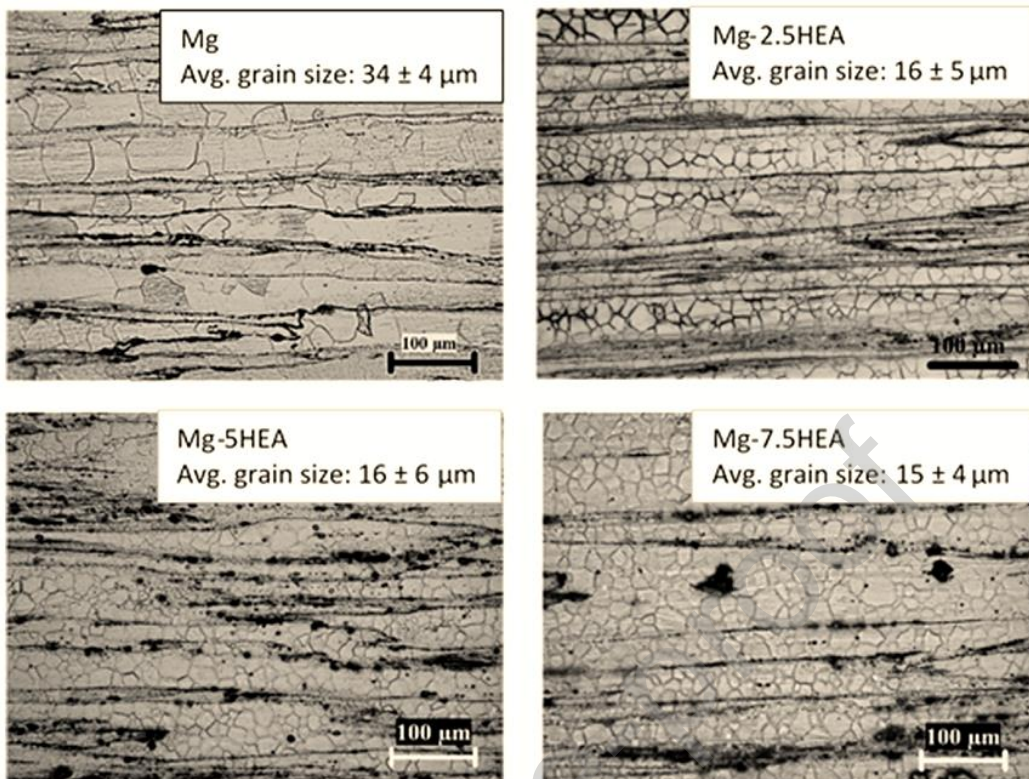


**Fig. 44** Grain size evaluation of monolithic Mg and Composites [104].

Chen et al. [108] have studied the behavior of copper matrix with TiZrNbTa (HEA) to find high strength and electric conductive properties in composite fabricated through the SPS method. Mechanical properties with variation of electrical conductivity and microstructural analysis were done with various composites (0, 10, 20, 30, 40, and 50 wt. % of HEA). The high pressing and low temperature of the sintering process of the SPS method reduces the interdiffusion gap between the HEA and Cu phases [109]. **Fig. 45** represents the SEM images of the HEA-Cu composite with 1, 30, and 50 wt. % HEA content along with the magnified SEM of the local surface area of the 50 wt.% HEA-Cu composite. Point EDS was also observed at point A of the Cu site and point B of the HEA site in the 10 wt.% HEA-Cu composite. The results show that copper is 98.75 wt. % at points A and Ti, Zr, Nb, and Ta are 23.60, 25.18, 25.92, and 25.02 wt. % at point B, respectively. The SEM and EDS in **Fig. 46** of 30 wt. % HEA-Cu composite show the presence of TiZrNbTa HEA elements with a bright phase and Cu with a dark phase. HEA is evenly distributed in the matrix with a size of less than 10 $\mu$ m and forms a good solid solution with the Cu matrix, resulting in a high density, low defect, and low pore composite. EBSD test of 0, 10, and 30 wt.% HEA-Cu composite shows the presence of HEA phase in the colored grains and black regions of Cu in **Fig. 47 (a, c, e)**. The generation of residual stress after HEA addition was studied by kernel average misorientation (KAM) maps and represented in **Fig. 47 (b, d, f)**. The green color indicates high residual stress spots in the composite, which increase as the HEA content increases, and the blue color indicates the low residual stress region indicating the presence of the Cu phase.

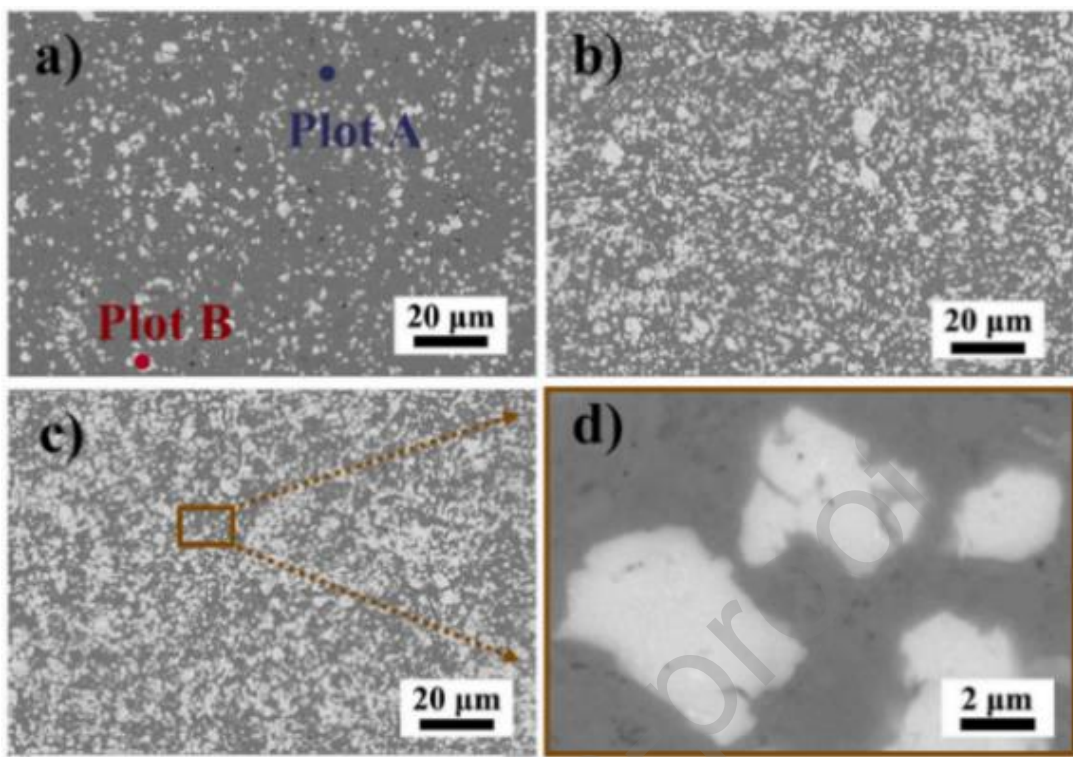


**Fig. 45** SEM image of (a) 10, (b) 30 and (c) 50 wt.% HEA-Cu composite and (d) local SEM in high magnification [108].

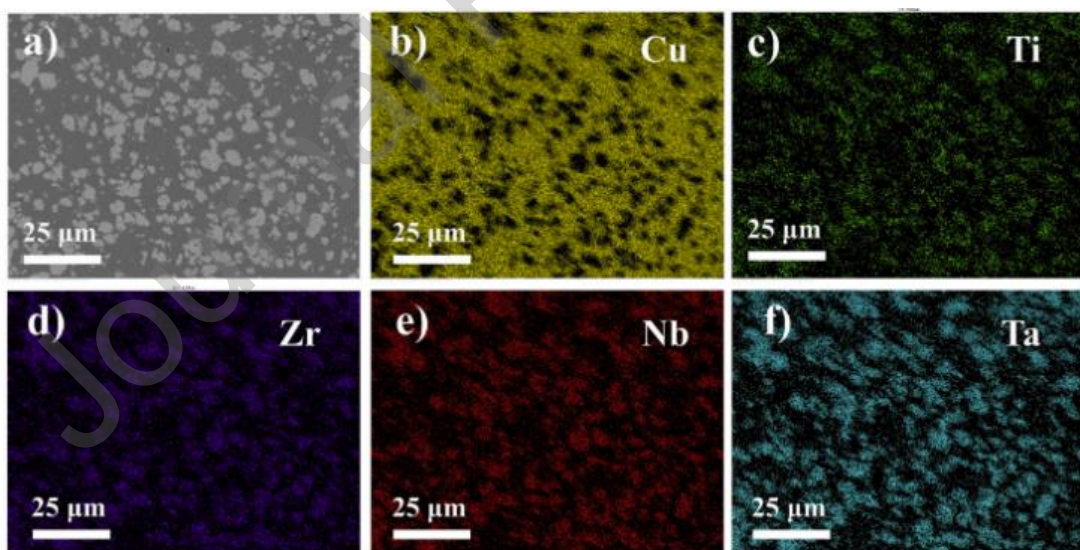


**Fig. 46** SEM (a) and EDS (b-f) of 30 wt.% HEA-Cu composite [108].

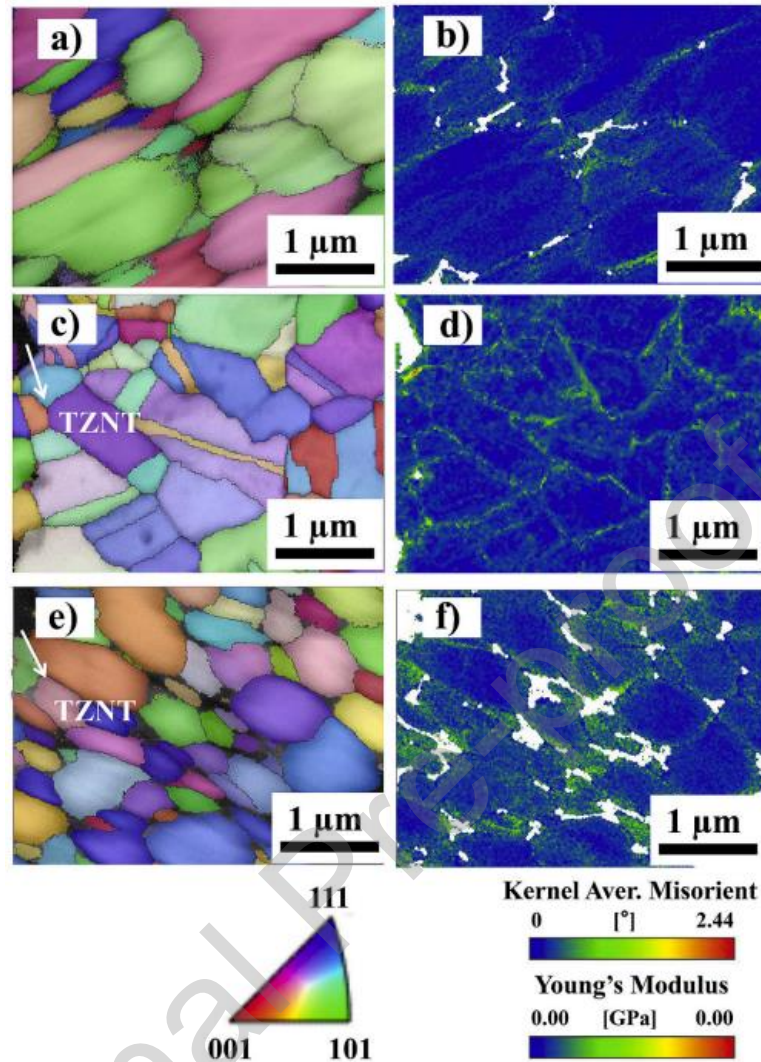


**Fig. 47** EBSD and Kernel Average Misorientation (KAM) map of (a, b) 0, (c, d) 10, and (e, f) 30 wt.% HEA-Cu composite [108].

Yang et al. [110] used a cooling-assisted friction stir processing (FSP) method to fabricating Al-HEA composite materials. In the Al-5083 matrix, different percentages (5, 10, and 15 wt %) of AlCoCrFeNi HEAp reinforcement were embedded with an average particle size of 25  $\mu\text{m}$ . Blind holes were made on the surface of aluminum plate and filled by HEA reinforcement particles. Five passes of the FSP tool with an inclination angle of 2° were made on the top of the composite plate to seal the holes. The influence of the distribution of coaling-assisted FSP and HEAs was examined by OM, SEM and EBSD results, and the distribution of the elements present was observed by EDS study. Figure 48 shows SEM and OM analysis of the retarding, advancing side, and top, middle, and bottom of the 15 wt % HEA reinforced composite. Homogeneous distribution of HEAs on Al-HEA composites can be achieved by cooling assisted FSP method. In the fabrication composite, two mechanisms of FSP operate, one is the frictional thermal formation of the plastic flow of the aluminum matrix and the second is the stirring action of the FSP tool. Mechanical stirring of the FSP tool moves the aluminum matrix from advancing to retarding side. On the

other hand, a stirring FSP tool contacts the material, which applies pressure and generates frictional heat in the composite, it ensures uniform mixing of reinforceed HEAp with the aluminum matrix in the composite system [111, 112]. In FSP the temperature distribution is always higher in the contact area of tool and material (advancing side) than on the non-working side (retreating side). But the continuous multi-pass movement of the tool makes a uniform distribution of temperature from the developing side to the retarding side. Thus canceling the temperature difference on both sides and equal distribution of HEAp over the stir zone is achieved in the composite [113, 114]. So the integrated combination of mechanical stirring and forward-backward motion of the FSP tool provides uniform distribution of HEAps and temperature in the composite material. They observed that the friction between the contact area of the tool and the heated material allows plastic flow of the aluminum matrix, and the pressure of the FSP tool helps distribute the HEAp uniformly over the matrix. Figure 49 (a-c) shows SEM analysis of HEA-Al alloy with different wt % (5, 10 & 15) of HEA. It is observed that the HEAp is distributed in all directions in each region of the test side and no site has the presence of HEAps and no clustering of HEAps occurs. The composite density increases with increasing HEA wt % particles and the spacing between each particle decreases. The load-depth curve in Fig. 49 (d) shows the nanoindentation on the HEA and base metal surface. The results indicate that the nano-hardness of 7.6 GPa and elastic modulus of 184.1 GPa HEAp is higher than the aluminum matrix with nano-hardness of 1.3 GPa and elastic modulus of 88.9 GPa.

Uniform distribution of HEAps and formation of interfacial bond between matrix and HEA reinforcing agent is also a key mechanism for improved surface property. Figure 50 shows SEM and EDS analysis of 1.5 wt % Al-HEA alloy used to study interfacial properties and elemental mapping. They reveal that no voids and pores are formed at the interface, which reflects the good quality of the bond between matrix and reinforcement, and no detectable reaction byproducts appear at the junction of HEA reinforcement and composites. This observation stems from the relatively low processing temperature of FSP, which combined with efficient cooling reduces heat input. In addition, the high melting point and slow diffusion of HEA reinforcement help prevent significant interfacial reactions. The HEA particle elements diffusion reacts with the matrix material, thereby easily transferring the load from the soft matrix to the hard reinforcing agent. The load transfer strengthening mechanism takes place in this interdiffusion bond. The increase in microhardness can be attributed to the addition of HEAp, grain refinement and interdiffusion bonding. This increases the dislocation resistance between particles and provides geometrically required dislocation reinforcement. The low thermal imbalance between the HEAd and the matrix and the elastic modulus coefficient create a high dislocation density around the HEA particles. Interface bond formation also makes it easier to avoid any fracture in the composite material during loading, this helped prevent the HEA and matrix particles from separating from each other. It is difficult to stop the reactions between hard HEA and soft matrix interface in FSP composite fabrication, but coaling-assisted FSP can easily precipitate in the matrix to form MMCs in hard HEAps.

Figure 51 shows the EBSD analysis of composites with different wt. % HEAp. With the incremental addition of HEAp (5, 10 & 15 wt.%) through cooling assisted FSP process, the composite grain size is equiaxed and fine compared to the previous composite. The FSP process produces a high strain rate and temperature that results in increased dislocation mobility in the presence of HEA to improve the microstructure through recrystallization. HEAs have a grain size greater than 1  $\mu\text{m}$ , for which the PSN mechanism plays a key role in developing dynamic recrystallization in the composite. The cooling assisted friction stir processing (CFSP) method uses cooling aid to obtain advantages compared to FSP because it reduces the time to produce recrystallization, which improves the grain size of the composites. The grain size of the composite is refined by adding HEA particles to 1.8  $\mu\text{m}$ , 1.4  $\mu\text{m}$  and 1.1  $\mu\text{m}$ , which are 5 wt. %, 10 wt. % and 15 wt. %, respectively. This reduction in grain size is attributed to the availability of more nucleation sites during the FSP process due to the HEA grain size greater than 1  $\mu\text{m}$  as observed in the PSN mechanism.

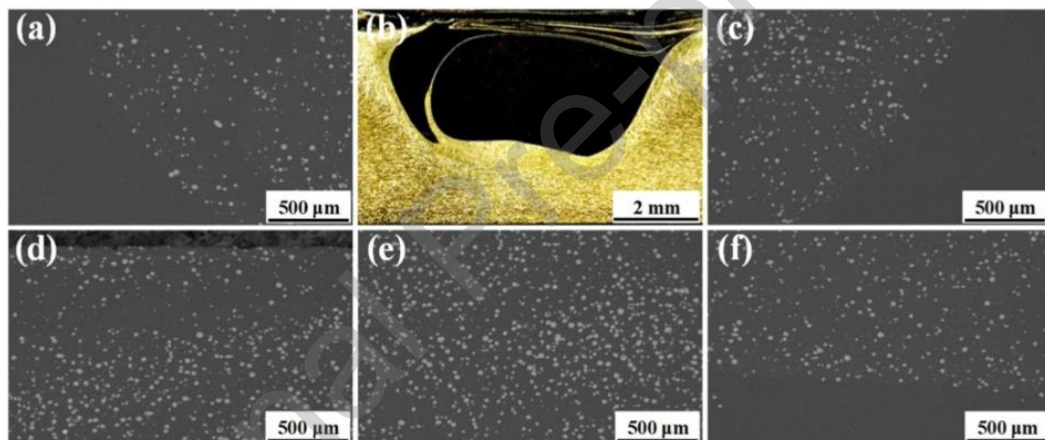


**Fig. 48** SEM image of 15 % HEA-Al composite at (a) retreading side (b) OM at surface (c) SEM at advancing side (d) top portion, (e) middle portion, and (f) bottom portion [110].

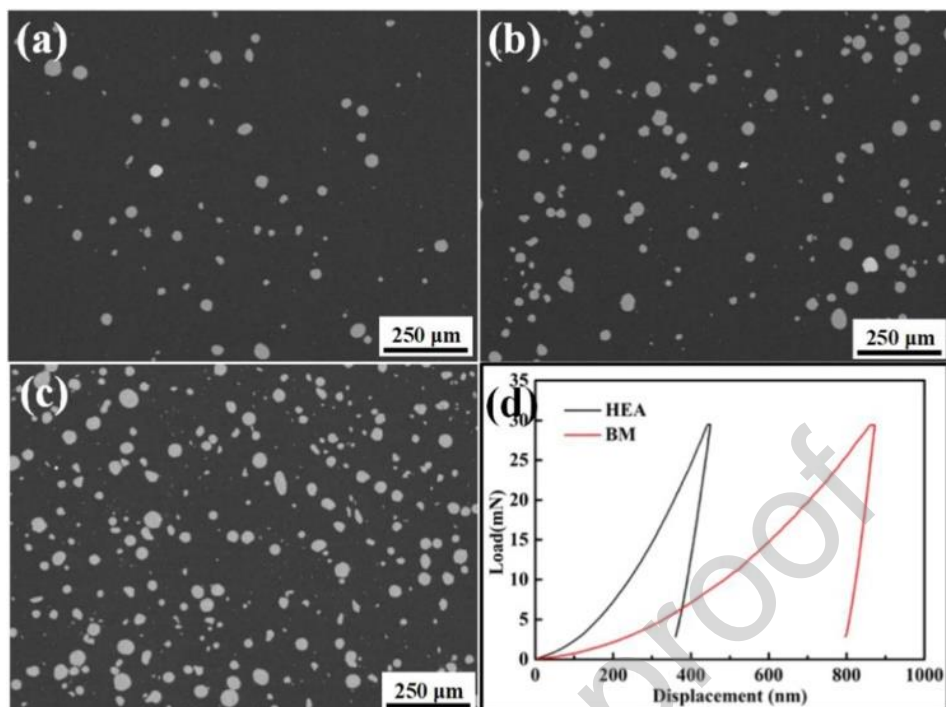


**Fig. 49** SEM images of composite at (a) 5 wt. %, (b) 10 wt.% (c) 15 wt.% HEA content on aluminum matrix composite [110].

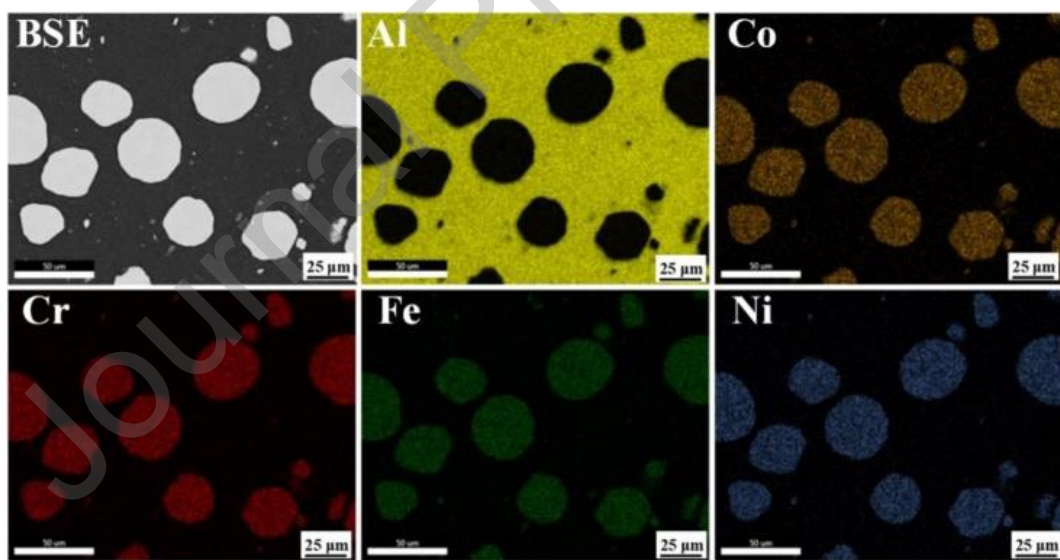


**Fig. 50** SEM and EDS elemental mapping of 15 wt. % HEA-Al composite [110].

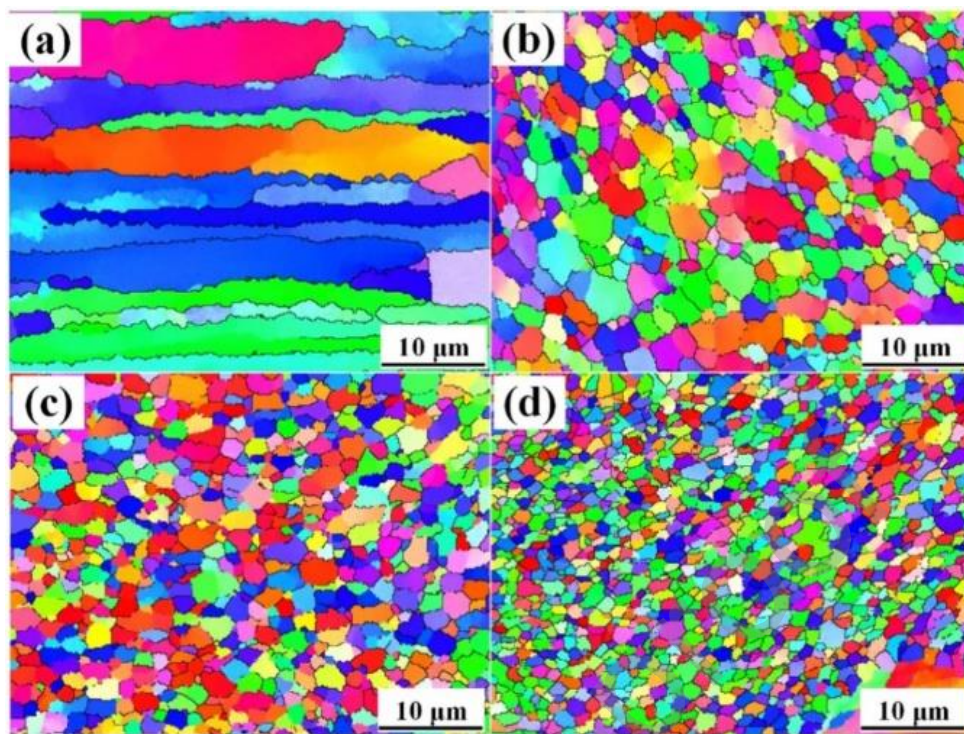


**Fig. 51** EBSD images of composite at (a) 0 wt. % , (b) 5 wt. % (c) 10 wt. % (d) 15 wt. % HEA content [110].

**Table 3** Comparative XRD results for HEA-MMCs.

S. No.	References	Matrix	Reinforcement	XRD results
			HEA	
1.	Ananiadis et al. [33]	Aluminum 1050	MoTaNbVW	<ul style="list-style-type: none"> <li>With the addition of HEAp peaks intensity of Al reduces.</li> <li>Peak intensity of HEA increases with increase in HEA wt.%.</li> <li>Small peak BCC MoTaW and NbV phase.</li> <li>High Peak FCC Al phase.</li> </ul>
2	Prabakaran et al. [32]	Aluminum 6061	CrMnFeNiCu	<ul style="list-style-type: none"> <li>Low peaks corresponds to BCC phase (HEA) and high peaks to FCC phase (Al).</li> </ul>
3.	Yuan et al. [91]	Aluminum 2024	CoCrFeMnNi	<ul style="list-style-type: none"> <li>Al atoms reacts with Mn and Cu atoms to form new <math>\text{AlCu}_2\text{Mn}</math> and <math>\text{MnAl}_6</math> phases along with Al &amp; HEA.</li> </ul>
4.	Liu et al. [93]	Aluminum	AlCoCrFeNi	<ul style="list-style-type: none"> <li>Presence of BCC phase in HEA &amp; at transition layer FCC phase was found.</li> </ul>

5	Yuan et al.	Aluminum [94]	$\text{Al}_{0.6}\text{CoCrFeNi}$	<ul style="list-style-type: none"> <li>Single BCC solid solution phase of HEA and mixed Al, Al (Co,Fe) and Al12Mg17 phases shown during sintering process.</li> </ul>
6	Yuan et al.	Titanium [95]	$\text{CoCrFeNiMo}_{0.2}$	<ul style="list-style-type: none"> <li>At 76° FCC Ti phase is present.</li> <li>New phase formed at 43° and 50° after sintering of HEAs.</li> <li>At high temperatures (800 and 850 °C) <math>\text{TiCr}_2</math> and CrMo found.</li> </ul>
7	Wang et al.	Aluminum [96]	$\text{CuZrAlTiNiW}$	<ul style="list-style-type: none"> <li>In addition to BCC HEA and Al matrix phase, in-situ formed B2 and WAl12 are present in composite</li> </ul>

#### 4. Effect of HEA reinforcement on mechanical properties

As discussed earlier, to obtain the desired mechanical properties of metals, researchers have designed composite materials by incorporating reinforcements such as ceramic particles and high entropy alloys. The concentration of HEAs in composite and composition techniques determines the mechanical properties such as high hardness, high stiffness, good strength, good ductility and good resistance to wear, and corrosion. The following sections discuss the improvement of hardness, strength, corrosion, and wear.

##### 4.1 Towards the hardness enhancement:

This section provides an overview of matrix hardness enhancement through reinforcement. Various authors have reported an improvement in hardness when preparing MMCs reinforced with high entropy alloys and provided mechanisms of improvement.

Prabakaran et al. [32] studied aluminum 6061 matrix composite reinforced by CrMnFeNiCu HEAp fabricated through powder metallurgy route. Composites prepared by 10 and 20 wt.% HEAp at different sintering temperatures (560 & 600 °C) and soaking time (1 & 2 h) and with different properties were evaluated. It is observed from Fig. 52 (a) that increasing the sintering temperature and soaking time decreases the density of both matrix and composite. Aluminum 6061 matrix shows higher density compared to others at given sintering temperature and time. The small grain size HEA was homogeneously distributed in the mixture by using the PM method. Sintering the Al-6061 matrix without HEAs above its recrystallization temperature of 250 °C brings the elements in the matrix to a higher dispersion, resulting in a higher density material compared to the composite. HEAs in the PM method provide resistance to compaction, thereby creating a weak bond between the HEAp and the matrix. But sintering with higher temperature brings about the diffusion of elements to form strong bonds, resulting in a dense structure less than 3.5% in the 20 wt.% Al-HEA composite. Figure 52 (b) shows that the addition of HEA reinforcement particles in the matrix

increases the composite porosity. However, porosity decreases with increasing sintering temperature and soaking time, which was found to be 35% and 5–10% for matrix and composites, respectively.

An increase in sintering temperature and time shows a positive response in enhancement to the hardness of the composite as shown in Fig. 53 (a). A microhardness of matrix 59 HV is observed at 560 °C sintering temperature and 1-hour soaking time, while 18% hardness (73 HV) improvement is found when aluminum matrix is sintered at 600 °C for 2 hours. As previously discussed, reduced porosity and improved bonding at matrix-reinforcement interfaces are the reasons for improved hardness in composite materials. The microhardness values of 10 (~120 HV) and 20 (~135 HV) wt.% Al-HEA comosite are higher compared to the base aluminum alloy (73 HV) due to the presence of hard particle in HEA. The composites are less dense, but due to the smaller grain size of HEAs, there is more interface between the matrix and the reinforcement, which in turn generates more sites to form stronger bonds with higher strain energy at the interface. Furthermore, the uniform distribution of reinforcement particles provides resistance to indentation during the microhardness test. The overall composite hardness is higher due to the harder elements of HEA compared to the softer Al matrix.

The response of sintering temperature and soaking time variation with compressive strength of Al-6061 matrix and composites is shown in Fig. 53(b). The compressive strength of matrix and composites increased with increase in soaking time at constant sintering temperature. The compressive strength of the composites increased by 18–35% compared to the matrix due to lower voids and porosity and improved interfacial bonding. The addition of HEAs provides improved hardness and the presence of a stable BCC strong phase in the HEA gives strength to the matrix. The improved mechanical properties of the constituent elements of HEA increase the compressive strength in the composite. It was revealed that Al-10 wt.% HEA composites show better compressive strength than Al-20 wt.% HEA composite and matrix. Incorporation of high amount (20 %) of HEAs with aluminum matrix results in more strain energy at grain boundaries and more cracking when load is applied. It was found that Al-10 wt.% HEA composite shows better load transfer strengthening mechanism compared to other composites and matrices.

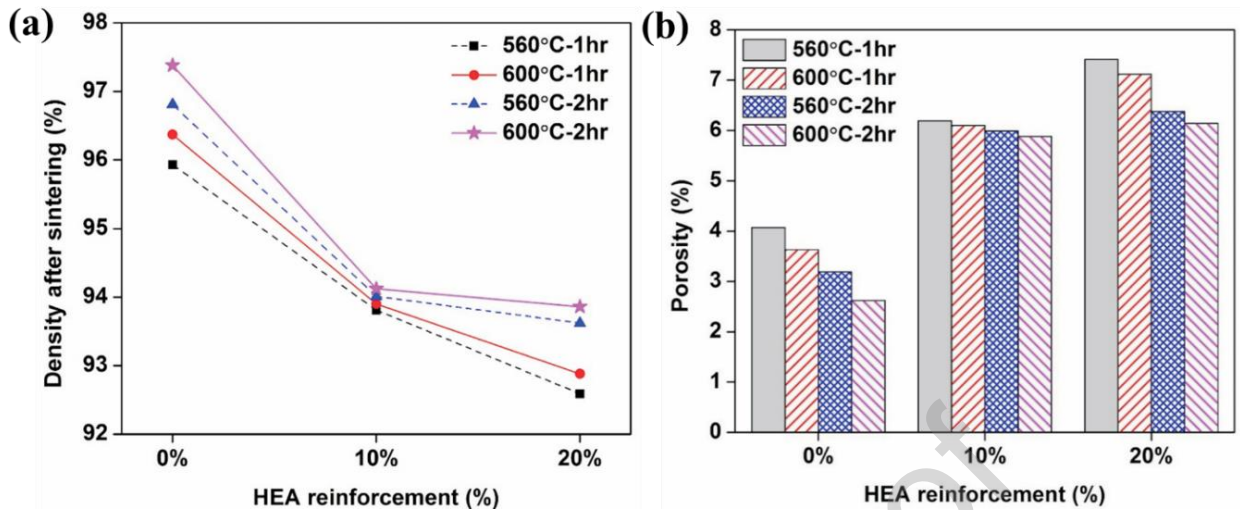


**Fig. 52** Changes in (a) Density and (b) Porosity of composites after sintering and soaking time [32].

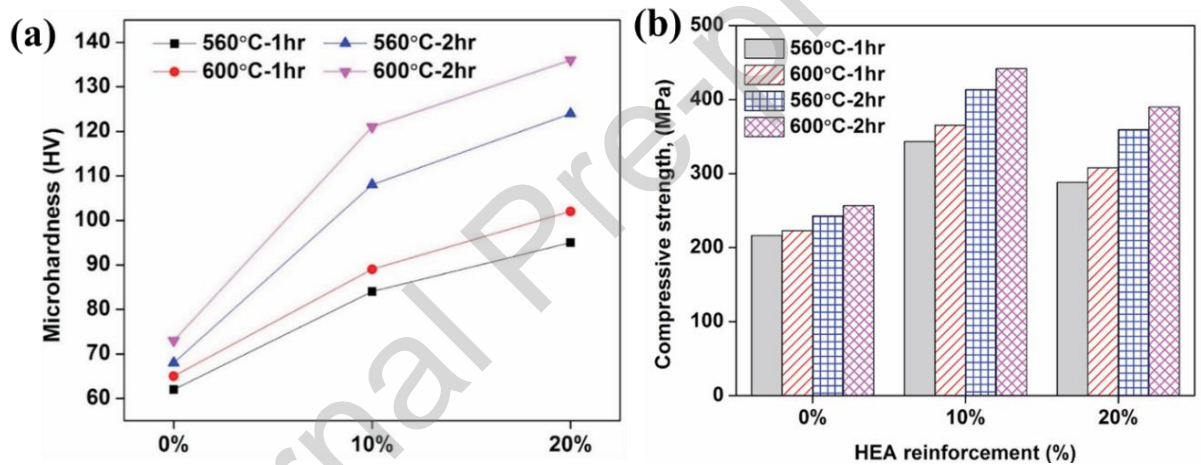


**Fig. 53** (a) Hardness and (b) Compressive strength of composites at different HEA wt. % [32].

Ananiadis et al [33] studied the aluminum matrix reinforcement with MoTaNbVW HEA particles prepared by powder metallurgy method. The SEM images of the composites were correlated with the increase in hardness values (**Fig. 54**). In the microstructure SEM imaging analysis of the HEA-Al composites, homogeneous distribution and uniformity of HEAp on the aluminum matrix was seen. The hardness of the composite increases with increasing wt.% HEA content due to the presence of this hard reinforcement HEAp. The Rockwell B hardness of HEA was reported to be  $97 \pm 4$  HRB [98], while the hardness of the pure matrix was only 41 HRB, an increase in the HEA-Al alloy was observed in the test. Other reasons for the increased hardness in EDS imaging are the quality of integration at the reinforcement-matrix interface and high interfacial bonding with no pores and less disintegration.

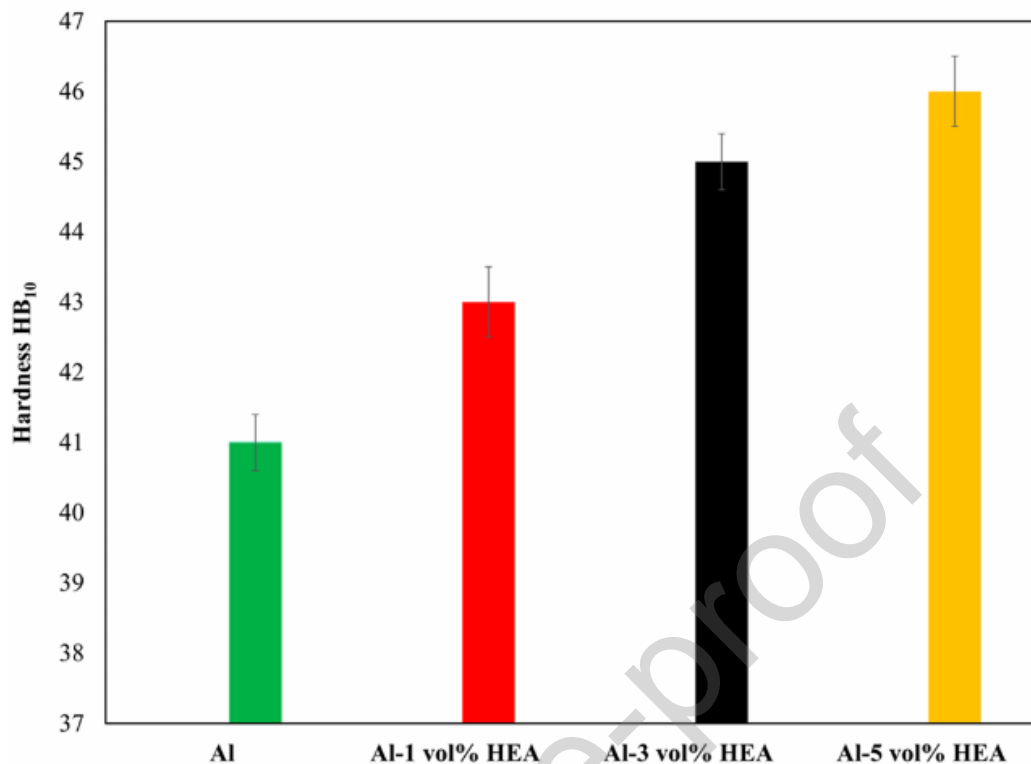


**Fig. 54** Hardness variation of composite with addition of HEAp in matrix [33].

Zhang et al. [54] fabricated HEA-MMC to evaluate the mechanical properties of AA2219 matrix reinforced by AlCoCrFeNi HEAp with an average size of  $8.11\text{ }\mu\text{m}$  by ultrasonic assisted stir casting route. The SEM and XRD were performed to analyze the microstructure and to identify the phase of the material respectively. The hardness was evaluated for different wt. % (0, 0.25, 0.5, 0.75, 1.5, 3.0, 5.0) HEA-MMCs as shown in **Fig. 55 (a)**. The hardness of AA 2219 was observed 82.4 HV and further, the hardness of the material was reported to increase with the addition of HEAp. The optimum hardness of composite was found at 3wt% HEA-AMC, which is 46.3 % higher form alloy. The presence of HEA in the alloy hardness decreases after 5 wt.%, but it is more than 30% in the pure Al alloy. By comparing maximum harness achievement in 3 wt.% HEA-AMC of Al alloy it is clear that HEA zone has much improved harness in the range of 30-60% **Fig. 55 (b)**. The hardness enhancement shows the presence of HEA in the aluminum matrix. HEAp diffuses onto the  $\alpha$ -Al matrix and thus produces lattice distortion resulting in enhanced hardness.

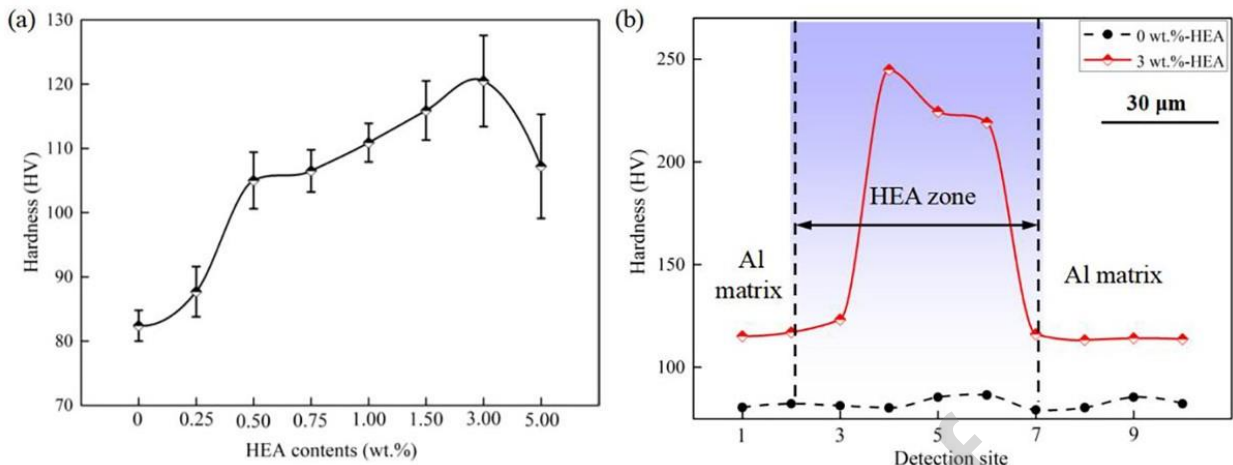


**Fig. 55** (a) Hardness of AMC with different wt.% of HEAp, (b) Comparison of hardness of Al and 3 wt.% HEAp-AMC [54].

Zhang et al. [55] examined the mechanical and tribological properties of high entropy alloy aluminum metal matrix composite (AA2219- Al<sub>0.5</sub>CoCrFeNi HEA) fabricated by ultrasonic stir casting method. **Fig. 56** below shows the hardness values of AMC as affected by HEAp (0.5, 1.5, 3.0, and 5.0 wt.%) content. The hardness of monolithic AA2219 is 82.4 HV and it increases after incorporation of HEAp into AA2219. The optimum hardness of 120.5 HV was found at 3 wt.% HEAp-AMC, which was about 46.2% higher than that of the aluminum matrix, and then the hardness declined with 5 wt.%. The suggestive reason for the improvement in hardness can be explained by the SEM image of 3 wt.% HEA-AMC. The white grain boundaries showed the presence of Al<sub>2</sub>Cu phase and the agglomeration of HEAp found in the form of clustered gray phase. This HEA particle agglomeration increases with the wt.% HEA in aluminum and acts as a binder for the increase in hardness.

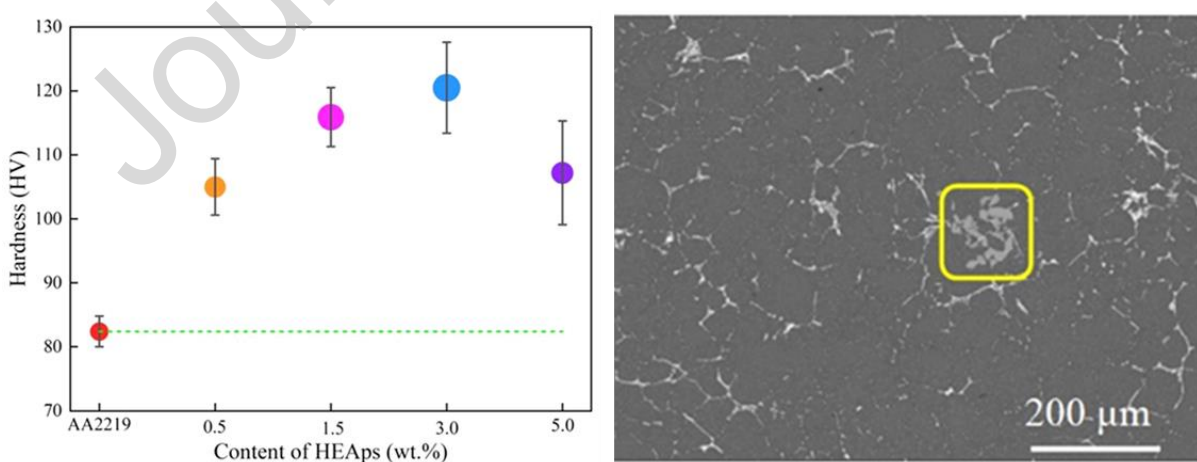


**Fig. 56** Hardness versus wt. % of HEAp and SEM image of 3 wt.% HEA-AMC [55].

Yuan et al. [91] used SPS method to fabricate HEA-Al MMC and ID mechanism layer was discussed in detail. The hardness of the composite through the ID layer along with the indentation test along with the Young's modulus was also examined and shown in **Fig. 57 (a, b)**. The average hardness of the HEA was

found to be 7.5 GPa higher than that of the ID layer. The hardness decreases and a larger indentation appears in the ID layer because HEAp diffuses in a matrix with lower hardness compared to HEA. As the indentation approaches the matrix the HEA elements become less marked, the distance from the HEA increases and the hardness decreases. From the Vickers hardness test of 50 gf load, 63.7% hardness improvement was found in the composite as compared to the matrix material. There are two reasons reported that the first addition of HEA reinforcement results higher hardness exposed the composite compared to the matrix and the second expansion of the ID layer by the SPS method makes the ID layer uniform and dense. Therefore, that the indentation load stress is distributed and the load bearing capacity of the composite is improved. On the other hand, the compounds formed in the ID layer control the dislocation motion of the material, hence increasing the toughness of the alloy.

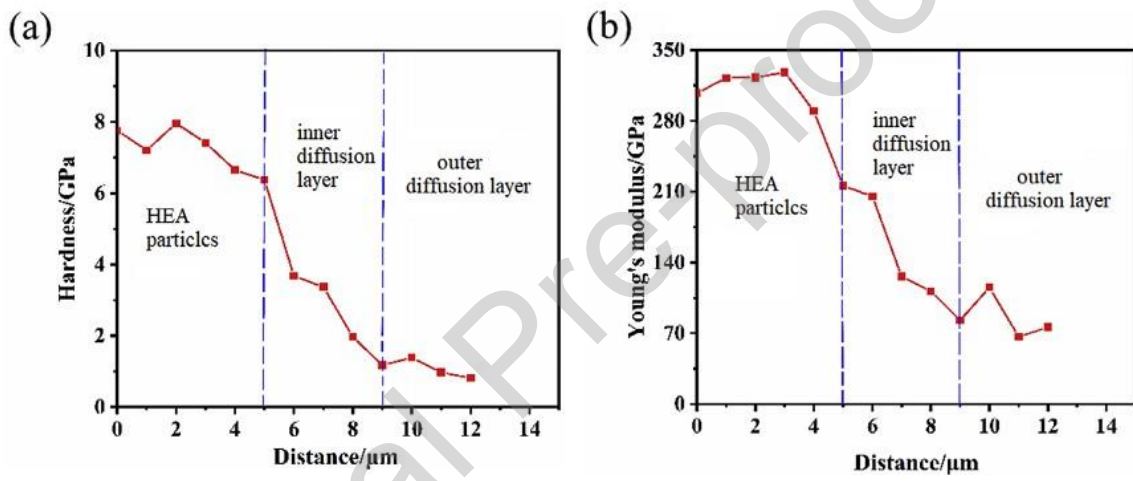


**Fig. 57** (a) Hardness and (b) Young's modulus of composite material through ID layer [91].

Yuan et al. [94] used vacuum hot pressing sintering method for fabricating AMC reinforced by  $\text{Al}_{0.6}\text{CoCrFeNi}$  HEAs. After heat treatment, the interface layers between the HEA and the matrix were detected and the variation in hardness linked to the composite microstructure was examined. **Fig. 58 (a)** shows hardness and **Fig. 58 (b)** represents Young's modulus variation in different positions in the composite. The hardness of HEA is higher than that of the interface layer and matrix, little change in hardness is seen from HEA to the interface layer, but drastic change is seen in the matrix. The average hardness of 12 GPa of HEA at the start of the interface layer decreases and becomes constant at 6 GPa due to the presence of a weak matrix. As the indentation progresses to the matrix phase, the hardness decreases to 1.8 GPa. The same is the case with Young's modulus, the value of Young's modulus at the beginning of the interface from the HEA side is 280 GPa, which is much higher than that from the matrix side. In the interface layer, it varies from 145 to 120 but remains constant up to 80 GPa at the end of the interface layer from the matrix side.

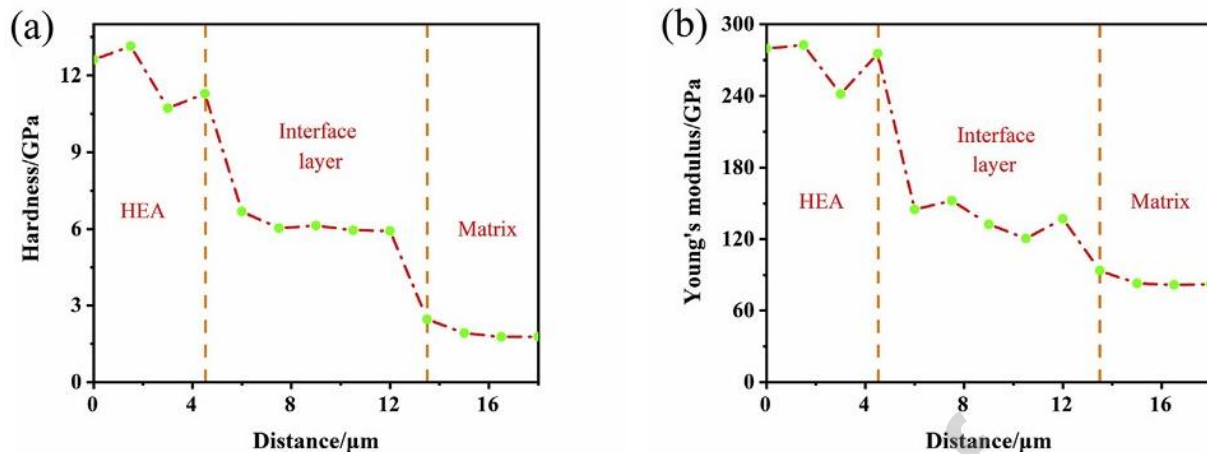


**Fig. 58** (a) Hardness and (b) Young's modulus of composites treated at 500 °C in 12h sintering time [94]

Praveen Kumar et al. [116] fabricated Al-2014 aluminum-based composite using reinforcement of ternary HEA by stir casting method and results revealed that the hardness of Al-20Cu-10Mg HEA (5, 10, and 15 wt.%) composite increased with an increasing wt.% of HEAs particles as shown **Fig. 59**. They found an overall hardness increase of 63% after adding Al-20Cu-10Mg HEA (5, 10, and 15 wt.%) to Al-2014. This increase in hardness is due to the interfacial bonds between the matrix and reinforcement particles, the refined grain size of the matrix and the size of the reinforcement. Displacement constraints of interparticle distance, controlled dislocation mobility of grains, matrix deformation and enhanced dislocation density impose enhanced hardness during composite hardness testing. All these hardness enhancement results support the presence of HEAp and its solubility on the matrix.

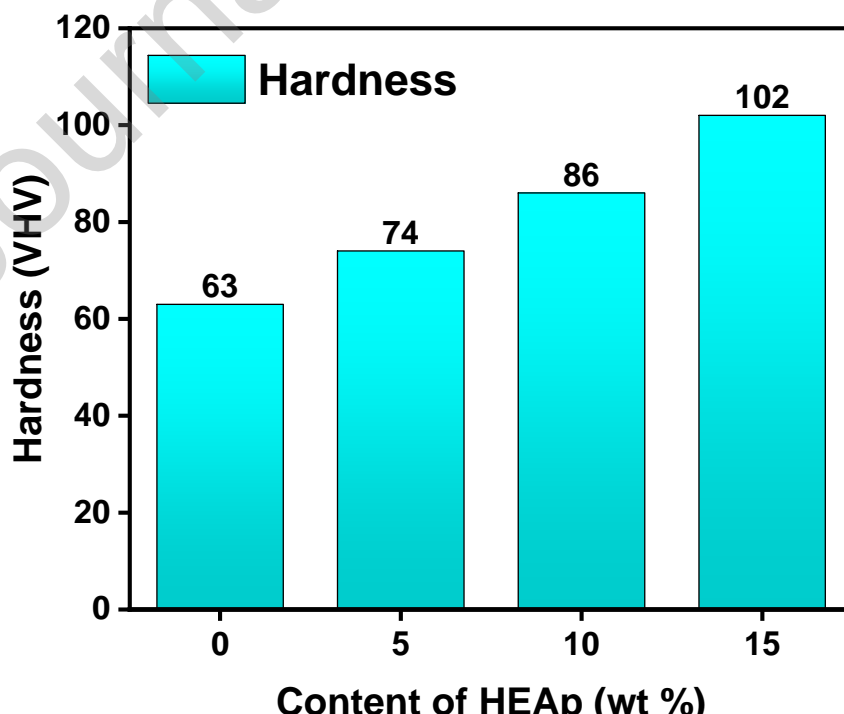


**Fig. 59** Hardness variation with reinforcement addition [116]

Wang et al. [96] fabricated HEA-Al MMC by PM SPS method with 10, 20 and 30 volumes of CuZrAlTiNiW HEA to study the mechanical and corrosion properties. **Fig. 60** shows the improved microhardness of Al-MMC with increasing content of reinforcing HEAp from 10, 20 and 30 wt.%. The highest microhardness of 331 HV was found at 30 wt.% HEAp, which was about 10 times higher than that of pure Al (34 HV). After proper mixing, homogeneity of HEAp was achieved in the mixtures. During the sintering process, Al atoms interdiffuse at the Al matrix/HEA interface due to the distinct difference in Al concentration between HEA reinforcement and pure Al matrix power. It is widely accepted that high entropy alloys (HEAs) exhibit low thermal conductivity. The pure Al matrix has a higher thermal conductivity of 217.7 W/m·K when compared to HEAs, indicating that the Al particles transfer heat more rapidly in the inter-particle regions. In the alloy during sintering, the Al atoms of the matrix diffuse into the reinforcement due to their strong diffusion ability, then the Al atoms react with the constituent elements of CuZrNiAlTiW HEA to form in-situ WA12 and NiAl-rich B2 phase, and they surround the BCC-HEA particle. All these reasons make the quality of sintered products with dense structure. XRD and FESEM image analysis concluded the formation of WA12 and B2 phases in the composite plugged dislocation, thus inducing resistance in particle dislocation and resulting in increased microhardness. Cai et al. [117] and Lu et al. [97, 98] also reported that these in-situ formations of WA12 and B2 phase improved the strength as well as the toughness in the aluminum matrix composite.

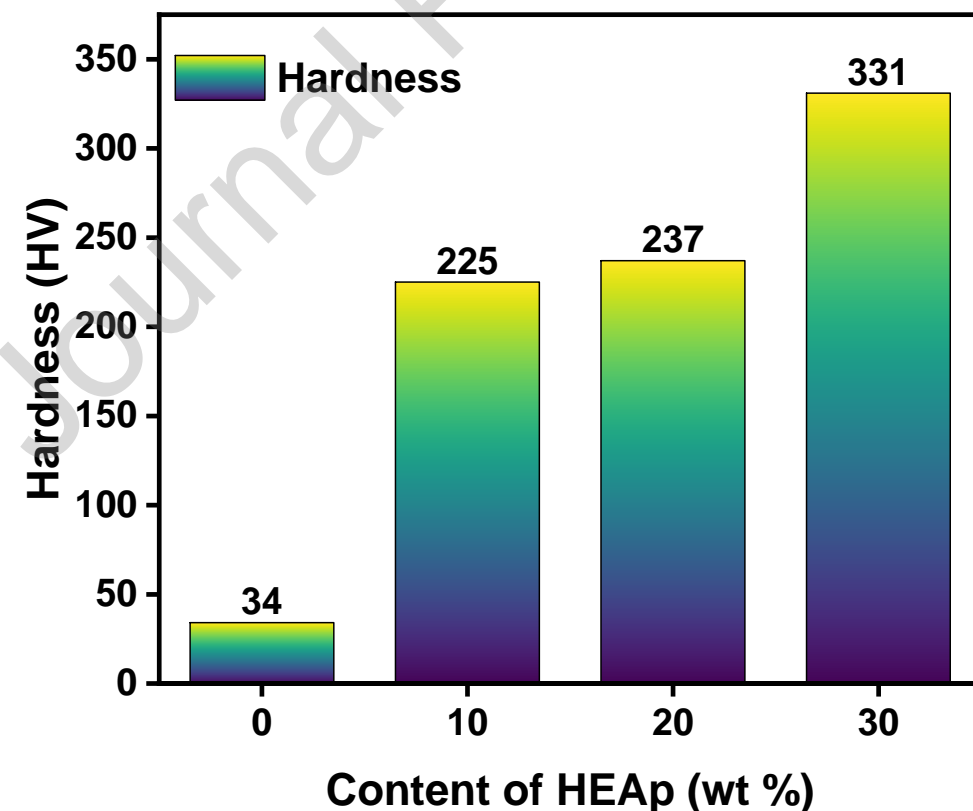


**Fig. 60** Vickers hardness variation w.r.t. content of HEAp (wt.%) in composite [96].

Yuan et al. [95] studied the microhardness behavior of titanium matrix reinforced by HEAp fabricated through vacuum sintering powder metallurgy method at different sintering temperature. **Fig. 61** shows the variation of hardness according to sintering temperature and hardness value is highest (402.6 HV) at 850 °C compared to other sintering temperatures. The diffusion layer formation between matrix and HEA and the reaction of elements of HEA have a positive effect on the hardness of composite materials. The hardness increases with the increase in interface diffusion layer however at 900 °C sintering temperature the hardness decreases due to higher diffusion and dissolution of HEA in matrix.

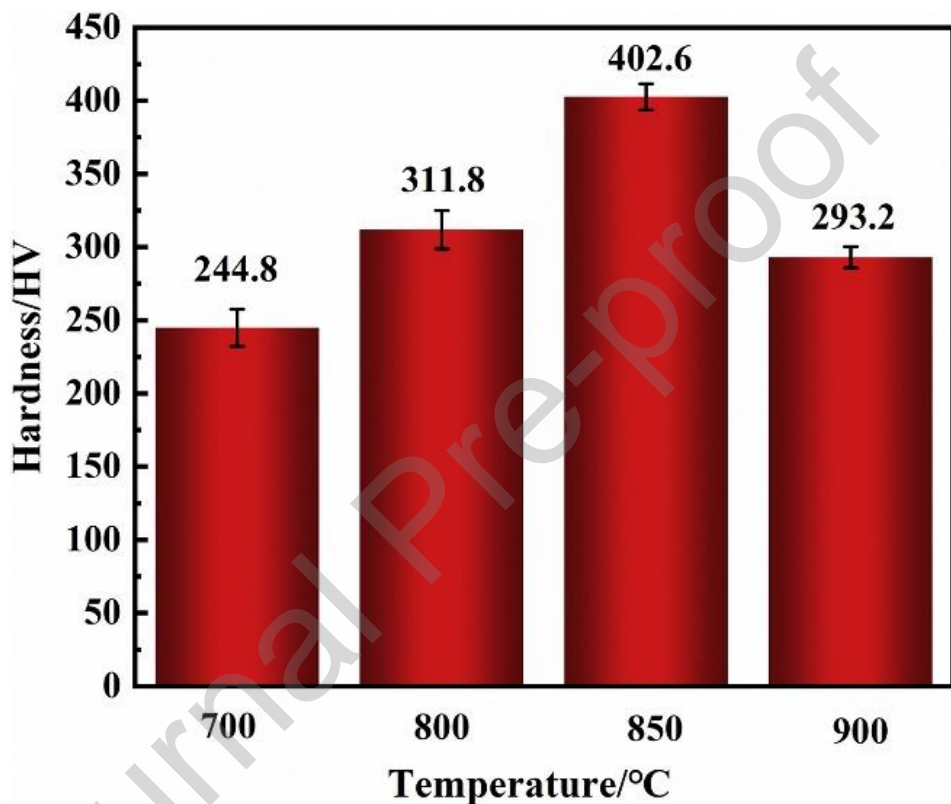


**Fig. 61** Microhardness behavior at experimented sintering temperatures [95].

Tun et al. [104] fabricated Mg metal composites with HEA by microwave sintering and studied the microhardness property of Mg as well as the composites. The hardness of the composite increased by 47%, 51% and 54% for 2.5, 5, and 7.5 wt.% HEA reinforced composite compared to pure Mg, respectively. The hardness improvement for the composite is due to the grain refinement effect in microstructure and hard and strong HEAs addition. It is clear from this study that Mg base HEA reinforced composites show better microhardness compared to other reinforced magnesium composites [120], compared to reinforcements like metallic glass, ceramics and metallic particles in the literature, all this is indicated in **Fig. 62** below.

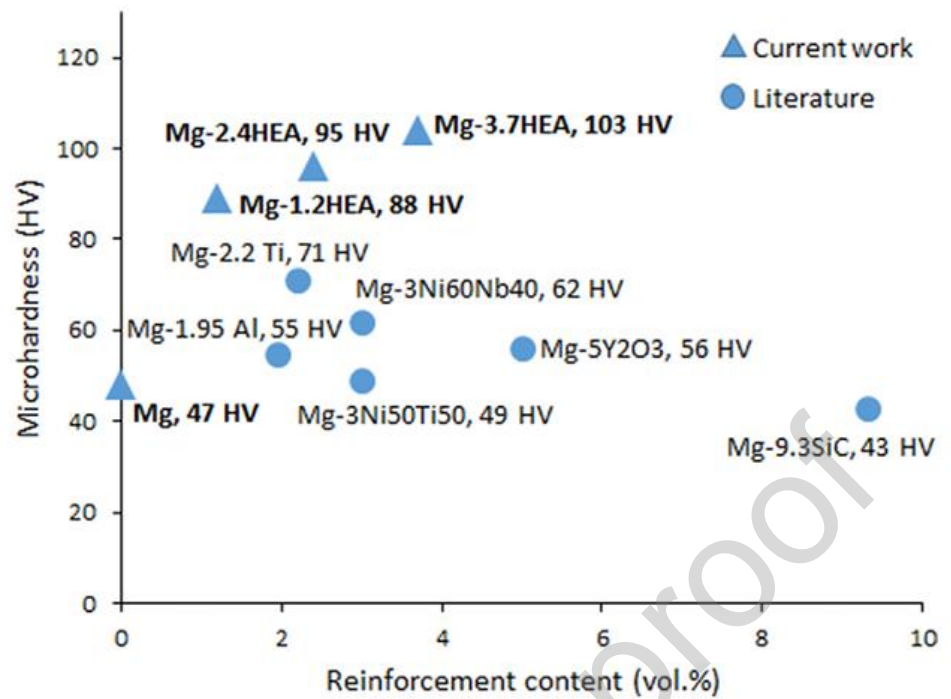


**Fig. 62** Microhardness variation with HEA content through Mg-HEA composites and other literature work [104, 120].

**Table 4** The statistical processing of the experimental results.

S. No.	References	Matrix	Reinforcement	Hardness
1	Ananiadis et al. [33]	Aluminum 1050	MoTaNbVW	46 ± 4 HRB
2	Zhang et al. [51]	Aluminum 2219	AlCoCrFeNi	120.5 HV
3	Zhang et al. [52]	Aluminum 2219	Al <sub>0.5</sub> CoCrFeNi	120.5 HV
4	Yuan et al. [92]	Titanium	CoCrFeNiMo <sub>0.2</sub>	402.6 HV
5	Wang et al. [93]	Aluminum	CuZrAlTiNiW	331 HV
6	Tun et al. [96]	Magnesium	Al <sub>20</sub> Mg <sub>20</sub> Li <sub>20</sub> Cu <sub>20</sub> Zn <sub>20</sub>	110 HV
7	Praveen Kumar et al. [108]	Aluminum 2014	Al-20Cu-10Mg	102 HV
8	Zhu et al.	Aluminum	Al <sub>35</sub> Ti <sub>15</sub> Cu <sub>10</sub> Mn <sub>20</sub> Cr <sub>20</sub>	225 HB

#### 4.2 Towards the strength evaluation:

It can be seen through research studies that the addition of HEA particles to the matrix improves both yield strength (YS) and ultimate tensile strength (UTS) of the composite. The strength of MMCs can be assessed by tensile and compressive testing, where the behavior of UTS and YS provide information on the strength

improvement by adding HEA in the matrix. This section is devoted to the enhancement of strength mechanical properties for various HEA-MMCs.

Chen et al. [31] studied the effect of AlCoNiCrFe high-entropy alloy (10 & 20 wt.%) on Cu matrix by measuring the compressive strength. **Fig. 63** represents the stress-strain behavior of pure Cu and composite in compressive test. Result shows improvement in strength and reduction in ductility by adding 10 and 20 % HEA in composite. The yield strength of 10 % HEA-Cu alloy is 240 MPa, and 20 % HEA-Cu is 330 MPa, which is 160% and 220 % higher than pure Cu matrix. The reason behind the strength improvement is interfacial bonding and increased density with less voids and pores. Different metallic glasses such as Zr<sub>57</sub>Ti<sub>8</sub>Nb<sub>2.5</sub>Cu<sub>13.9</sub>Ni<sub>11.1</sub>Al<sub>7.5</sub> [121] and Ni<sub>70</sub>Nb<sub>30</sub> [122] were also used to improve the strength of Al based MMC, but it is recognized that HEA gives more strength compared to metallic glasses and due to their difference in plasticity. Metallic glasses are highly brittle with good strength so it is hard to deform plasticity due to brittle nature. The HEA and Cu phase feel similar kind of stress during deformation. HEA exhibits high strength along with plasticity, and the strain during deformation is at the plasticity limit of the HEA particle.

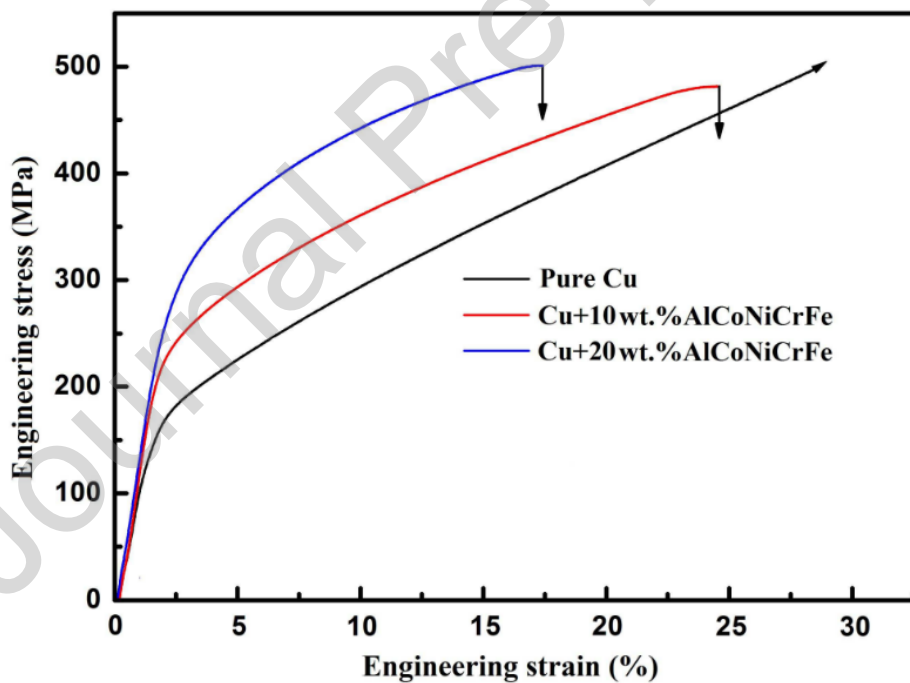


**Fig. 63** Compressive stress-strain curve of base Cu metal and composites [31].

Zhang et al. [54] conducted that the tensile properties are enhanced in MMCs by reinforcing the HEA particles. A UTS value of 125.6 MPa was found at Al matrix and after 1.5 wt.% HEAp 217.4 MPa UTS was found. Further, the addition of HEA particles to the MMC the properties are decreased. A similar trend was observed in the YS of the composite, but the YS became stable with HEA addition from 0.75 to 5 wt.%. However, the fracture elongation (FE) graph of the composite shows a reverse trend (**Fig. 64**) of strength. As the wt.% of HEAp in the composite increases, the fracture strength is reduced from the highest value of

pure Al 2219 alloy at 7.55%, and a sharp reduction from 6.65% to 5.07% is found after HEA addition from 1.5 to 5 wt.%. The author reported seven strengthening mechanisms for improvement in strength of Al alloy such as grain refinement, load transfer, Orowan, elastic modulus mismatch, solute and dislocation strengthening, and mismatch in the coefficient of thermal expansion (CTE). Dimples longer than 6  $\mu\text{m}$  were observed in the alloy having lower UTS and YS compared to HEA containing Al alloy shown in **Fig. 65**. A fishbone structure indicated in the blue rectangular area was observed, indicating eutectic HEAp in the 0.5 wt.% composite. The cleavage fracture and band fracture during testing are indicated by blue and white arrows, respectively. Casting defects such as blow holes, rough surface and cracks were also observed in AMCs more than 1.5 wt.% of HEAp due to HEA/Al interface bonding and agglomeration of reinforcement particles.

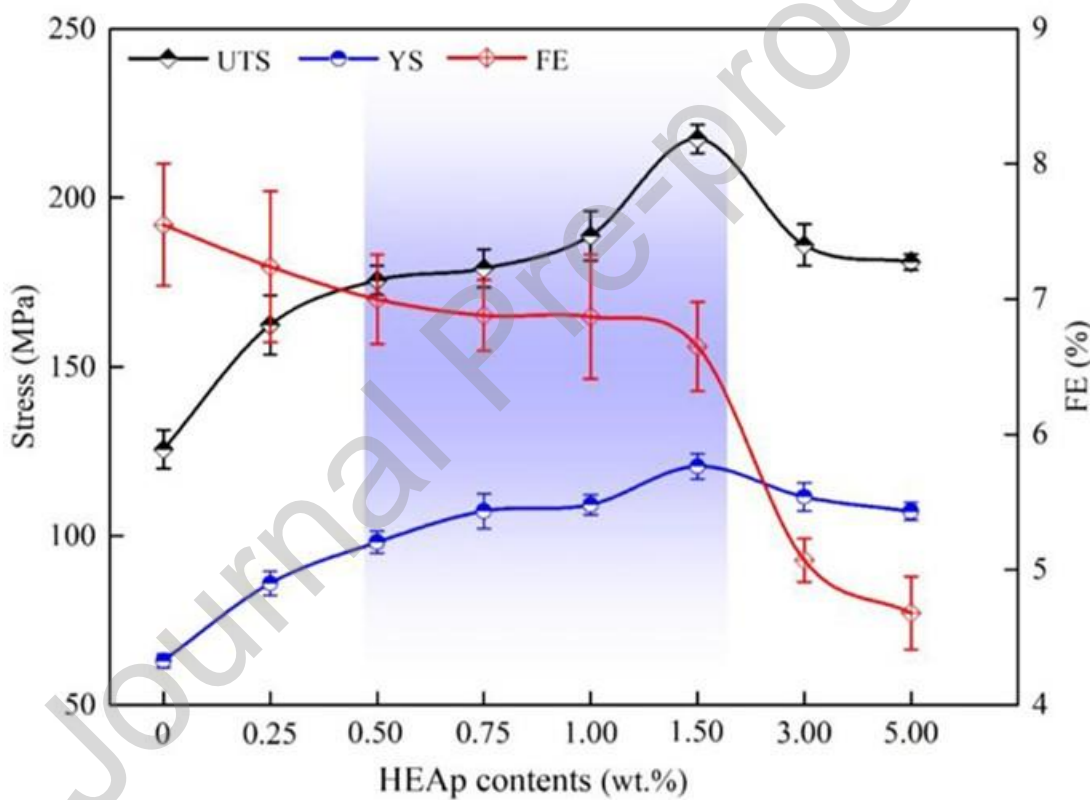


**Fig. 64** Tensile test reading of different HEA-MMC [54].

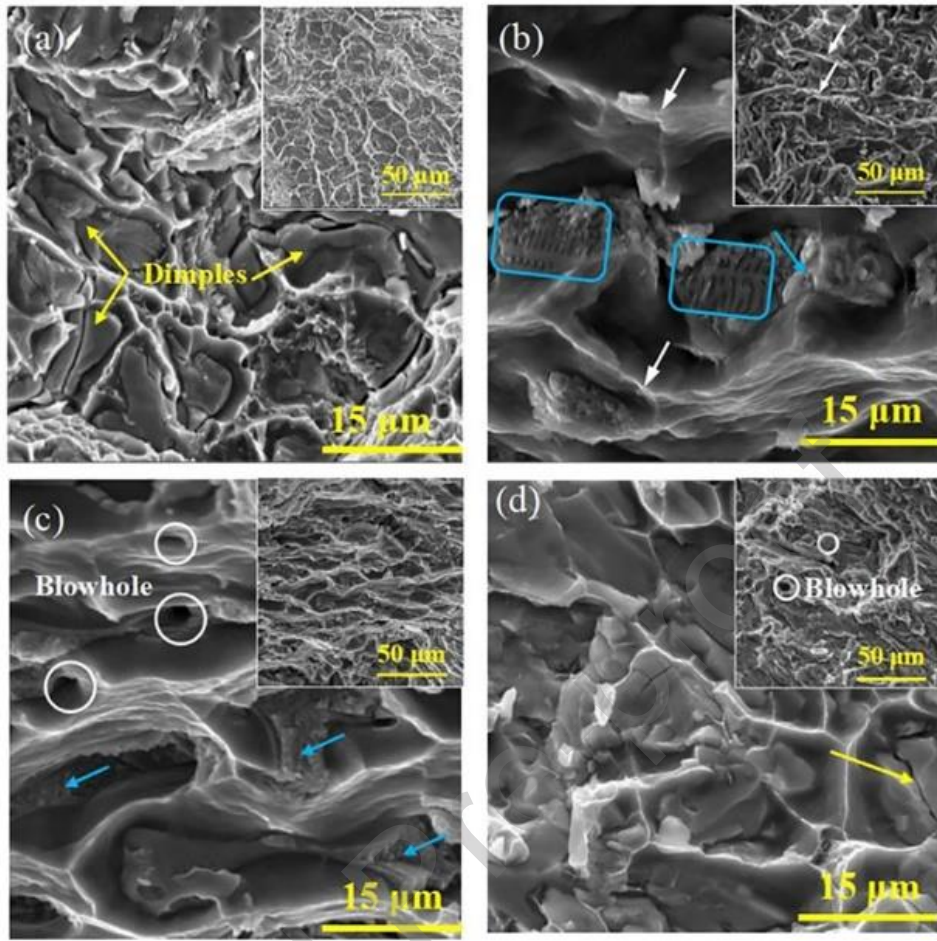


**Fig. 65** Tensile fractography of (a) 0, (b) 0.5, (c) 1.5, (d) 3 wt.% HEA-AMC [54].

Liu et al. [93] fabricated AlCoCrFeNi HEA-Al MMC with 5 vol. % reinforcements by SPS process and sintering done at different temperatures (540°C, 560°C, 580°C and 600°C). A compression test was carried out for strength evaluation and is represented by **Fig. 66**. The YS was found to increase from 540°C to 580°C and no further improvement was found after 600°C sintering temperature. The YS of the composite is observed as 96 MPa, 105 MPa and 137 MPa for sintering temperatures 540°C, 560°C and 580°C, respectively, of the Al-5vol.% AlCoCrFeNi HEA reinforced composites. However, no such change in mechanical properties was detected at 600°C sintering temperature as compare to 580°C sintering temperature. This improvement is due to the presence of a 7.6 μm thick transition layer between the Al matrix and the HEA reinforcement.

Praveen Kumar et al. [116] developed the composites by the stir casting method to study the strength of composites. The HEAp wt.% varies from 5 to 15 in Al matrix and results are shown in **Fig. 67** with stress-strain curve. Increasing the HEA content in the matrix improved its strength compared to the pure composite, with UTS obtaining 70% improvement and YS obtaining 95%. Higher UTS values were found in the composite material due to load transfer effect with increasing reinforcement particles.

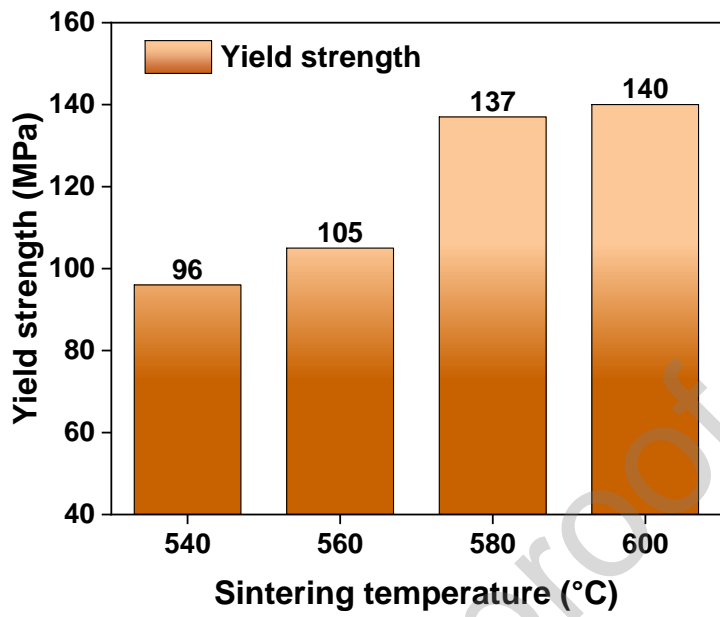


**Fig. 66** Yield Strength (YS) of composite at different sintering temperature [93].

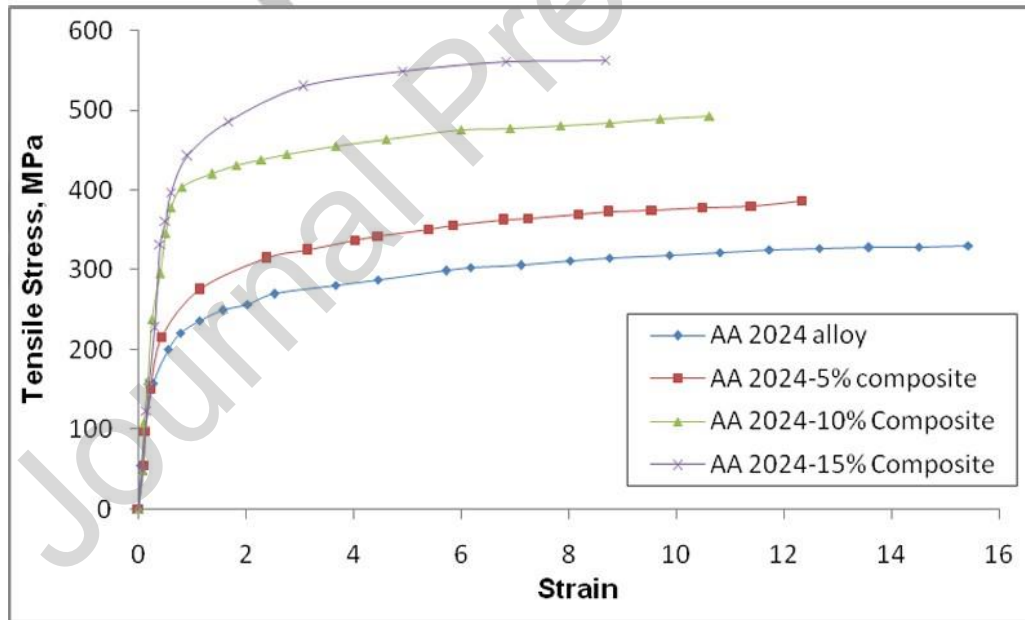


**Fig. 67** Stress-strain curve for alloy and composites [116].

T. Lu et al. [123] studied impact of nano crystalline high entropy alloy (NCHEA) on fine grained 2024Al matrix. The composite is fabricated by four methods such as powder metallurgy after hot pressing, hot extrusion, and heat treatment at wt.% 0, 7.5, 15 and 30 of  $\text{CoNiFeCrAl}_{0.6}\text{Ti}_{0.4}$  reinforcement HEAp. The tensile test was performed to evaluating strength of the composite with sample gauge length 15 mm, diameter 3 mm with strain rate of  $5 \times 10^{-3} \text{ s}^{-1}$ . **Fig. 68** showing stress-strain graph of monolithic as well as composite samples. The yield strength improved as the NCHEA was added to the matrix. The yield strength at 7.5 wt.% NCHEA-2024Al composite is  $419 \pm 12$  MPa, which is 112 MPa higher than matrix Al. Uniform dispersion

of reinforcement particles and fine crystal size are the reasons for grain refinement and strength improvement of the matrix. Finally they compared the results with different ceramic reinforcement and recommended NC-HEAp as reinforcement for Al matrix for aerospace applications.

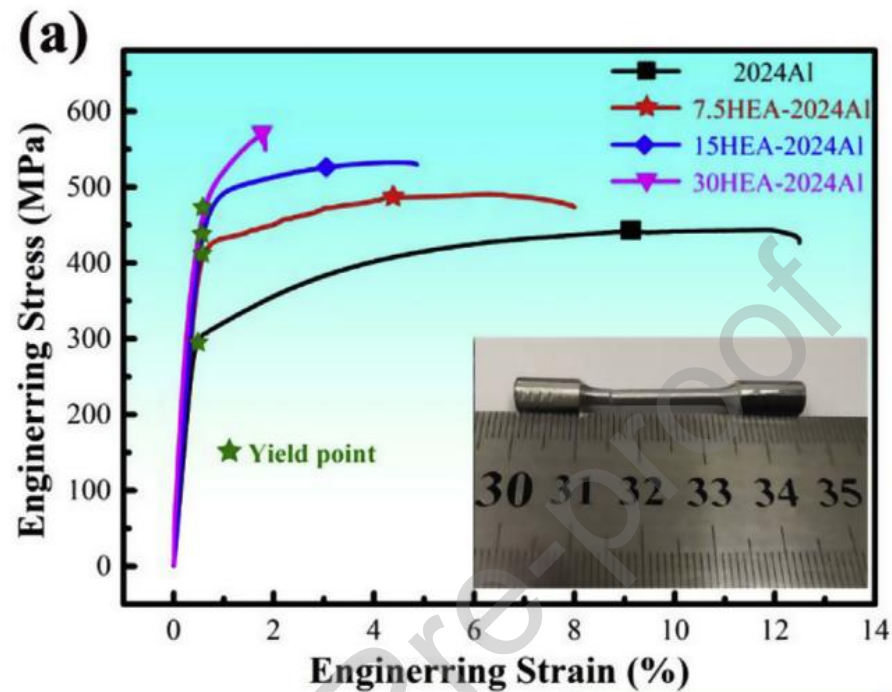


**Fig. 68** Engineering stress-strain curve for monolithic and composites [123].

Chen et al. [124] fabricated an AA 6061 based composite reinforced with  $\text{CoNiFeAl}_{0.4}\text{Ti}_{0.6}\text{Cr}_{0.5}$  HEA alloys (7.5 vol.%) with particle size below  $23\ \mu\text{m}$  by powder metallurgy (PM) route. The effect of ball milling time (10, 20 and 40h) on mechanical properties and microstructure was evaluated. The tensile strength of the composite is enhanced with addition of the HEA reinforcement as shown in stress-strain diagram (**Fig. 69**). The tensile strength of the 10h ball milled composite specimen was 378 MPa, which was higher than the strength of the base composites of 238.5 MPa. The highest ultimate tensile strength (UTS) of 385 MPa and yield strength (YS) of 348 MPa were found at 40 h milling. Hall-Pech effect and geometrically required dislocations are identified as the main strengthening mechanisms in fabricated composites. Even distribution of HEA in the matrix at 40h milling time and absence of oxide layer formation on the reinforcement particles are the root cause of the strength improvement.

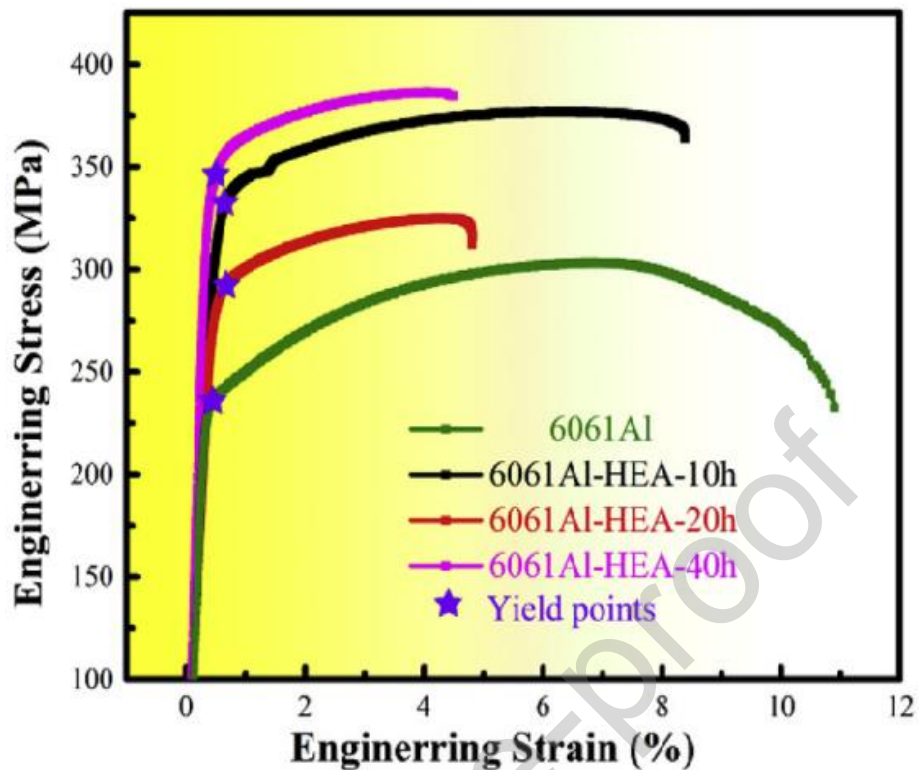


**Fig. 69** Engineering stress-strain curve for Al 6061 and composite [124].

Huang et al. [108] fabricated an aluminum-based composite by reinforcing AlCrTiV HEA particles into a molten aluminum alloy matrix and dispersing it through an ultrasonic probe. The effect of HEA particles on matrix aluminum was evaluated by mechanical and microstructural analysis. The stress-strain curve of composite and monolithic Al is shown in Fig. 70, and the results are depicted in Table 5. It was observed that the UTS, YS, and elastic modulus properties were improved and the elongation decreased with the incorporation of HEA particles into the matrix. Addition of 3 wt.% HEA increased the matrix UTS by 54% and YS by 38% compared to the matrix and 6wt.% HEA-AMC increased UTS by 81% and YS by 63%. The ductility of the alloy decreases with the addition of HEA particles to the matrix from 3wt.% to 6wt.% due to the presence of coarse  $\text{Al}_{45}(\text{Cr}, \text{V})_7$  particles (Fig.71). HEA particles, evenly distributed in the composites, increase the hardness with the growth of reinforcing particles.

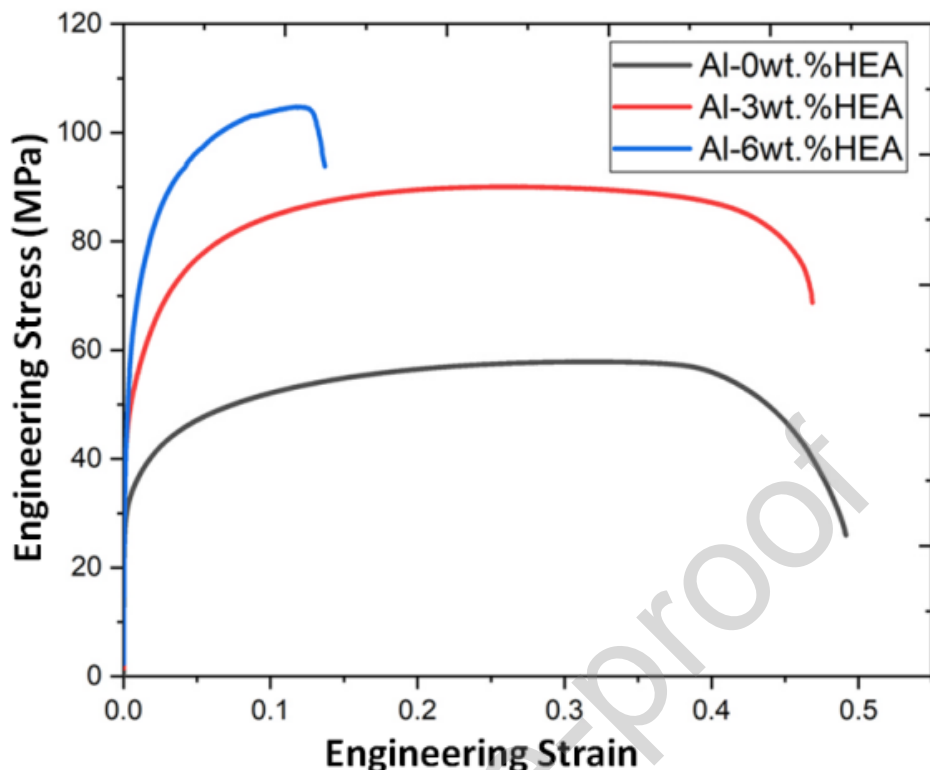


Fig. 70 Engineering stress-strain curve for pure as well as composites [125].

Table 5 Mechanical properties of pure Al and Al-HEA composites.

Material	Yield strength (MPa)	UTS (MPa)	Elongation (%)	Elastic Modulus (GPa)
Al	30.6	57.8	49.1	66.6
Al-3wt.% HEA	42.3	89.2	46.8	70.4
Al-6wt.% HEA	49.8	104.7	18.7	73.7

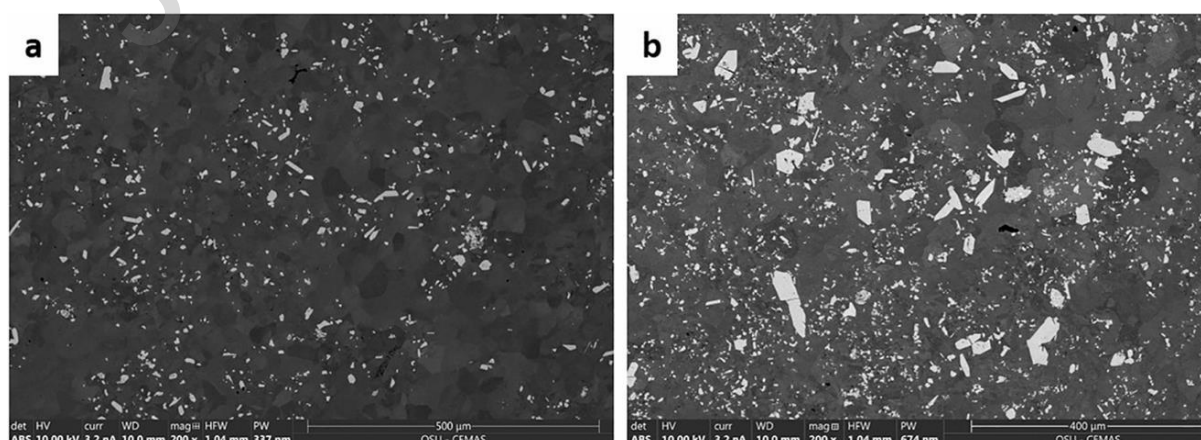
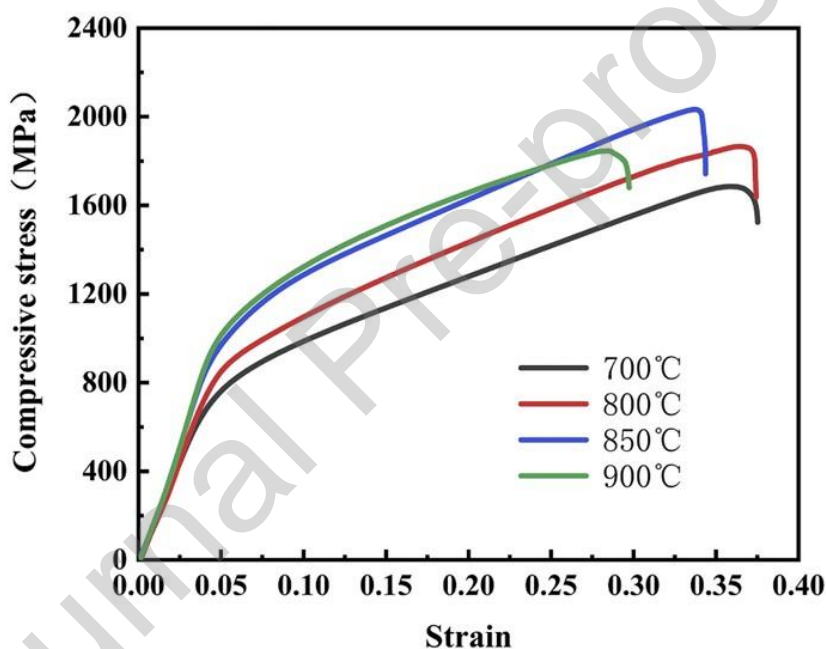


Fig. 71 Backscattered electron image of Al with (a) 3 wt.% HEA particle addition, (b) 6 wt.% addition [125]

Yuan et al. [95] determine the compressive strength of titanium HEA-reinforced composite prepared by powder metallurgy method. **Fig. 72** shows the stress-strain behavior of the composite generated by compression test at different temperatures from 700-900 °C. The yield strength and compressive strength first increases and then decrease after 850 °C sintering temperature. A maximum yield strength of 928.2 MPa and a compressive strength of 2032.6 MPa at 850 °C were found this is due to formation of a thick interdiffusion layer between HEA and matrix. The interdiffusion layer increases the bonding quality of the composite from weak mechanical bonding to strong diffusion bonding and thus increases the overall strength of the composite. Porosity decreases and density increases with increase in sintering temperature, which helps in improving the strength properties of the composites. At 900 °C the dispersion of HEA in the matrix is very high, which reduces the improvement of impact and thus the strength.



**Fig. 72** Stress-strain curve of compression test of composites at different sintering temperatures [95].

Tun et al. [104] studied both tensile and compressive strengths in Mg-HEA MMC and found an improvement in both compared to the unreinforced matrix, results shown in **Table 6**. **Fig. 73** shows the behavior of the composite and matrix to illustrate the stress-strain relationship. The load transfer strengthening for micron-sized HEA, Orowan strengthening for submicron-sized HEA and particle-stimulated nucleation (PSN) mechanisms for greater than 1 $\mu$ m grain-sized HEA, acted behind the improved tensile strength. The composite tensile UTS value increased with increasing HEA content and the highest value of 220 MPa (Table 4) was found for 7.5 wt.% HEA-MMC. As seen in SEM images of composite in **Fig. 74** the HEAs are uniformly dispersed but due to formation of cluster of HEAs it nullifies the strengthening effect of Orowan and this results in constant tensile YS for composites. However, the interfacial bonding between the reinforcement and the Mg matrix, due to the metallic nature of the HEA, it leads to improved strength and hardness. Both YS and UTS increase simultaneously in compression due to increased ductility. There was a

drastic improvement from 2.5% HEA to 5% HEA, but near equal strength found from 5% HEA to 7.5% HEA. In compressive strength, the particles cluster in the microstructure (**Fig. 74**) does not cause discontinuities, and Hall-Pech, Orowan and load transfer equally play a role in increasing the YS and UTS of the composite.

An increase in strength has been observed in composite materials as a result of several strengthening mechanisms such as particle-induced nucleation, Orowan strengthening and load transfer strengthening. Furthermore, the mechanical properties of composite material are highly influenced by the distribution of high entropy alloy (HEA) particles. Strengthening procedures to increase strength are discussed below-

**Load Transfer Strengthening:** When external loads are effectively transferred between the matrix and reinforcement phases in a composite material, load transfer strengthening occurs. The reinforcement phase of a composite such as HEA particles contains a significant amount of the applied load. A strong bond between the reinforcement and the matrix allows efficient load transfer, which improves the mechanical properties of the reinforcement, including strength and stiffness. To prevent debonding and promote effective stress transfer, load transfer strengthening depends on a strong interface between the reinforcement and the matrix. **Orowan Strengthening:** This is a strengthening mechanism when the dispersed particles in the matrix resist dislocation motion. Particles obstruct the movement of dislocations, requiring additional stress to overcome the obstruction. This barrier's increased resistance to plastic deformation results in improved strength and toughness of the material. The size, shape and volume percentage of the reinforcement particles are among the variables that affect how effectively Orowan affects strength. Stronger effects are generally produced by smaller particles and higher volume fractions. **Particle-stimulated nucleation Strengthening:** The process of nucleating and growing new phases or microstructural features at the interface between matrix and reinforcement particles is called particle-stimulated nucleation. This process can cause the material to become stronger by forming intermetallic compounds, grain refining, or precipitation of secondary phases. The mechanical properties of the composite material can be improved by the presence of HEA particles, which serve as nucleation sites for the formation of new phases during processing or subsequent heat treatments. The mechanical properties of the composite material are significantly affected by the dispersion of HEA particles in it. Particles should be evenly distributed throughout the matrix to maximize the effectiveness of strengthening mechanisms such as particle-stimulated nucleation and Orowan strengthening. Furthermore, homogeneous distribution reduces stress concentrations and protects against premature failure caused by localized deformation. On the other hand, uneven distribution of particles may lead to areas of poor bonding or concentrated stress, which reduce mechanical properties and increase the risk of failure modes such as delamination or cracking. As a result, various strengthening mechanisms, such as particle-induced nucleation, Orowan strengthening, and load transfer strengthening, account for the strength seen in composite materials, including HEA-aluminum matrix composites. Optimizing these strengthening mechanisms and ultimately influencing the overall mechanical properties of the composite depends on the distribution of HEA particles in the material.

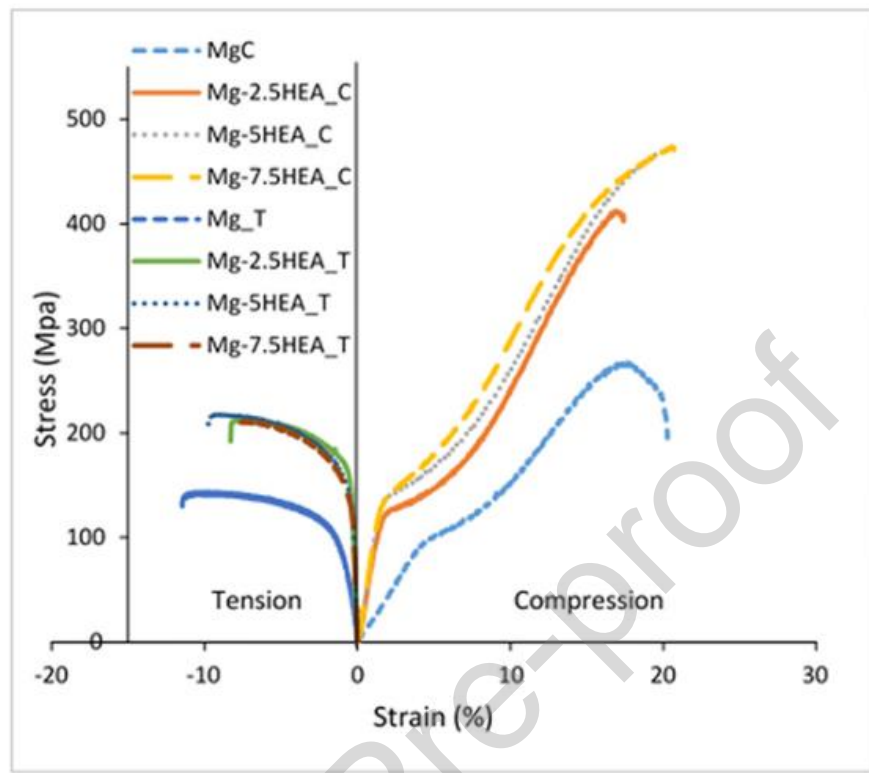


**Fig. 73** Tensile and compression behavior of Mg-HEA composites and Mg [104].

**Table 6** Tensile and compressive strength results of Mg and composites.

Material	Tension		Compression	
	0.2 Yield Strength (MPa)	Ultimate Strength (MPa)	0.2 Yield Strength (MPa)	Ultimate Strength (MPa)
Mg	103 ± 9	162 ± 15	91 ± 8	263 ± 16
Mg-2.5HEA	154 ± 14	199 ± 12	125 ± 3	412 ± 2
Mg-5HEA	147 ± 7	216 ± 9	135 ± 4	468 ± 7
Mg-7.5HEA	147 ± 17	220 ± 19	141 ± 4	471 ± 7

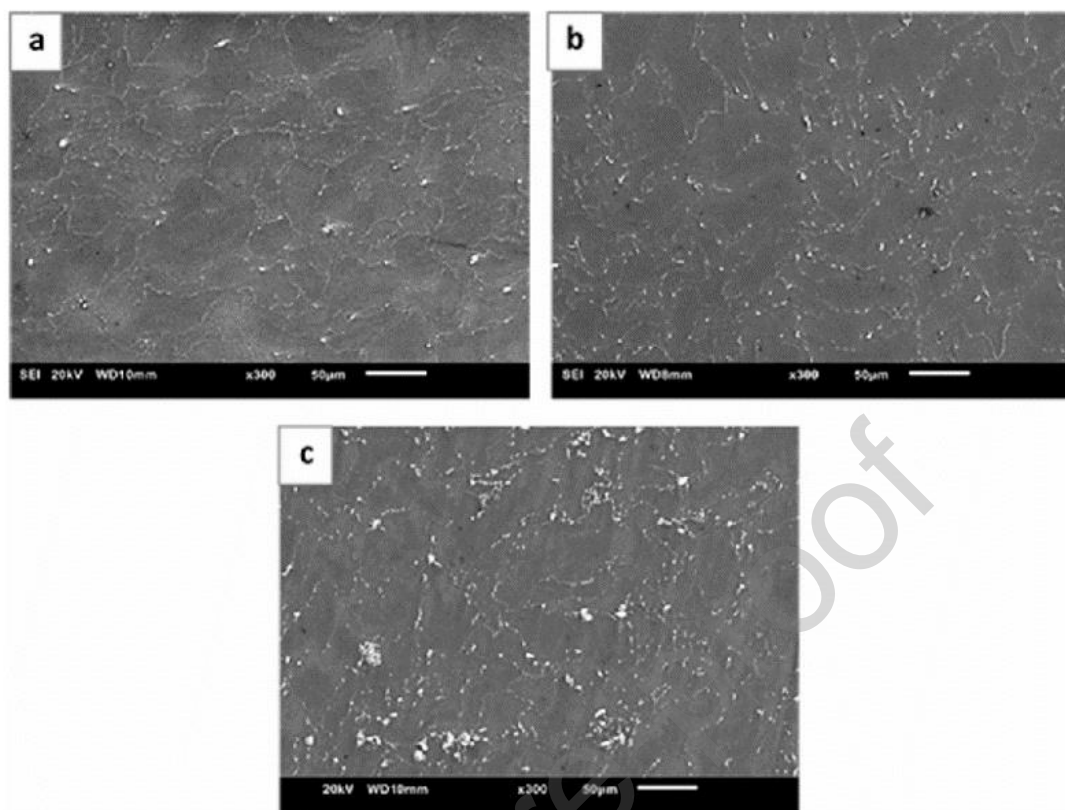


**Fig. 74** SEM micrographs of Mg-HEA composite with HEA as (a) 2.5, (b) 5 and (c) 7.5 wt.% [104].

**Table 7** The statistical processing of the experimental results (Strength).

S. No.	References	Matrix	Reinforcement	compressive strength (MPa)	Tensile (MPa)	strength	
				YS	UTS	YS	UTS
1	Chen et al. [31]	Copper	AlCoNiCrFe	330			
2	Zhang et al. [54]	Aluminum 2219	AlCoCrFeNi			217.4	
3	Liu et al. [93]	Aluminum	AlCoCrFeNi	140			
4	Yuan et al. [95]	titanium	CoCrFeNiMo <sub>0.2</sub>	928.2	2032.6		
5	Tun et al. [104]	Magnesium	Al <sub>20</sub> Mg <sub>20</sub> Li <sub>20</sub> Cu <sub>20</sub> Zn <sub>20</sub>	141 ± 4	471 ± 7	147 ± 17	220 ± 19

6	T. Lu et al. [123]	Aluminum 2024	CoNiFeCrAl <sub>0.6</sub> Ti <sub>0.4</sub>	419 ± 12		
7	Chen et al. [124]	Aluminum 6061	CoNiFeAl <sub>0.4</sub> Ti <sub>0.6</sub> Cr <sub>0.5</sub>	348	385	
8	Huang et al. [108]	Aluminum	AlCrTiV	49.8	104.7	
9	Zhu et al. [97]	Aluminum	Al <sub>35</sub> Ti <sub>15</sub> Cu <sub>10</sub> Mn <sub>20</sub> Cr <sub>20</sub>	566	641	

#### 4.3 Effect of HEA reinforcement on corrosion behavior:

HEA as a reinforcing agent has good corrosion resistance [126]. It has been found in technical research articles that it increases the corrosion resistance of HEA-MMCs in the matrix composite. Corrosion resistance was evaluated by potentiodynamic polarization testing in 3.5% NaCl solution with pH 7 value. This section analyzes the effect of HEA on the matrix material in a corrosive environment.

Ananiadis et al. [33] studied the corrosion performance of AMC reinforced by HEA particles prepared by powder metallurgy process. Different HEA volume percentages of Al 1050-based alloy (0, 1, 3, and 5 vol.%) were fabricated and 3.5% NaCl solution was used for corrosion test. In **Fig. 75** the aluminum phase polarization curves from 0 to 3 vol.% HEA content show the same trend as pure aluminum. However, the Al-5 vol.% HEA composite exhibits a different trend of polarization curve which reflects less corrosion due to the presence of HEA content in composite. The curve reflects the polarized behavior of monolithic aluminum and alloys, in all cases the pitting potential (Epit) appears at a higher value when compared to the corrosion potential (Ecorr). Ecorr values for Al and low HEA-Al alloys are lower at lower value of current density, but increased current density with 5 wt.% indicates higher value of Ecorr for the alloy.

After potentiodynamic polarization corrosion test SEM images of aluminum matrix and composites were examined (**Fig. 76**). Surface degradation is visible from **Fig. 76 (b-d)** due to the pitting action of NaCl. Major corrosion is seen in the aluminum matrix and the HEA reinforcement is unaffected. The 5 wt.% HEA-Al composite elemental mapping is shown in **Fig 76 (e)**. The elemental mapping of corrode 5 wt.% HEA-Al composite sample shows the presence of oxygen at HEAp areas which are near to matrix alloy. The corrosion resistance of HEAp is due to the corrosion mechanism of MoTaNbVW, in which uniform corrosion and electrochemical potential difference between dendrite rich Mo, Ta, W and inter-dendrite rich Nb, V play a major role. Pitting corrosion resistance is also reduced by the Mo, Nb, W component of HEAp. The composite shows improved corrosion resistance by increasing the HEA wt.% in the aluminum matrix, which forms an oxide layer on the composite material [96]. **Fig. 76 (c & d)**, as the HEA content improves it starts to suspend Al and the oxide file on the HEA/Al interface and acts as a corrosion site. The uniform

distribution of HEA particles in the composite and interface structure in HEA/Al are important factors for the increase in corrosion resistance. A stablished layer of Mo, W and Nb in the transition between HEA/Al may reduce corrosion. The galvanic effect becomes more effective by increasing the HEAp content and acts between a high amount of HEA and a low amount of HEA i.e. Al. On the other hand it also causes displacement of Al from the HEA/Al interface. This galvanic effect is reduced by the uniform dispersion of HEAp over the alloy and no other intermetallic compound is formed. The strength and reduced porosity by increasing density are other factors to improve the corrosion performance of the overall composite [96]. The corrosion resistance of MoTaNbVW HEA-Al alloy in seawater solution makes it a potential engineering material for marine applications.

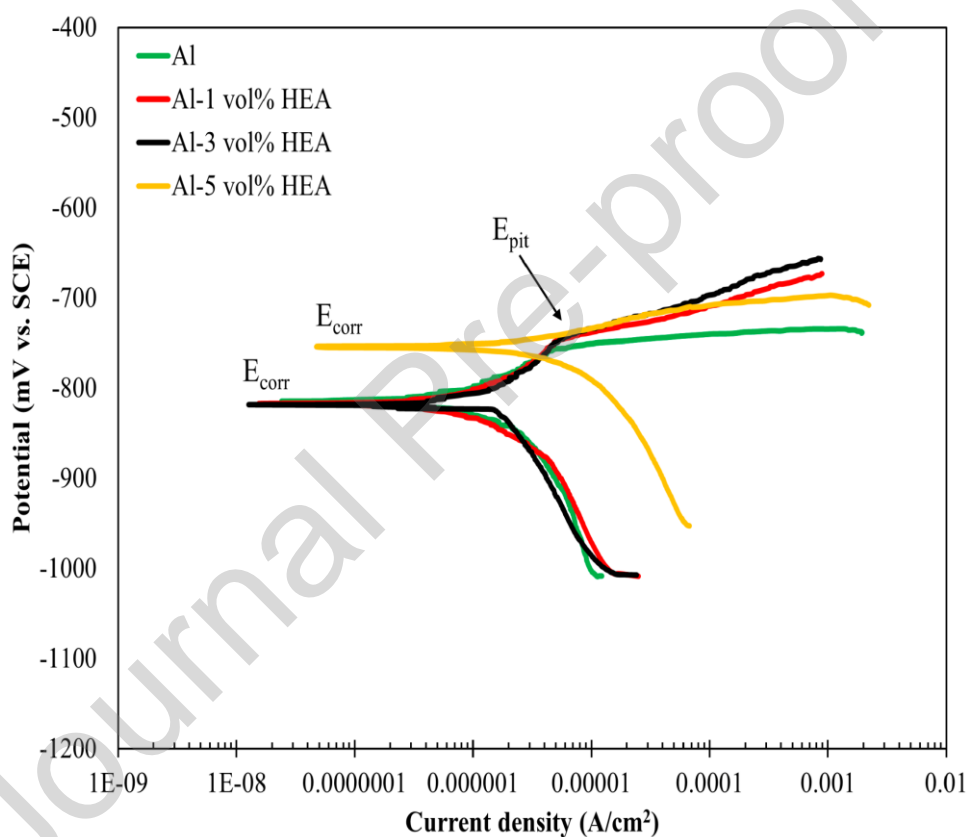


**Fig. 75** Potentiodynamic polarisation curves for HEA-MMC and monolithic aluminum phase. [33]

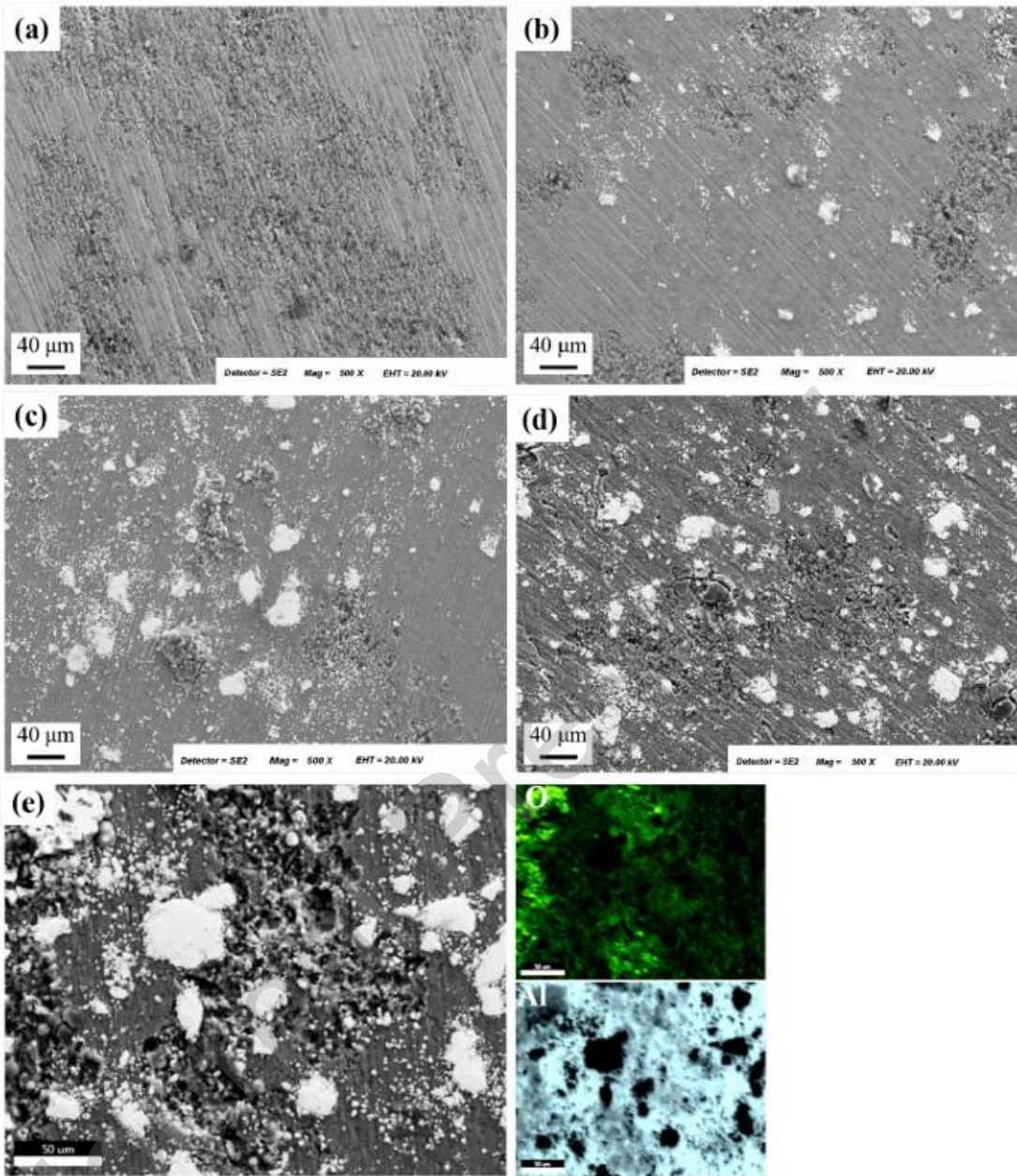


**Fig. 76** SEM image of (a) Al (b) 1 vol.% HEA-MMC (c) 3 vol.% HEA-MMC and (d & e) 5 vol.% HEA-MMC with elemental EDS after corrosion treatment in 3.5% NaCl solution [33].

Wang et al. [96] fabricated the HEA-Al-MMC by spark plasma sintering (SPS) in which HEA is prepared by mechanical alloying. Corrosion properties of CuZrNiAlTiW HEA reinforced aluminum matrix composites at different volume fractions of HEAs (10, 20 and 30 vo.% and named as A110, A120, and A130) were evaluated. The seawater was prepared with salt to distilled water mass ratio 1:30 for preparing electrochemical workstation. The working electrode, reference electrode and counter electrode were tested samples, an Ag-AgCl electrode and a platinum sheet, respectively. After corrosion test the potentiodynamic polarization curve formed and shown in **Fig. 77**. The **Table 5** describe the values found from potentiodynamic polarization curve of corrosion potential ( $E_{corr}$ ), pitting potential ( $E_{pit}$ ), passive region ( $\Delta E = E_{pit} - E_{corr}$ ), current density ( $i_{corr}$ ), and general corrosion rates ( $r_{corr}$ ). Al-10 vol.% HEA composite exhibits

improved corrosion resistance, it is clear from **Table 8** that  $i_{corr}$  and  $r_{corr}$  have lowest value for Al10 and  $E_{corr}$  value is -1.04 V. All composites show good pitting resistance compared to the aluminum matrix, but 30 vol.% HEA MMC has the highest value of  $\Delta E$  and therefore exhibits pitting resistance in seawater.

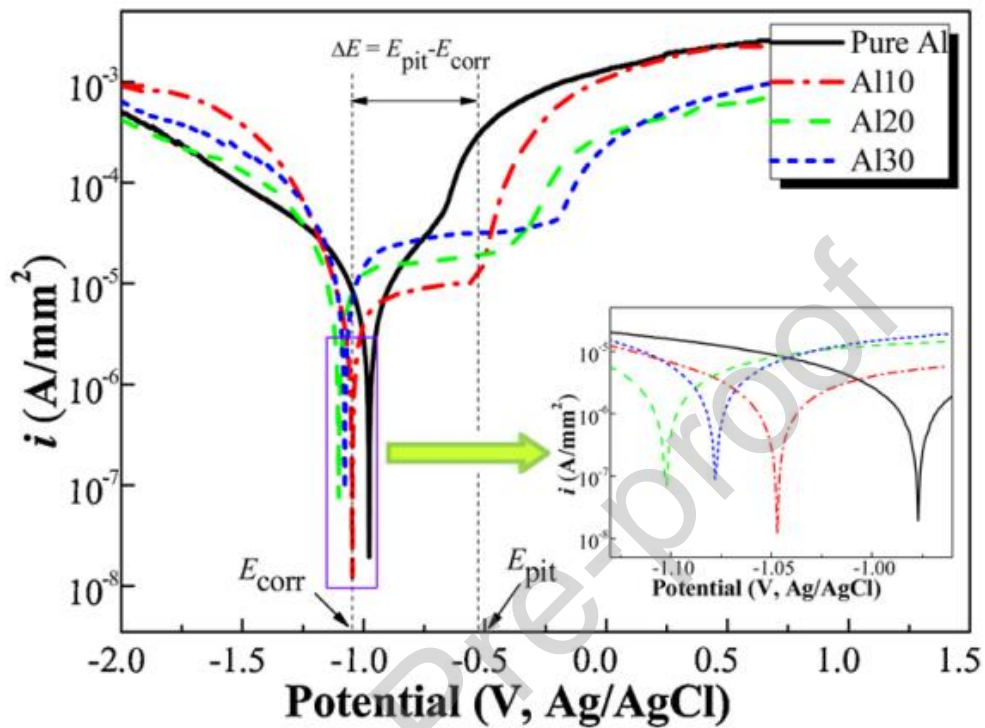


**Fig. 77 Potentiodynamic polarization curve for HEA-MMC with 10, 20 and 30 vol % of HEA [96].**

**Table 8** Values of corrosion resistance test parameters based on potentiodynamic polarization curve shown in **Fig. 73** [96].

Samples	$E_{corr}$ (V vs. $A_g/A_gCl$ )	$E_{pit}$ (V vs. $A_g/A_gCl$ )	$\Delta E$ (V vs. $A_g/A_gCl$ )	$i_{corr} \times 10^{-5}$ (A/mm <sup>2</sup> )	$r_{corr}$ (mm/yr)
Pure Al	$-0.98 \pm 0.02$	-N/A	-N/A	1.28	1.394
Al10	$-1.04 \pm 0.03$	$-0.54 \pm 0.03$	$0.50 \pm 0.05$	0.86	0.827
Al20	$-1.09 \pm 0.04$	$-0.40 \pm 0.06$	$0.69 \pm 0.06$	1.63	1.288
Al30	$-1.07 \pm 0.03$	$-0.18 \pm 0.05$	$0.89 \pm 0.05$	2.44	1.616

Pandian et al. [127] performed corrosion analysis of AMC-HEAp-MMC by Tafel polarization technique. First the open circuit potential (OCP) was generated at steady state, then the potential was applied and the active, passive, and trans-passive regions were developed. The results show that an oxide layer is formed on the Al MMC after an applied potential. Furthermore, an increase in the applied potential starts to break the layer on the workpiece surface and is indicated as the trans-passive region in **Fig. 78**. This substrate breaks

down the compound by chloride ions present in a 3.5% NaCl solution. The uniform distribution of solid particles on the matrix exhibited high corrosion resistance from the attack of chloride ions. The author suggested that the low current and high potential exhibit high corrosion resistance in the workpiece material and the high corrosion resistance provided by the composite low pitting action.

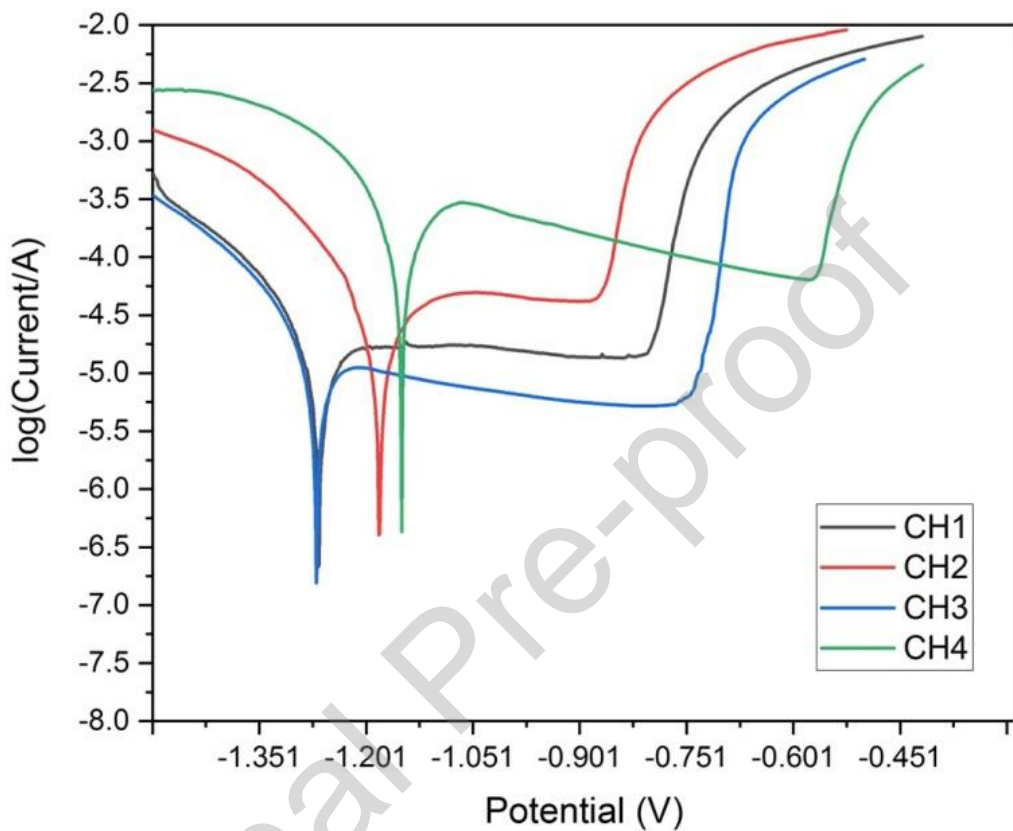


**Fig. 78** Aluminum monolithic and composite Polarization curves [127].

#### 4.4 Effect of HEA reinforcement on wear behavior

Studies are available for the analysis of wear characteristics of special HEAs such as CoCrFeNi HEA [128]. Researchers are trying to evaluate the wear performance of HEA-MMCs, but still very few studies have been conducted. This section focuses on the wear performance of HEA-MMC through wear morphology.

Pandian et al. [127] studied mechanical properties of AA7075-CrCuFeMnNi-MMC fabricated by stir casting method for airframe structural members of aerospace. Composite with different wt.% of reinforcement discussed in wear study. The wear mechanism is described by worn surface morphology (**Fig. 79**) and coefficient of friction (COF). Composite pins with varying loads are used for dry sliding wear tests. Dry sliding wear loss increases as the applied load increases from 10 to 40 N. Smearing mechanisms control the maximum wear resistance at specific loading conditions of composites with 5, 10 and 15 wt.% reinforcement on the matrix. Coefficient of friction decreases with increase in wt.% reinforcement due to formation of oxide layer. The worn surface morphology of aluminum alloys (**Fig. 79 (a)**) shows deep grooves and the alloys show plastic deformation and parallel grooves in the direction of pin sliding. The soft

phases Cu-Ni-Mn of reinforcement under minimum loading condition acts as a lubricant and behave as a barrier for wear; it generates minimum frictional heat between sliding plate and pin with minimum COF. The wear at high loading conditions is borne by hard particles Fe-Cr of reinforcements. The Fe phase oxidized at 15 wt.% reinforcement HEAp Pin-plate interface. The oxidation and lubrication phenomena reduce the COF and bring medium wear damage at sliding.

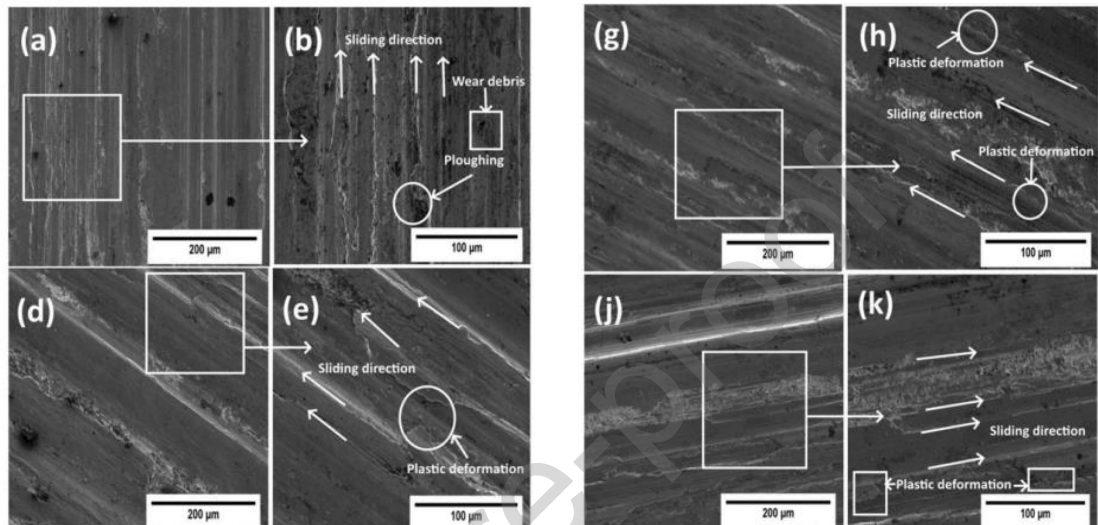


**Fig. 79** Worn surface morphology of (a,b) AA-7075 and composites with (d,e) 5 wt% (g,h) 10 wt% (j,k) [127]

Zhang et al. [55] studied the tribological performance of Al-HEA-MMC fabricated by ultrasonic stir casting to perform a dry sliding wear test. The author is the first of its kind study in dressing with HEA-MMC fabricated using liquid state technique. The effect of heap addition on load and sliding speed on wear rate and COF was evaluated. Weight loss was measured by weighing the sample in an electronic weighing machine before and after completion of the test. The results found that the cost of wear decreases with the increase in reinforcement wear volume. The wear mechanism is described as follows.

#### (a) HEAp addition impact on wear morphology

In **Fig. 80** the effect of reinforcement on the wear morphology of the composite is illustrated. The wear track width reduces with an increase in wt.% of HEAp in the composite. Abrasive wear is indicated by microstructure in which grain is thrown out, debris falls, deep grooves and plugging action occurs. The ploughing action indicates plastic deformation in abrasive wear whereas deep crater-like grooves represent serious HEAp addition and fall off from the composite surface.

#### (b) Applied load impact on wear morphology

**Fig. 81** depicts the SEM image of 3 wt% aluminum alloy with different load conditions, the width of the wear track increases with load increase from 10 to 50 N. **Fig. 81 (a2-d2)** reflecting that the groove depth

increased with increasing reinforcement. Pits and debris are shown in SEM and stresses across the wear surface induced by heat generated during sliding contact surface. At an applied load of 50 N there are deep grooves and cracks due to stress concentration around the HEA/Al interface, and severe wear is compounded with increasing load.

*(c) Sliding velocity impact on wear morphology*

**Fig. 82** depicted SEM images of the wear morphology of 3 wt.% HEA-MMC under constant 30 N load with increasing sliding velocities. The wear track width increases from 2.63 mm to 3.09 mm with sliding speed from 15 mm/s to 60 mm/s. A small amount of debris with a smooth surface at speeds as low as 15 mm/s. Abrasive wear features include deep grooves, increased debris count, uneven surface and severe wear due to increased speed.

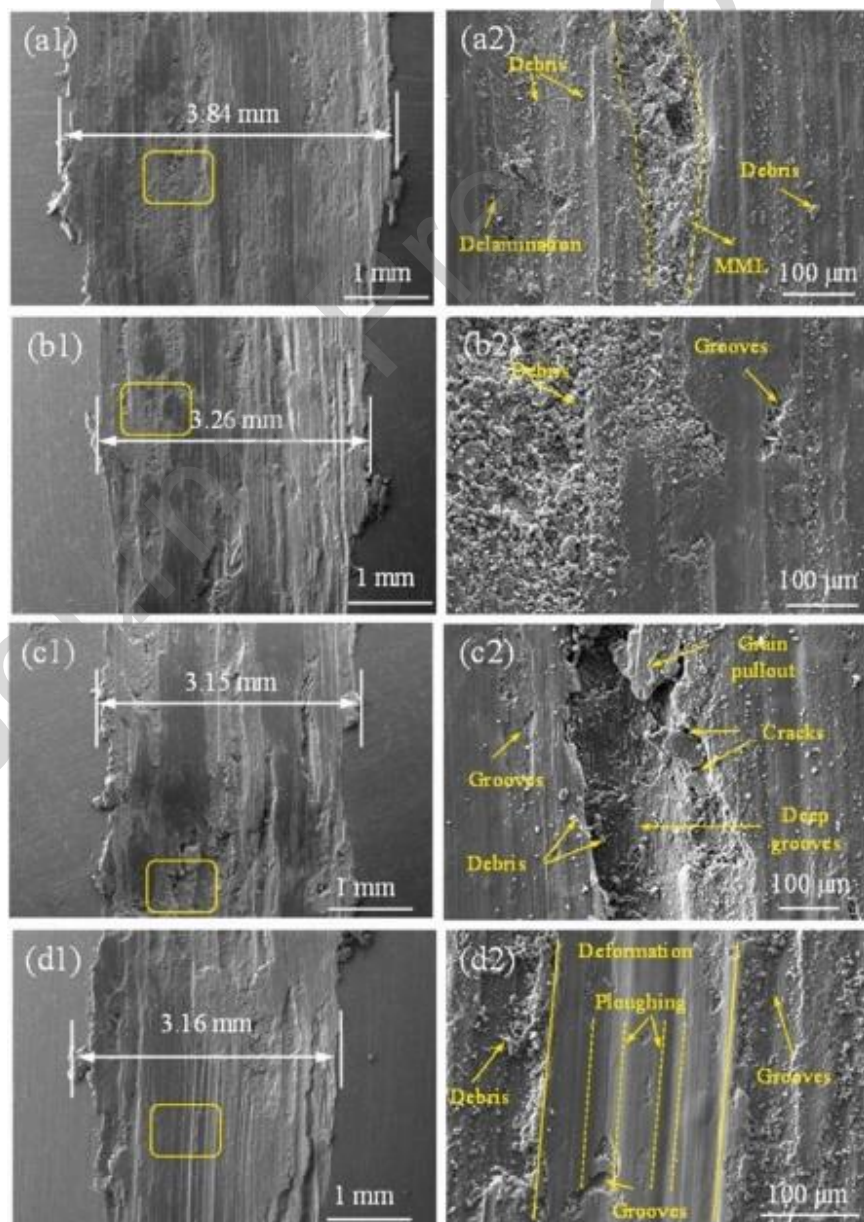


**Fig. 80** Wear track images of HEA-MMC at a constant load of 30 N and fixed velocity of 70 mm/s. (a1-d1) represents AA 2219, 1.5 wt.%, 3.0 wt.%, 5.0 wt.% HEA-MMC. (a2-d2) are the explored view of the yellow rectangular area from a1-d1 [55].

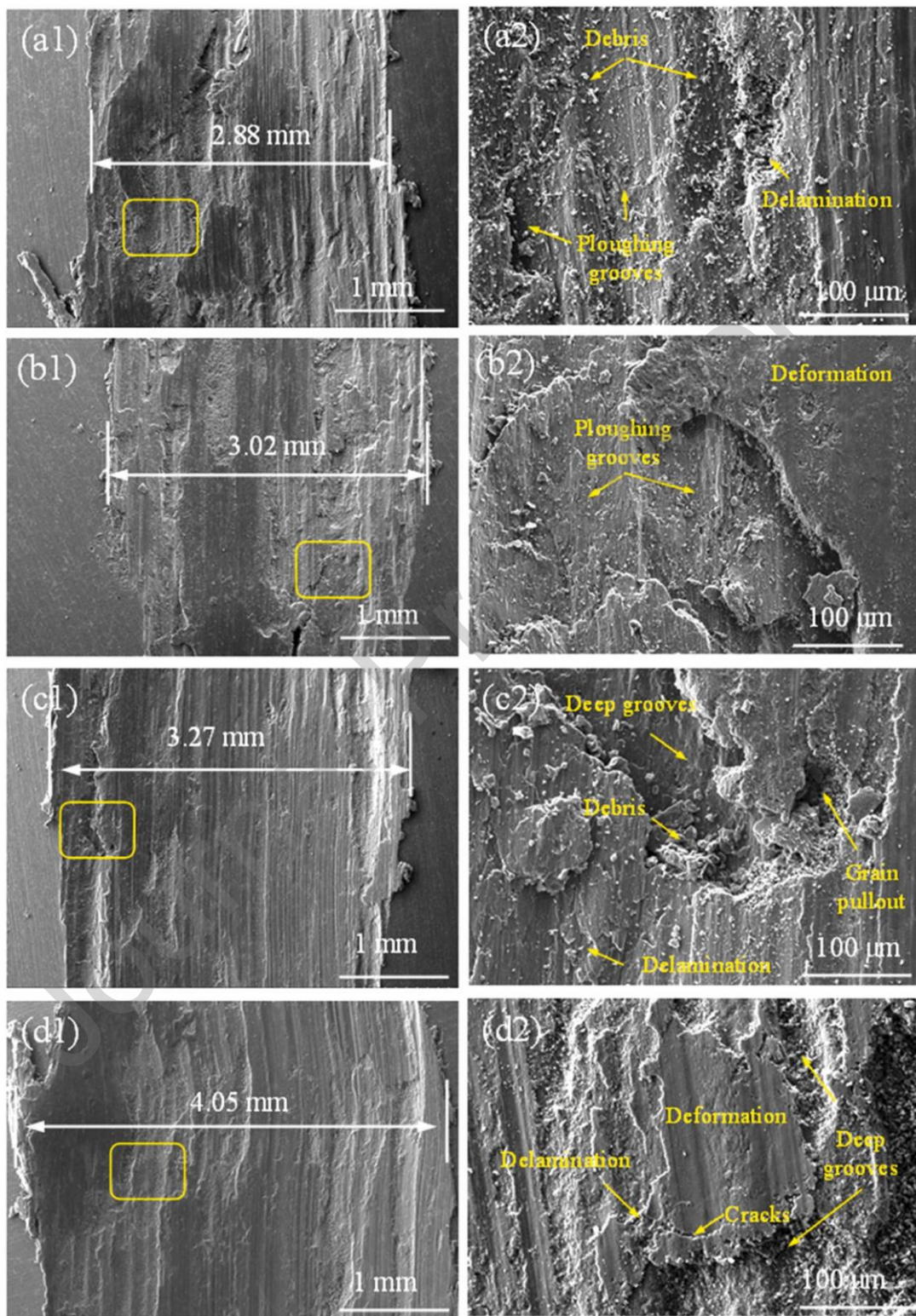


**Fig. 81** Wear track images of 3 wt.% HEA-MMC with fixed velocity and varying loads. (a1-d1) represents AA2219, 1.5 wt.%, 3.0 wt.%, 5.0 wt.% HEA-MMC. (a2-d2) are the explored view of the yellow rectangular area from a1-d1 [55].

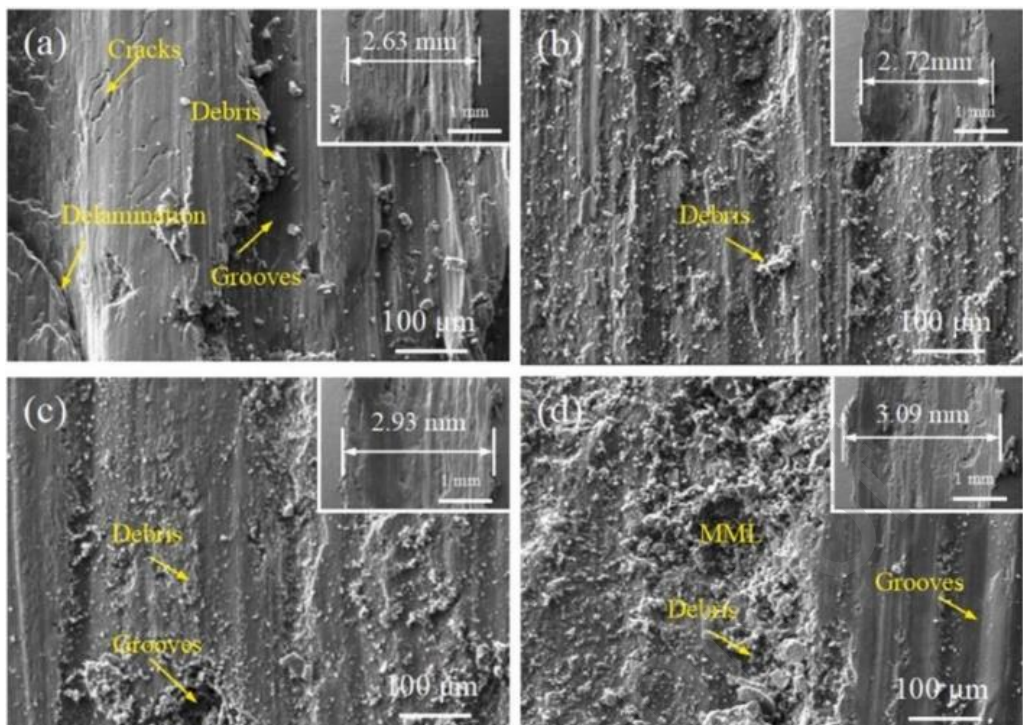


**Fig. 82 Wear track images of 3 wt.% HEA-MMC on fixed 30 N load with varying velocity of (a) 15 mm/s, (b) 30 mm/s, (c) 45 mm/s, (d) 60 mm/s [55].** Yang et al. [110] studied aluminum metal matrix composites reinforced with HEA prepared by cooling-assisted friction stir processing. A ball-on-disc wear testing set was used to evaluate the tribological performance at a normal force of 5 N, a sliding speed of 10 m s<sup>-1</sup> and a sliding distance of 9000 m. The wear rate and wear loss of the blend prepared with different volume % of HEA were analyzed. HEA at 15 vol.% shows a 43% and 57.8% reduction in wear rate and wear loss, respectively, compared to the monolithic matrix phase. In matrix adhesive wear works which converts into abrasive wear at 15% Al-HEA composites. **Fig. 83 (a)** clearly shows that the hardness changes from the base metal to the stir zone and it varies little in the stir zone, which confirms the uniform distribution of HEA particles in the alloy. At 15 wt.% HEA 136 HV hardness is found, 65.9% increase from the matrix (82 HV). The key effects of improved hardness are interface development, homogeneous distribution of HEA particles and refined grains. **Fig. 83 (b, c, d)** shows the coefficient of friction, wear rate and wear loss in graphical image. A continuous decrease in coefficient of friction is found after adding 0, 5, 10 and 15 wt.% of HEA in composite [129], [130]. From **Fig. 83 (c, d)** wear rate and loss both decrease as wt.% of HEA increases. The wear rate found at 15 wt.% HEA is  $8.5 \times 10^{-5}$  mm<sup>3</sup> m<sup>-1</sup>, which is 43% less than the matrix, and the wear loss is 1.6 mg, which is 57.8% compared to the base matrix. The improved tribological properties are attributed to the improved hardness of the composites. **Fig. 84** shows the wear worn surface of the composite with different wt% of HEA. The plowing and scratches are more severe in samples without HEA particle addition due to severe plastic deformation of the base metal sample [131]. The growth of HEA particle attachment provides more resistance to wear of the base metal, decreases in the creator of the composite surface and the thinner the surface. The 15 wt.% HEA composites pose less wear rate, wear loss and least coefficient of friction as compared to other samples.

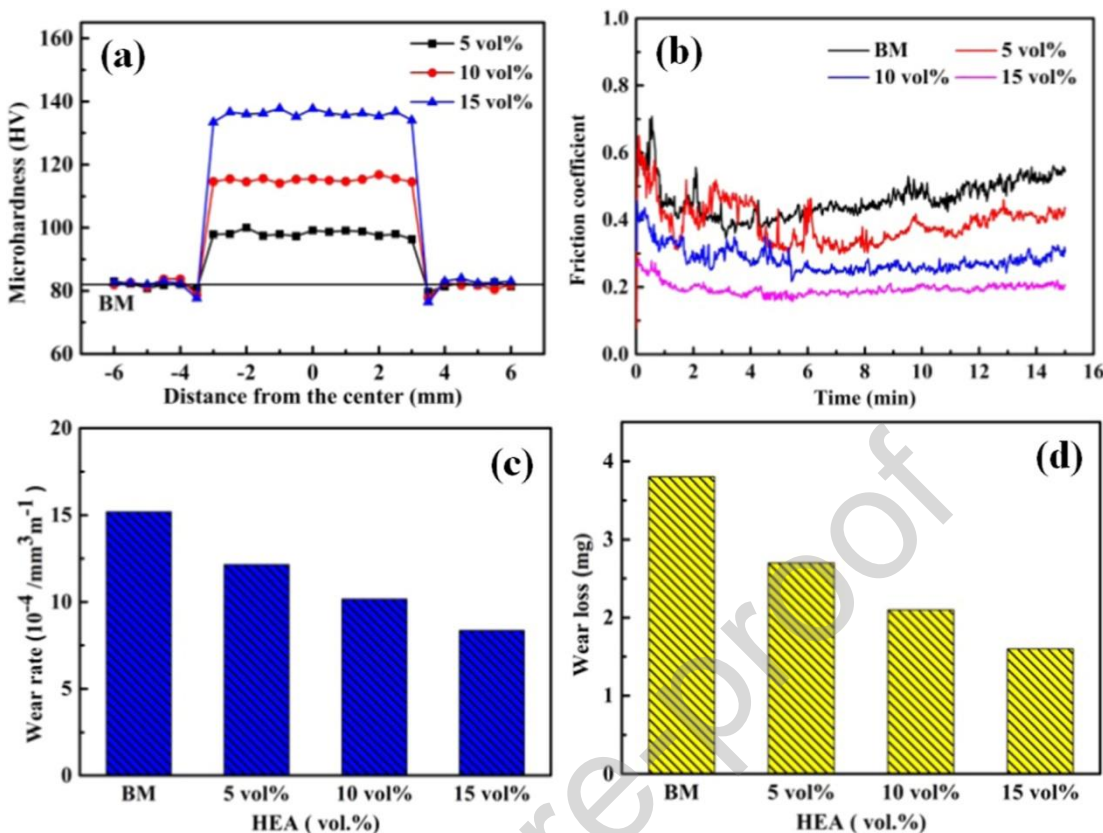


**Fig. 83** (a) Microhardness graph at stir zone, (b) Coefficient of friction graph, (c) wear rate of composite, (d) wear volume loss of composites at 0, 5, 10 and 15 wt. % HEA with aluminum matrix [110].

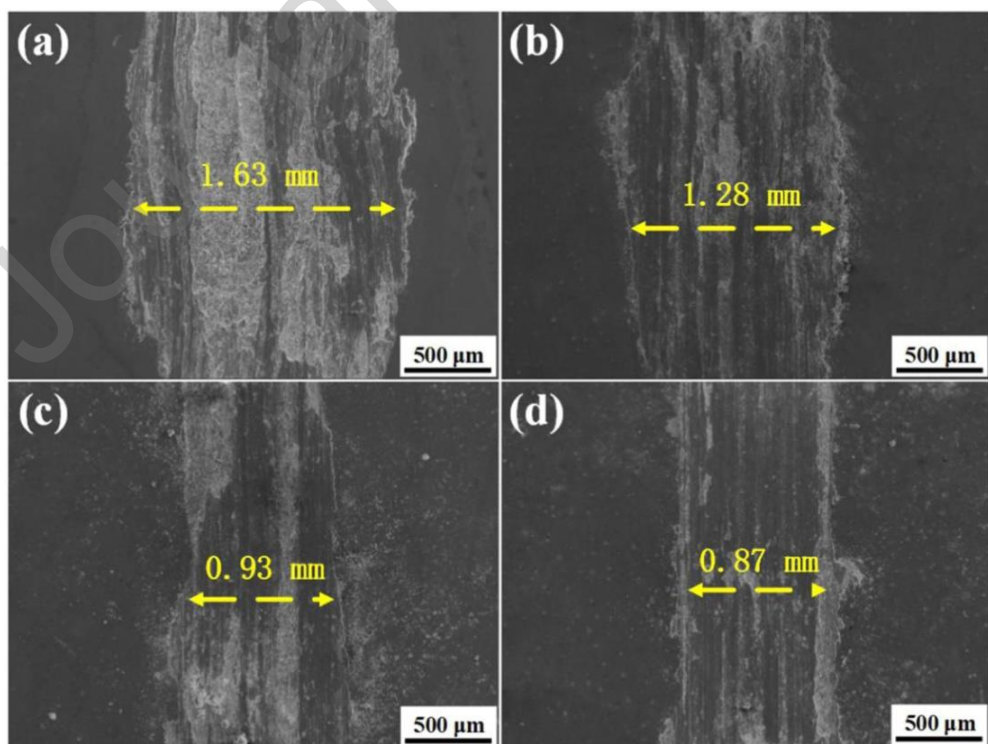


**Fig. 84** Wear surface SEM image of composite at (a) 0 wt.%, (b) 5 wt.%, (c) 10 wt.%, (d) 15 wt.% HEA [110].

#### 4.5 Effect of HEA reinforcement on thermal and electrical properties

It is important to study the evaluation of the thermal and electrical properties of the copper matrix, due to their good conductivity in both properties. Very little work has been reported on the thermal and electrical properties of HEA-Cu composite, however, this section presents a study of the thermal expansion behavior, electrical properties, and thermal conductivity of copper metal matrix reinforced with HEA particles. The effect of annealing heat treatment on thermal diffusion coefficient and thermal conductivity is also examined and discussed below.

Mane et al. [132] used the PM method to fabricate HEA-Cu MMC with different wt.% (0, 2.5, 5, 10) of HEA and studied the mechanical, wear and thermal properties of the composites. A single single-phase solid solution of HEA was obtained by mechanical mixing of the constituent elements for 15 h. A compression pressure of 700 MPa and a sintering temperature of 900°C were selected to conduct the experiment. The coefficient of thermal expansion (CTE) behavior of copper is used in heat sinks, electronic packaging, and heat passing of electronic components. In this property, the size of the material changes as temperature changes, due to this copper is preferred as it possesses a low mismatch of CTE [133]. The Cu possess CTE  $\alpha_{Cu} = 16.8 \times 10^{-6}/^{\circ}C$  and HEA possess CTE  $\alpha_{HEA} = 15 \times 10^{-6}/^{\circ}C$  which is near equal [134], [135]. The minute value change in CTE between composite and Cu matrix is shown in the **Fig. 85 (a)**. In **Fig. 85 (b)** the highest volume change (0.86 %) occurs at 0 wt.% HEA-Cu composite, which decreases as wt.% HEA increases and only 0.74% volumetric change is found at 10 wt.% HEA-Cu composite. At high temperatures, the CTE mismatch is much smaller in the HEA and Cu matrix, which increases strength, reduces creep and fatigue of alloys, and acts as a barrier to thermal stress generation [136].

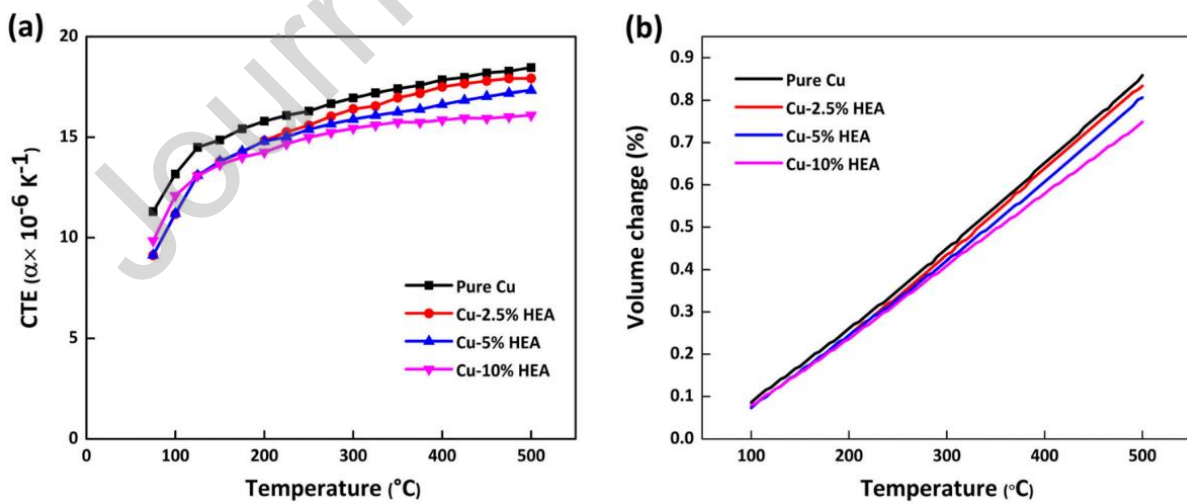


**Fig. 85** Graphs of HEA-Cu composite (a) Coefficient of thermal expansion (b) Volume change (%) Vs Temperature [132].

Zang et al. [137] prepared a Cu-HEA/diamond metal matrix composite coating by a mechanical composite method. Microhardness, wear resistance and thermal conductivity of the composites were measured. The

results show that the microstructure of the composite coatings was improved by annealing heat treatment. The effect of annealing heat treatment on the thermal conductivity of the composite coating was investigated. The coating thickness on pure copper was found to be uneven but continuous in form and the measured value was 100  $\mu\text{m}$  as shown in **Fig. 86**. Thermal conductivity of composite samples at unannealed condition, annealed condition at 500°C of composite, and pure copper for reference is tested. The thermal conductivity of the imperfect composite sample is 87.19  $\text{W}\cdot\text{m}^{-1}\cdot\text{K}^{-1}$ , which is much lower than that of pure copper and annealed composite because of residual stress, dislocation, sub-grain boundaries and lattice distortion. After relieving the annealing lattice distortion and residual stress, the density increased due to this recrystallization effect [138]. Close contact of diamond with the HEA-Cu composite after the annealing process also contributed to the improvement of the thermal performance. The annealing process improves the bond between the substrate and the coating material, resulting in an increase in thermal diffusion coefficient of the composite of 108.276  $\text{mm}^2\cdot\text{s}^{-1}$  and thermal conductivity of 358.53  $\text{W}\cdot\text{m}^{-1}\cdot\text{K}^{-1}$  and the thermal diffusion coefficient is 87.029  $\text{mm}^2\cdot\text{s}^{-1}$  and the thermal conductivity is 305.67  $\text{W}\cdot\text{m}^{-1}\cdot\text{K}^{-1}$ .

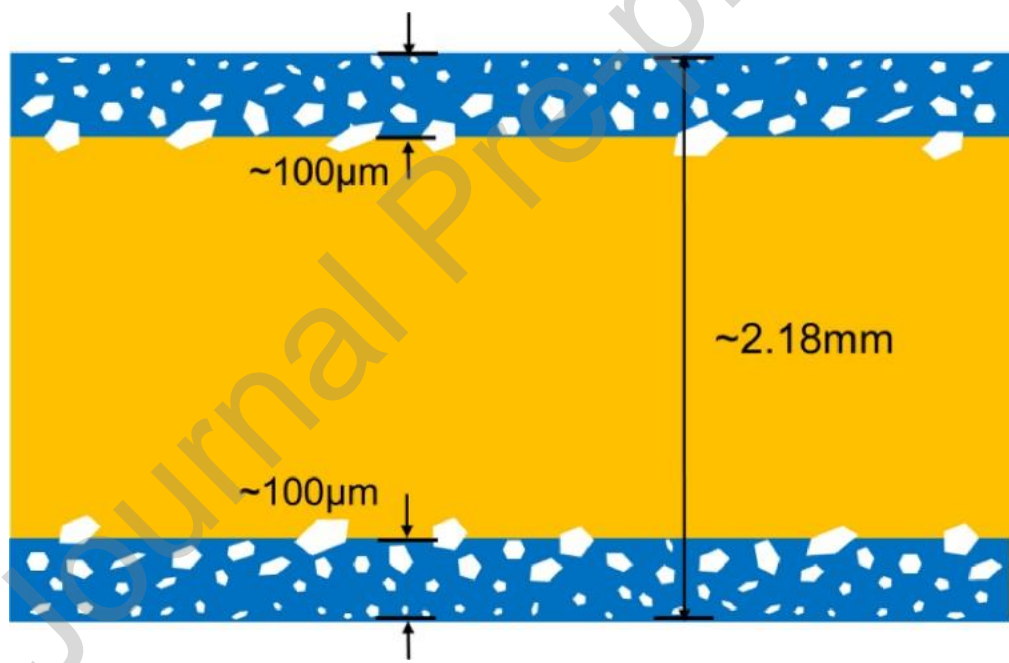


**Fig. 86** Representative diagram of composite coating sample [137]

Chen et al. [108] used TiZrNbTa with Cu matrix as HEA to fabricate the composite by SPS method and compression test was conducted with different wt.% HEA. The results show that the amount of HEA addition linearly increased the compressive strength and decreased the ductility of the composite. The stiff HEA particles resist dislocation of the weak matrix and form strong stable bonds with Cu. The strength and electrical conductivity values of 30, 40, and 50 HEA-Cu composite are 702 MPa (45.3%) IACS, 882 MPa (33.0%) IACS, and 953 MPa (22.0%) IACS, respectively, which are higher than pure bulk Cu. Compared to ceramic reinforcement such as Al<sub>2</sub>O<sub>3</sub>/Cu with 460 MPa (31.8%) IACS [120], ZrO<sub>2</sub>/Cu with 304 MPa and (45.9%) IACS [121], and metallic glass (CuZrAl) reinforced Cu matrix composite with 852 MPa (27.7%)

IACS, the HEA-Cu composite exhibits better balanced mechanical and electrical properties as shown **Table 9**.

**Table 9** Yield Strength and electrical conductivity of HEA-Cu composites.

HEA wt.% - Cu Composite	Yield strength (MPa)	Electrical conductivity (%IACS)
0	251	90.0
10	345	73.3
20	437	58.3
30	520	45.3
40	681	33.0
50	862	22.0

Kumar et al. [116] fabricated HEA-Al MMC by stir casting method by adding HEA at 5, 10, and 15 wt.%. **Fig. 87** results from HEA and matrix reaction at the interface presence of CuMgAl<sub>2</sub> HEA incorporation, uniform dispersion of HEA, and excellent bonding between reinforcement and matrix reduce the electrical resistance of the overall composite. The impurities used for reinforcement have low resistivity, thus reducing the electrical resistivity of the composite. The Mg and Cu dissolve at the interface, which increases their concentration and they form the CuAl<sub>2</sub> phase, the resistivity decreases as the reinforcement content increases.

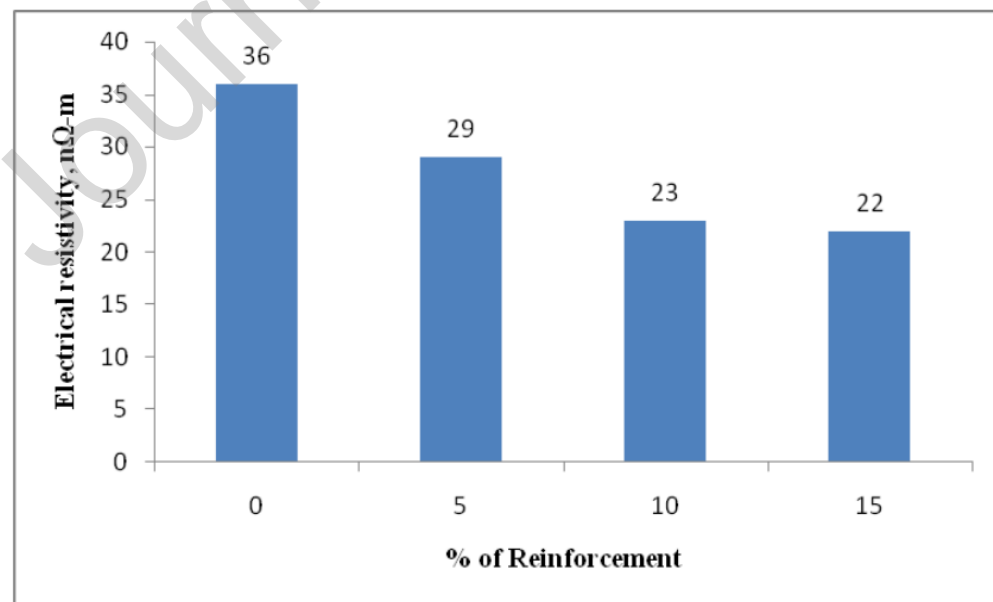


**Fig. 87** Electrical resistivity of HEA-Al MMC with HEA wt. % variation [116].

##### 5. Heat treatment (HT) effect on HEA based MMC.

A new topic of interest for researchers is to study the effects of heat treatment processes on HEA-MMCs. There is limited research that has been done in this area so far. Only special high entropy mixtures were examined under different heat treatment processes. Annealing and other heat treatment studies at different temperatures and different times have been studied for HEAs particles so far. Various researchers are studied the effect of heat treatment of different alloys with reinforcing HEA alloys are  $\text{Al}_{0.5}\text{CoCrFeMnNi}$  [139],  $\text{FeCrCuMnNi}$  [140],  $\text{AlCoCrFeNiTi}_{0.8}$  [141],  $\text{AlCoCrFeNi}$  [142], and  $\text{AlCoCrFeNi}$  [143].

Previous literatures are concerned with the effect of separate HEA and heat treatment on their mechanical and microstructural properties. The same effect needs to be studied on HEA-MMC, however, very little literature is available with heat treatment effect of HEA-MMC. Among them Yuan et al. [94] fabricate HEA-AMC by vacuum hot pressing sintering methodology and different temperature and time has been selected for finding the effect of heat treatment on interface layer. The Al5052 selected as matrix and  $\text{Al}_{0.6}\text{CoCrFeNi}$  (average 56  $\mu\text{m}$  particle size) as reinforcement in the composite. Heat treatment at 350°C, 500°C, and 600°C for 24 hours was done to investigate the interfacial characteristics of the composite and mechanical properties. The effect of holding time with 12 and 48 hours was studied in heat treatment at a temperature of 500°C shown in **Fig. 88**. It shows the diffusion layer formed around the reinforced particle in the aluminum matrix composite. Dark gray is the matrix phase, white is the spherical shape HEAp, and light gray is the diffusion layer after heat treatment of the mixture between matrix and reinforcement. **Fig. 88 (a)** represents a thinner diffusion layer as compared to **Fig. 88 (b)** because of less heat treatment time. It is observed that the distribution of the elements is in good condition in 24 h holding time. With increased holding time, a thick diffusion layer developed around the reinforced HEA particle with an uneven distribution of elements.

Spots A and B (**Fig. 88**) were detected at 12 h and C, D, E, and F were detected at 24 h heat-treated composites. An EDS analysis was examined to better understand the distribution of elements in the interface layers. The distribution of HEA elements in the interface layer is not uniform. The hysteresis effect in the diffusion kinetics of a high-entropy mixture and the different diffusion rates of its elements are contributing factors, resulting in variations in the distribution and content of each element in the interface layer. When compared to other elements, the distribution and content of Cr in the composites is lower. This may be due to the fact that iron and nickel have a large diffusion coefficient in aluminum, which causes the elements to diffuse into the matrix. The diffusion of Fe and Ni elements will inevitably occupy a portion of the near diffusion channel, resulting in a relatively reduced relative diffusion channel for the Cr element. This will slow and possibly even prevent the Cr element's outward diffusion. The elemental distribution results are prepared according to the distribution in Table 10 and **Fig. 89**. The concentrations of cobalt, iron, and nickel increase noticeably with particle distance in comparison to other elements. According to the binary phase diagram of iron, nickel, and aluminum, the expansion coefficients of Fe and Ni are larger than those of other elements in aluminum. In addition, the temperature range over which they react with aluminum to form intermetallic compounds is lower than that of other high entropy alloying elements, indicating that the

diffusion distance is relatively long because the elements are dispersed as atoms over long periods of time. As a result, it covers the entire aluminum surface.

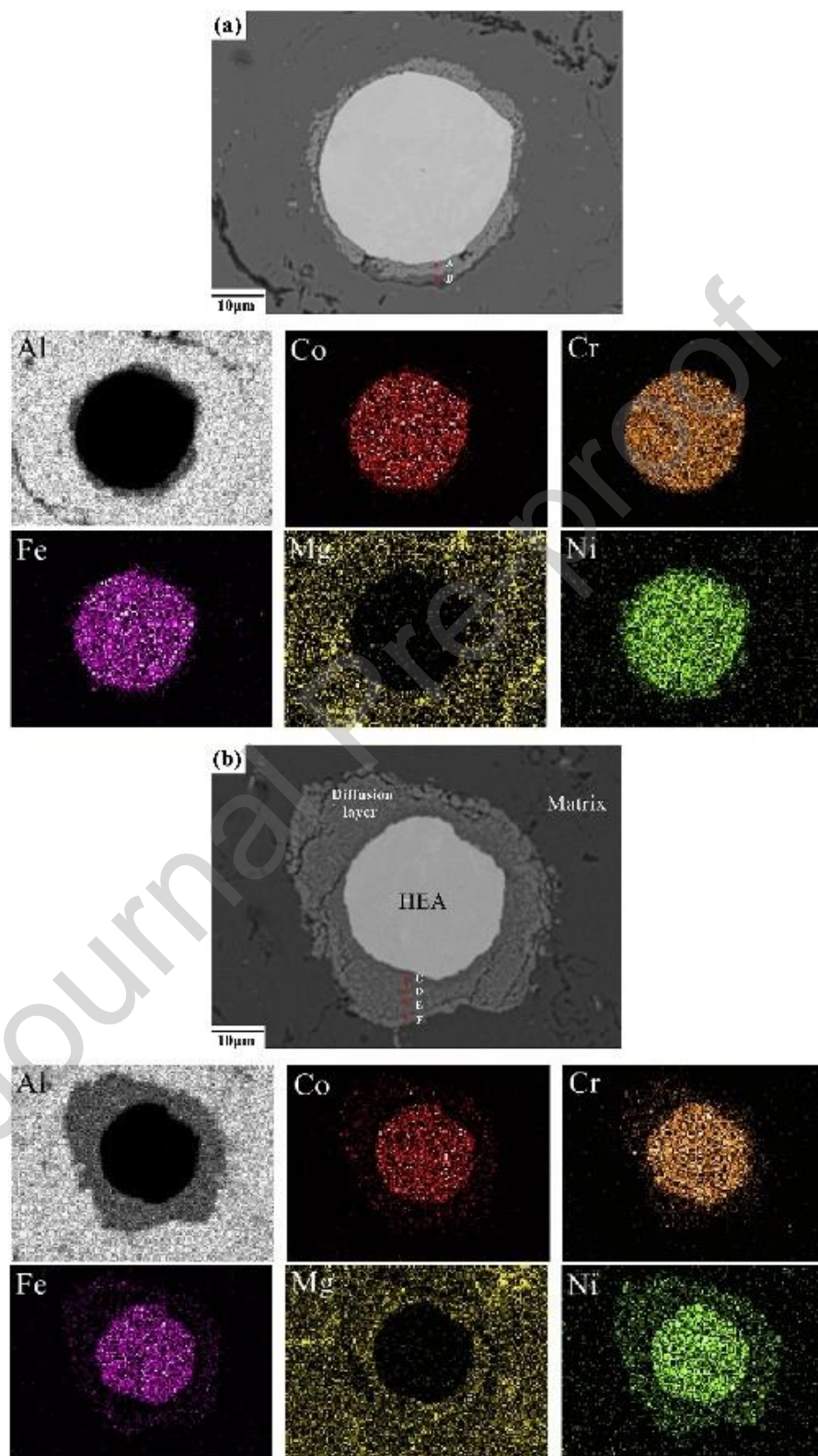


**Fig. 88** Variation of elements distribution in diffusion layer of composite at 500°C at (a) 12 h and (b) 24 h

[94].

By studying the relationship between HEAp and interface thickness, the maximum outer circle of the diffusion layer and near the HEAp surface, because the change in the uneven distribution of particles around the interface thickness and HEAp occurs by increasing the sintering temperature time. The inner circle center point is the center of the 12 segments for the study and the blue line is chosen as the starting point. The distance between the outer circle and the inner circle is measured for the interface thickness, which corresponds to the HEA particle boundary and is represented in **Fig. 90**. The interface layer thickness increases as the ratio of interface to particle thickness decreases. The HEAp boundary is not uniform at every location because the diffusion to the HEA and matrix is different. The matrix near the HEA is assumed to be the working area with R area, when R is positive the area perpendicular to the expansion decreases as the layer depth decreases, the opposite happens in negative R and summarize in **Fig. 90**. Various properties and fabrication technique of various high entropy alloys reinforced metal matrix composite by different researchers are listed in the Table 11.

**Table 10** Chemical composition of the composite diffusion layer (at.%).

Regions	Al	Fe	Zn	Mg	Mn	Cu	Si	Cr	Ni	Co
A	77.022	4.937	0.0883	1.3544	1.189	0.0383	3.344	4.915	3.646	3.466
B	80.322	4.451	0.0187	2.053	0.0828	0.1029	0.8826	0.809	6.316	4.962
C	80.467	3.432	0.0244	5.477	0.0463	0.1392	0.3581	3.652	2.585	3.819
D	80.335	3.154	0.0763	5.823	0.0579	0.1177	0.2781	3.784	2.707	3.667
E	80.733	3.869	0.1413	4.493	0.056	0.0564	0.2193	2.846	3.977	3.609
F	81.24	5.717	–	1.0889	0.0356	–	0.241	0.3255	5.715	5.637

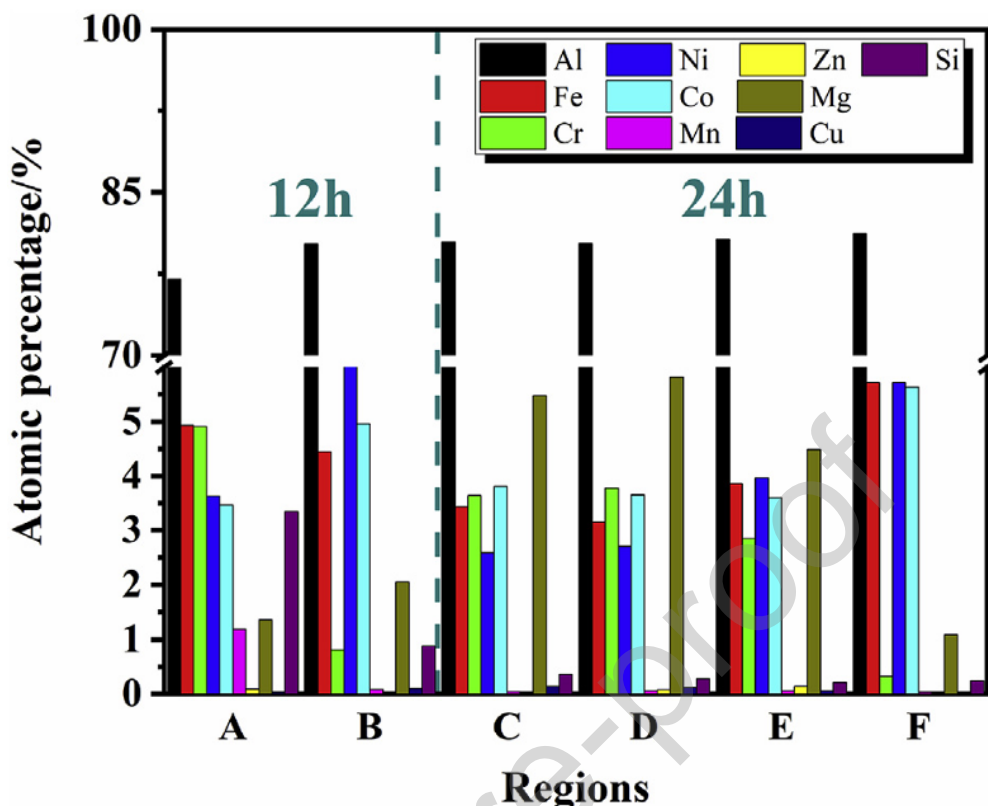


**Fig. 89** Elements distribution at diffusion layer after heat treatment represented in **Table 10** [94].

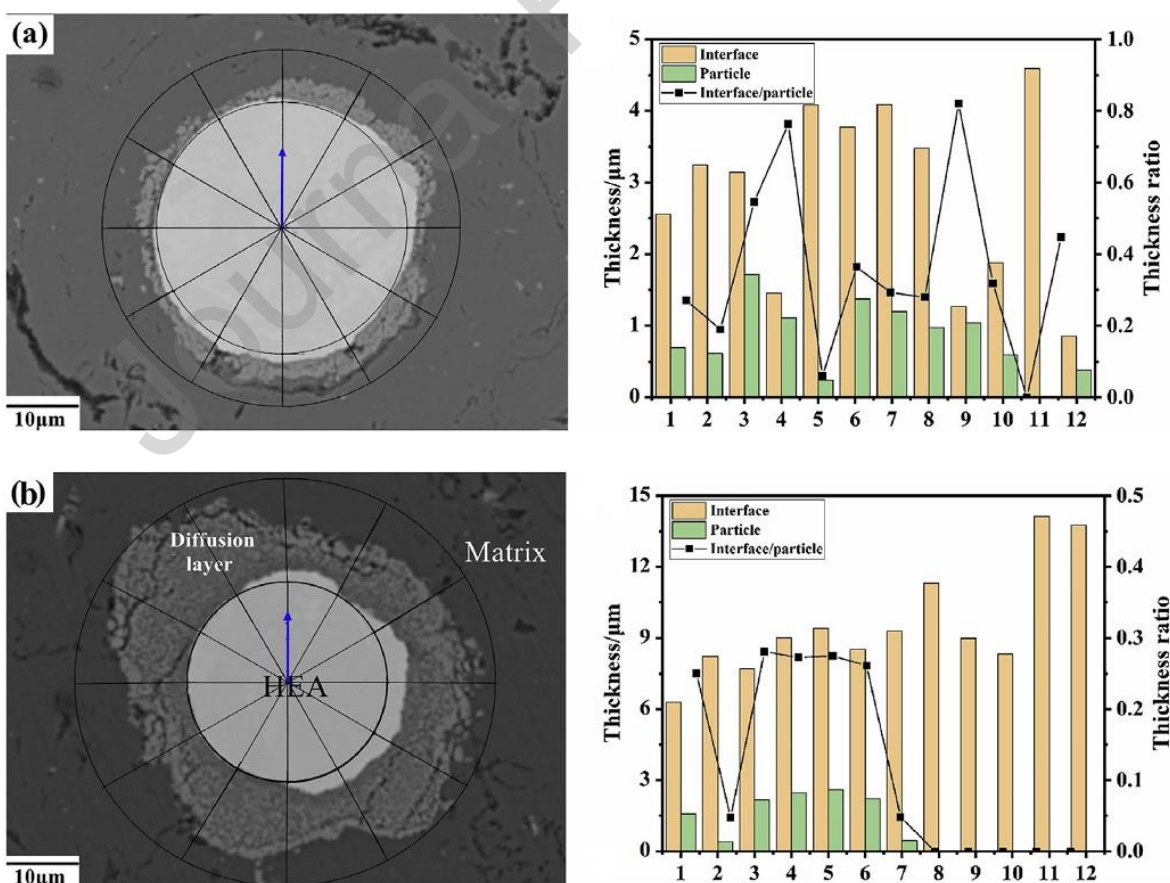


**Fig. 90** Study of curves of composite at 500 °C sintering time in (a) 12h (b) 24h [94]

**Table 11** listed the different properties and fabrication technique of various high entropy alloys reinforced metal matrix matrix composite by different researchers.

S.No	Year	Matrix	Reinforcement (HEA)	Method	Reference	Properties
1	2021	Aluminum	FeCoNi <sub>1.5</sub> CrCu	low-temperature microwave sintering	Wang et al. [30]	• Maximum compressive strength 248.7 MPa, YS 227.4 MPa and microhardness 93.1 HV at 40 min sintering time of 15 wt. % HEA-Al MMC.
2	2015	Copper	AlCoNiCrFe	Powder Metallurgy (PM)	Chen et al. [31]	• HEA-Cu composite compressive yield strength at 10 % HEA is 240 MPa and 20 % HEA is 330 MPa
3	2017	Aluminum 6061	CrMnFeNiCu	Powder Metallurgy (PM)	Prabakaran et al. [32]	• 18 % improvement in hardness at 600°C for 2 Hr. • 10 % HEA-Al composite possess higher hardness as compared to

							20 % HEA-Al composite.
4	2021	Aluminum 1050	MoTaNbVW	Powder Metallurgy (PM)	Ananiadis et al. [33]	• Highest harness and corrosion resistance offered by 5 % HEA-Al MMC.	
5	2020	Aluminum 5083	AlCoCrFeNi	Submerged friction stir processing (SFSP)	Yang et al. [51]	• Hardness improved 65.9% (136 HV) as compared to base matrix at 15 wt.% HEA. • At 15 wt.% HEA-Al Composite wear rate was $8.5 \times 10^{-5}$ mm <sup>-3</sup> m <sup>-1</sup> and wear loss were 1.6 mg which is 43.0 % and 57.8 % lesser as compared to base matrix.	
6	2022	Aluminum 2024	Al <sub>0.5</sub> CoCrFeNi	Stir Casting (SC)	Li et al. [52] and rolling	• 1 % HEA-Al CR tensile strength 543 MPa (Alloy 70 MPa) and 10 % elongation.	

7	2022	Aluminum 1050	$\text{Al}_{0.5}\text{CoCrFeNi}$	Stir (SC)	Casting and rolling	Luo et al. [53]	<ul style="list-style-type: none"> <li>• 3 % HEA-Al has UTS of 115 MPa, 74.3 % higher than alloy.</li> </ul>
8	2021	Aluminum 2219	$\text{AlCoCrFeNi}$	Ultrasonic Stir Casting	Zhang et al. [54]	<ul style="list-style-type: none"> <li>• Strength of CR 3% HEA-Al was 15.1 % higher than RTR at 50 % deformation.</li> </ul>	
9	2022	Aluminum 2219	$\text{Al}_{0.5}\text{CoCrFeNi}$	Ultrasonic Stir Casting	Zhang et al. [55]	<ul style="list-style-type: none"> <li>• Optimum tensile strength 217.4 MPa for 1.5 wt.% HEA-Al MMC.</li> <li>• Maximum micro-hardness 120.5 HV for 3 wt.% HEA-Al MMC.</li> <li>• Optimum hardness 120.5 HV of 3 wt. % HEA-Al MMC.</li> <li>• Wear performance improved for 0.5 to 3 wt. % HEA-Al MMC compared to Al alloy.</li> </ul>	

10	2017	Aluminum 5083	CoCrFeNi	Additive Manufacturin g (AM)	Karthik et al. [68]	• 12 vol. % HEA content with Al shows increase in tensile and compressive strength compared to Al alloy.
11	2019	Tungsten Carbide (WC)	CrMnFeCoNi	Laser melting deposition (LMD) Additive manufacturing	Li et al. [69]	• Tensile strength 800 MPa and elongation 37 % of 5 wt% HEA-WC MMC.
12	2021	Stainless Steel 316L	FeCoNiCr	Laser powder bed fusion (LPBF)	Zhang et al. [88]	• HEA-SS composite YS of 532.8 MPa, UTS of 627 MPa, elongation found above 50%. • Corrosion resistance improved 62.4% as compared to pure matrix.
13	2019	Aluminum 2024	CoCrFeMnNi	Spark Plasma Sintering (SPS)	Yuan et al. [91]	• Highest hardness of composite 135.48 HV achieved due to ID layer

						and HEA addition.
14	2019	Aluminum	AlCoCrFeNi	Spark Plasma Sintering (SPS)	Liu et al. [93]	<ul style="list-style-type: none"> <li>With transition layer strength is 137 MPa of 5vol% HEA-Al composite at 580 °C.</li> </ul>
15	2020	Aluminum 5052	Al <sub>0.6</sub> CoCrFeNi	Vacuum hot pressing sintering	Yuan et al. [94]	<ul style="list-style-type: none"> <li>Young's modulus 80 GPa, macro (1.81 GPa) and micro hardness (178 HV) at 500 °C heat treatment temp.</li> </ul>
16	2015	Aluminum 2024	Al-20Cu-10Mg	Stir Casting (SC)	Kumar et al. [116]	<ul style="list-style-type: none"> <li>Electrical resistivity of composite decreases with HEA addition.</li> <li>Increment of 62% (102 VHN) hardness by 15% HEA in Al matrix.</li> <li>YS 405.78 MPa, UTS 563.65 MPa, Young's Modulus 102.69 GPa, Elongation 8.64 % of 15%</li> </ul>

						HEA-Al MMC.
17	2020	Aluminum	CuZrNiAlTiW	Mechanical alloying and Spark Plasma Sintering (SPS)	Wang et al. [96]	<ul style="list-style-type: none"> <li>• Microhardness s 331 HV, compression strength, and optimum pitting resistance of 30 % HEA-Al composite.</li> </ul>
18	2019	Aluminum 2024	CoNiFeCrAl <sub>0.6</sub> Ti <sub>0.4</sub>	Ball milling, hot pressing, hot extrusion and heat treatment.	Lu et al. [123]	<ul style="list-style-type: none"> <li>• Yield strength <math>419 \pm 12</math> MPa of 7.5HEA-Al 112 MPa than Al alloy.</li> </ul>
19	2019	Aluminum 6061	CoNiFeAl <sub>0.4</sub> Ti <sub>0.6</sub> Cr <sub>0.5</sub>	Powder Metallurgy (PM)	Chen et al. [124]	<ul style="list-style-type: none"> <li>• 40 h HEA-Al composite UTS 378 MPa and fracture strain 8.4%.</li> </ul>
20	2022	Aluminum 7075	AlCrTiV	Stir Casting (SC)	Huang et al. [125]	<ul style="list-style-type: none"> <li>• Grain refinement improves YS, UTS and Elastic Modulus as compared to alloy.</li> </ul>
21	2022	Aluminum 7075	CrCuFeMnNi	Supersonic vibration with stir and squeeze infiltration	Pandian et al. [127]	<ul style="list-style-type: none"> <li>• Maximum hardness 230.20 HV, impact strength 12.06 %, wear and</li> </ul>

						corrosion resistance at 10 wt.% HEA-Al as compare to other HEA wt.% and alloy.
22	2020	Aluminum	AlCoCrFeNiTi	Stir Casting (Vacuum arc melting)	Li et al. [144]	• At 3 % HEA- Al MMC UTS 152 MPa, YS 115 MPa, and elongation reduced to 26 %.
23	2022	Aluminum	Al <sub>0.5</sub> CoCrFeNi 1050	Stir Casting (SC)	Luo et al. [145]	• Optimum UTS 115 MPa (154% higher) and elongation 32.1% (32% higher) for 3 wt.% HEA-Al MMC.
24	2022	Aluminum	AlCoCrFeNi	Theoretical Research, first- principles calculations	Liu et al. [146]	• HEA reinforcement enhances Young's modulus of Al from 69 GPa to 134 GPa.
25	2021	Aluminum	CoCrFeNi	Spark Plasma Sintering (SPS)	Liu et al. [147]	• The interfacial shell has higher creep resistance as compare to

					HEA and Al matrix itself.
26	2019	Aluminum	AlCoCrCuFe	Powder Metallurgy (PM)	<ul style="list-style-type: none"> <li>• Compression strength increased 2.6 times compared to pure Al.</li> </ul>
27	2022	Titanium	CoCrFeNiMo <sub>0.2</sub>	Vacuum hot pressing sintering	<ul style="list-style-type: none"> <li>• Maximum microhardness 71.3 HV for 15% HEA-Al MMC.</li> <li>• Composite density increased with addition of HEA reinforcement .</li> </ul>
28	2019	Tungsten	CoCrFeMnNi	Powder Metallurgy (PM)	<ul style="list-style-type: none"> <li>• Maximum hardness found 402.6 HV at 850 °C.</li> <li>• Highest Yield strength of 928.2 MPa and Compressive strength of 2032.6 MPa at 850 °C.</li> </ul>
					<ul style="list-style-type: none"> <li>• Higher compressive strength (2041 MPa) in SPS</li> </ul>

					Conventional, MW, SPS		as compared to CS, MWS.
29	2019	Magnesium	$\text{Al}_{20}\text{Mg}_{20}\text{Li}_{20}\text{Cu}_{20}\text{Zn}_2$	Powder Metallurgy (PM)	Tun et al. [104]	<ul style="list-style-type: none"> <li>• Maximum 54% (103 HV) improved hardness in 7.5wt. % HEA.</li> <li>• UTS of 220 MPa at 7.5HEA-MMC in tension.</li> <li>• UTS of 471 MPa at 7.5HEA-MMC in compression.</li> </ul>	
30	2022	Aluminum 7075	$\text{FeCoCrNiAl}$	Vacuum hot pressing sintering	Gao et al. [149]	<ul style="list-style-type: none"> <li>• Flexural strength and fracture toughness increased by 124.6% and 107% through 10% HEA addition in Al matrix.</li> </ul>	

31	2023	Copper	FeCoNiMnCr	Powder Metallurgy (PM)	Mane et al. [132]	<ul style="list-style-type: none"> <li>• 10% HEA-Cu shows highest hardness 69 HV, compressive strength 471.43 MPa.</li> <li>• COF of 0.4 and highest wear resistance found for 10% HEA-Cu composite.</li> <li>• Only 13% CTE found between 10% HEA-Cu composite and pure copper.</li> </ul>
32	2020	Copper	Cu <sub>2</sub> AlNiZnAg	Mechanical Alloying	Zang et al. [137]	<ul style="list-style-type: none"> <li>• Thermal diffusion coefficient 108.276 mm<sup>2</sup>•s<sup>-1</sup> of annealed composite higher than unannealed composite and pure copper.</li> <li>• Thermal conductivity of composite coating found 358.53 W•m<sup>-1</sup>•K<sup>-1</sup></li> </ul>

							higher than pure Cu.
33	2023	Copper	TiZrNbTa	Spark Plasma Sintering (SPS)	Chen et al. [108]	• The 40 HEA wt.% - Cu composite exhibits balanced compressive strength of 882 MPa, and electrical conductivity of 33.0 % IACS.	
34	2024	Aluminum	Al <sub>35</sub> Ti <sub>15</sub> Cu <sub>10</sub> Mn <sub>20</sub> Cr <sub>2</sub> . <sub>0</sub>	Spark Plasma Sintering (SPS)	Zhu et al. [97]	• The 40 HEA wt.%-Al composite shows max. hardness of 225 HB.	
35	2024	Aluminum	CoCrFeNi 6061	Spark Plasma Sintering (SPS)	Xiao et al. [98]	• Tensile strength of 211.5 MPa	

## 6. Evaluation of strengthening mechanisms of HEA reinforcement based MMC

For predicting the strengthening behavior of HEA reinforced MMC different theories are available. These strengthening mechanism models are used to predict the increase in yield strength in HEA reinforced MMC. The strengthening mechanism induced by reinforcement particles in the metal matrix can be primarily understood by grain refinement strengthening [109] [110], load transfer strengthening [87], coefficient of thermal mismatch strengthening [111] and Orowan strengthening [112].

The parameters related to strengthening mechanisms were discussed by Basu et al. [150] who discussed strengthening mechanisms issues of multi-phase HEAs. Attempts have been made to make a comparison between single-phase and multi-phase HEA Zhang et al. [54] developed HEA reinforced MMC with ultrasonic probe stir casting and evaluated the strength of the composite. Srivastava et al. [151] used ultrasonic processing to fabricate Al6061 composite reinforced with HEA. The effect on mechanical

properties and microstructure was analyzed by Hall-Pech strengthening, Orowan strengthening and coefficient of thermal imbalance between matrix and reinforcement. Luo et al. [145] studied seven strengthening mechanisms of HEA-AMC fabricated by stir casting method. Theoretical values and experimental values were compared and only 4.2% error was found. The various strengthening mechanisms are discussed in the successive section.

### **(1) Grain refinement strengthening**

This mechanism describes the effect of grain size on MMC. At smaller grain sizes, the grains are refined and this increases grain boundaries that can resist dislocation movement as a result of this yield strength of composite will be enhanced [152]. According to the Hall-Pech relationship the decrease in the grain size of the Al matrix increases the yield strength of the composite. The Hall-Petch relationship [153] given by as Eq. (2) :

$$\Delta\sigma_{Hall-Petch} = k_{H-P} \left( \frac{1}{\sqrt{d}} - \frac{1}{\sqrt{d_o}} \right) \quad (2)$$

Where  $d$ ,  $d_o$  is the average grain size of composite and Al alloy respectively and  $k_{H-P}$  is Hall-Petch constant whose value was taken as 74 MPa  $\mu m^{1/2}$  [154].

### **(2) Orowan strengthening**

Orowan strengthening is important for aluminum alloys but not sufficient for reinforced MMCs of fine size particles. Furthermore, the coarser particles have larger interparticle spacing and because the particles are located at the grain boundaries of the matrix, the strengthening of Orowan becomes irrelevant under these conditions. Strengthening is important for nano size reinforcement in AMC Orowan because small size closely spaced hard reinforcement particles induce resistance to dislocation movement in composites [155]. A small volume of HEAp also increases the resistance to deformation and promotes the prevention of particle movement in the composite [156]. This strengthening depends on the inter-particle space of HEA reinforcement particles on an aluminum metal matrix. The relationship between Orowan strengthening and  $\lambda$  inter-particle space is expressed by Eq. (3) [157].

$$\Delta\sigma_{Orowan} = \frac{0.13Gb}{\lambda} \ln \frac{D}{2b} \quad (3)$$

$$G = \frac{E}{2(1 + \nu)} \quad (4)$$

Where  $G$  shows shear modulus of aluminium whose value was 25.4 GPa given by Liu et al. [158],  $E$  is the elastic modulus of aluminium alloy and its value is 70 GPa,  $\nu$  is the poisson's ratio of aluminium matrix

which is 0.33 [159],  $b$  is Burger's vector with the value of 0.286 nm for the aluminum alloy,  $D$  shows average diameter of HEAp and  $\lambda$  is inter-particle spacing and given as [160]:

$$\lambda = D \left[ \left( \frac{1}{2V_p} \right)^{1/3} - 1 \right] \quad (5)$$

Where  $V_p$  shows the volume fraction of HEAp.

### (3) Load transfer strengthening

The load transfer strengthening mechanism was explained as the load transferred from reinforcement particles to the weak matrix when external force applied on composite. Goh et al. [161] used the equation for load transfer from the particle reinforcement phase to the aluminum matrix weak phase and is given by Eq. (6) as follows:

$$\Delta\sigma_{Load} = \frac{1}{2} V_p \sigma_m \quad (6)$$

Where  $\sigma_m$  is the yield strength of aluminum matrix.

It is clear from above equation that load transfer mechanism is directionally proportional to volume of reinforcement phase. Thus, small volume fraction of HEAp in composite contribute less in increased strength of composite and increase in volume of HEAp will enhance the strength of composite.

### (4) Coefficient of thermal expansion (CTE) mismatch strengthening

There is difference in CTE value of HEAp and matrix materials. Due to this CTE difference during the fabrication process of HEA reinforced MMC a residual plastic strain is produced from the experiment temperature to room temperature. Zhu et al. [162] concluded that these residual plastic strains further increase the dislocation density in the composite material. This enhanced dislocation density will increase the strength of HEA reinforced AMC. The difference in CTE accounts for the increase in strength and can be given by the following equation based on a study by G Gupta et al. [163] and Chen et al. [164].

$$\Delta\sigma_{CTE} = \eta G b \sqrt{\rho} \quad (7)$$

Where,  $\eta$  is the strengthening constant with value nearly equal to 1. Dislocation density ( $\rho$ ) is caused by mismatch in CTE and given by following equation [156]:

$$\rho = \frac{A \Delta \alpha \Delta T V_p}{b D (1 - V_p)} \quad (8)$$

Where  $A$  is a constant with value of 12 [165],  $\Delta\alpha$  is the difference of CTE between reinforcement particle and Al matrix ( $24.6 \times 10^{-6} K^{-1}$ ) [163] and  $\Delta T$  is the temperature change between pouring of molten metal and experimental temperature.

#### (5) Modulus mismatch strengthening

There is a difference in modulus existing between HEAp reinforcement and  $\alpha$ -Al matrix. Therefore, modulus mismatch strengthening happens with AMCs. To overcome from modulus difference between HEAp and aluminium metal matrix, the HEAp generates geometrical necessary dislocations (GNDs) in HEA reinforced AMC. Luo et al. [145] found that the dislocation in the microstructure of AMC is due to the modulus mismatch between the HEAp phase and the aluminum matrix phase. The composite change in microstructure with the introduction of HEAp is known as geometrically necessary dislocations (GNDs) [166]. Dai et al. [167] used the relationship between strength and modulus mismatch is as follows:

$$\Delta\sigma_{modulus} = \gamma G b \sqrt{\frac{18V\varepsilon}{bd_p}} \quad (9)$$

Where coefficient of dislocation strengthening is  $\gamma$  and its value was 0.5 reported by Dai et al. [167] in their study. The bulk strain of the HEA-AMCs is  $\varepsilon$  and it was taken as plastic strain in Jayalakshmi et al. [168] study.

#### (6) Secondary dislocation strengthening

A difference in elastic modulus occurs between the reinforced particles and the aluminum metal matrix. At the application of an external load, the composite feels deformed, the deformation of the matrix and the reinforcement cells do not match each other. Elastic deformation involves secondary slip around the interface between the matrix and the reinforcement particles. Due to enhanced strain in the composite the dislocation density increased. This secondary dislocation restricts the deformation and enhances the strength of composite. Based on the study of Alizadeh et al. [159] the relationship in secondary dislocation strengthening was given as follows:

$$\Delta\sigma_{WH1} = KG \left( \frac{V_p b \varepsilon}{d_p} \right)^{1/2} \quad (10)$$

Where constant  $K$  lies between 0.2 to 0.4 [159],  $\varepsilon$  and  $V_p$  represents tensile strain with 0.002 value and volume fraction of reinforced particles respectively.

#### (7) Geometrically necessary dislocation (GNDs) strengthening

The GNDs will occur in alloy matrix with deformation in the composite. Due to the difference of elastic modulus in the matrix and reinforcement, the composite begins with the application of load deformation and

the deformation gradient transfers from the matrix to the HEAp. To achieve this gradient, the matrix begins to transform and the yield strength of the composite improves. Alizadeh et al. [159] used the following relation to quantify this strengthening effect:

$$\Delta\sigma_{WH2} = 2G_m \left( \frac{1-\nu}{1-2\nu} \right) V_p \varepsilon \quad (11)$$

Where  $\varepsilon$  is tensile strain during loading with value of 0.002 and  $\nu$  is poissions ratio of Al matrix and its value id 0.33, described earlier.

The overall yield strength of HEA-MMC was predicted based on the indirect strengthening effect of reinforcement HEAp in the HEA-MMC, which was described above. The required expression for this expressed by following Eq. (12).

$$\sigma_{cy} = \sigma_{my} + (\Delta\sigma_{Hall-Petch} + \Delta\sigma_{Orowan} + \Delta\sigma_{Load} + \Delta\sigma_{CTE} + \Delta\sigma_{modulus} + \Delta\sigma_{WH1} + \Delta\sigma_{WH2}) \quad (12)$$

Furthermore, the contribution of these strengthening mechanisms on the overall yield strength of HEA reinforced AMC composites was studied by Luo et al.[145]. From **Fig. 91**, Orovan reinforcement has the greatest effect on yield strength and CTE and fine grain reinforcement also play an important role in strengthening the composite.

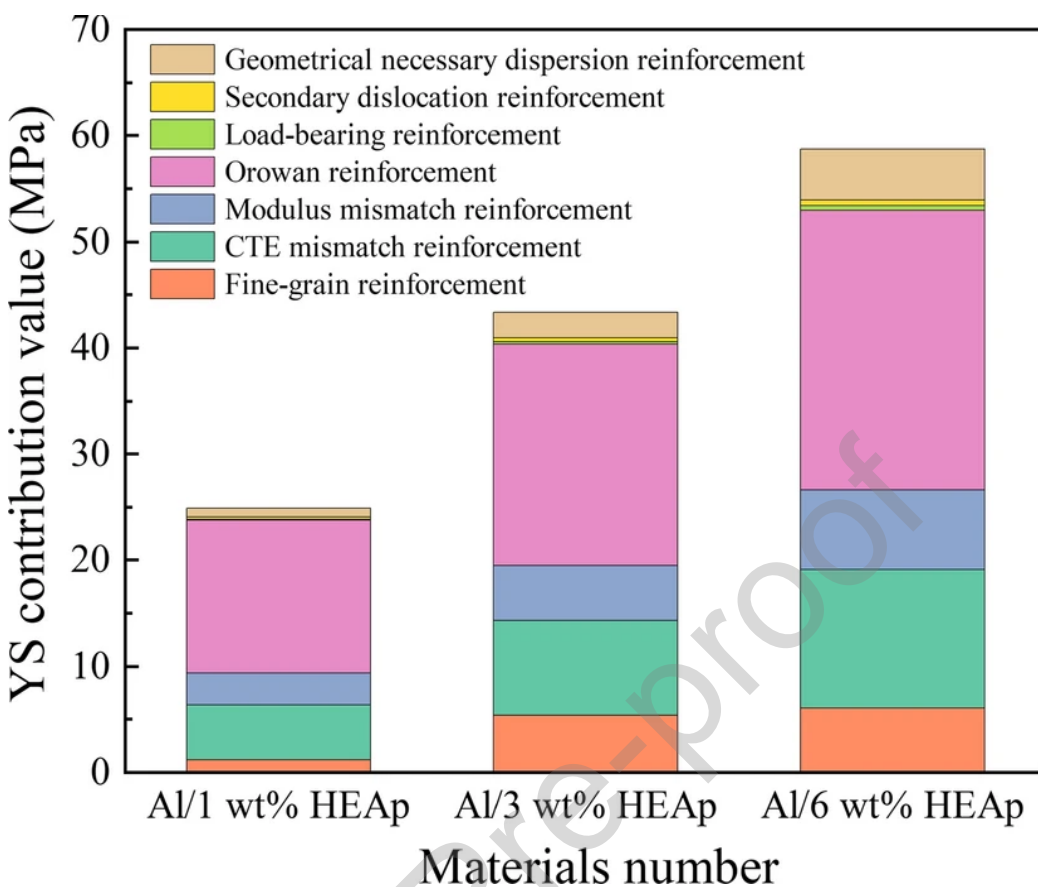


**Fig. 91** Different strengthening mechanisms contributing to total strength of HEA-AMC [145].

## 7. Applications

The enhanced properties by HEAs have attracted researchers to further work in the field of HEA-reinforced MMCs. 3M, CPS Technologies, GKN Sinter Metals, Materion and Santier are the top five companies engaged in metal matrix components. Aerospace application [127] requires the use of lightweight and high-strength HEA-reinforced MMC materials for biomedical components, implants, and structures.

### *Automobile Applications:*

Automobile components such as piston insert rings, cylindrical engine blocks, pistons, disc brakes, connecting rods, etc. are made of aluminum alloys. The alloy has a high strength-density ratio and excellent mechanical properties showing high ductility, stiffness and toughness, high corrosion resistance and high strength and temperature capability. However, low wear resistance, strength and hardness are disadvantages of the alloy for applications. The improved mechanical properties obtained by introducing HEA into such a weak matrix led to the use of HEA reinforced MMCs. **Fig. 92** indicates different application field of HEA- MMCs.

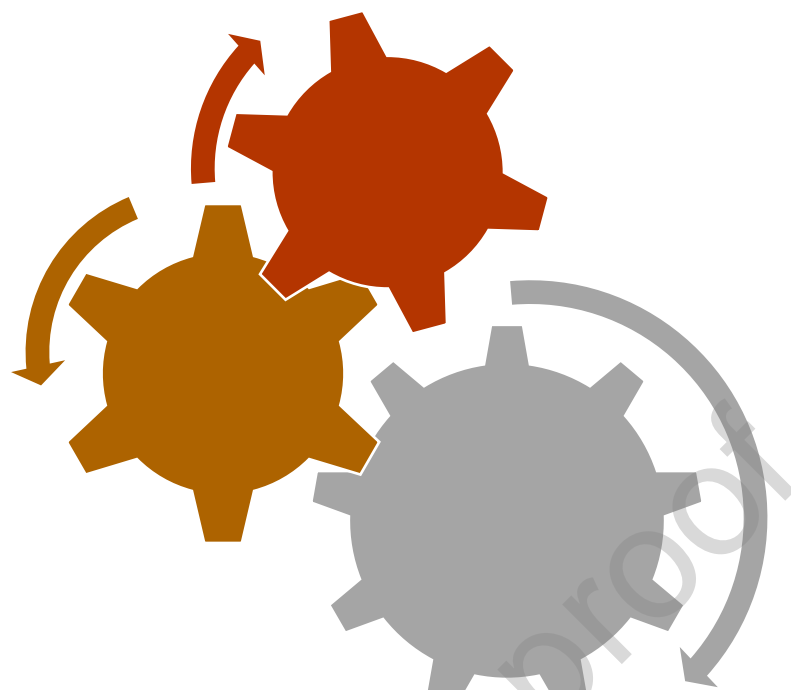


**Fig. 92** Different application field of HEA-MMCs

***Aerospace Applications:***

Refractory HEA coatings are used in the aerospace field for high-temperature and power applications [169] and can be used as a reinforcing particle with aluminum and magnesium to make lightweight HEA-reinforced MMCs. A research article published by Prabhu et al. [170] from CEMILAC Defense R&D Organization, Bangalore used the powder metallurgy method for self-composite with HEA and graphite. The braking system of military aircraft was tested. Landing Gear aerospace [171] applications are fields where HEA is effective. Metal matrix composite for aviation engines [172] are being suggested for their improved mechanical properties.

***Biomedical Applications:***

Metals are being used for a wide range of biomedical applications. Metallic materials are used as biomaterials for the proper functioning of human body parts. Mechanical properties such as high hardness, strength, as well as ductility and good biocompatibility, wear resistance, and good corrosion resistance, are requirements of biomaterials [173], [174]. High entropy composites are suitable materials for biomedical applications because of these properties [175].

## 8. Prime Importance, challenges and perspectives

Due to their special qualities and extensive range of possible applications, composites based on high entropy alloys (HEAs) have attracted a lot of interest in the field of materials science. Composites based on HEA often have remarkable mechanical qualities, such as great strength and hardness. When many elements are present in about equiatomic amounts, a solid solution is formed that is stronger than conventional alloys. HEA-based composites are extremely resistant to wear and abrasion due to their high strength and hardness combination. This feature is especially useful for parts like cutting tools, bearings, and wear-resistant coatings that are subjected to mechanical wear. Certain composites based on HEA exhibit superior resistance to corrosion, rendering them appropriate for application in abrasive situations where exposure to caustic materials is a cause for worry. Their prospective uses in sectors including chemical processing, aircraft, and maritime are increased by this attribute. By changing the composition of its constituent parts, composites based on HEAs provide the freedom to customize their qualities. Because of this tunability, scientists and engineers may create materials that precisely combine mechanical, thermal, and chemical properties to satisfy the demands of a wide range of applications. When compared to traditional alloys, HEA-based composites frequently show improved thermal stability, which enables them to maintain their mechanical characteristics at high temperatures. Because of this characteristic, they can be used in high-temperature applications such as gas turbines, thermal barrier coatings, and aerospace components. Certain HEA-based composites are appealing for applications where weight reduction is crucial, such as the automotive and aerospace sectors, because they have comparatively lower densities than conventional high-strength materials like steel. The superior properties of HEA-MMC materials open up a variety of applications in the field of advanced structural materials, biomedical implants, and electronic devices.

High-entropy alloys, or HEAs, are materials with nearly equal proportions of several principal elements, which give them special qualities like high strength, superior resistance to corrosion, and good thermal stability. HEAs present a promising way to improve mechanical, thermal, and functional properties when incorporated into composite materials as reinforcements. However, their integration into composite materials comes with several challenges and promising perspectives.

**Challenges:** The most challenging is the processing technique to fabricate composite for HEA-MMCs due to their complex composition and constituent elements' high melting point. Adding HEAs into the matrix requires appropriate methods and knowledge of parameters for uniform dispersion of particles in composites. The reinforcement phase and HEA matrix must form a strong interfacial bond to maximize load transfer and improve mechanical properties. To enhance interfacial bonding, techniques like surface modification, interlayer materials, and in-situ synthesis can be investigated. To obtain desired properties like high strength, toughness, and thermal stability, one challenge is to optimize the composition of the reinforcing phase and the HEA matrix. Careful selection of alloying elements and a thorough understanding of the interactions between the reinforcement and matrix are necessary for this. HEA-based composites may face particular challenges depending on the application. For instance, lightweight, high-temperature-resistant materials might be needed for aerospace applications, but corrosion resistance and energy absorption qualities might be more important for automotive applications. Cost-effectiveness and scalability are major obstacles to the

industrial manufacture of composites based on HEA. Commercial viability depends on creating economical synthesis routes, maximizing processing parameters, and reducing material waste. To assess the microstructure, mechanical characteristics, and performance of HEA-based composites under various circumstances, thorough characterization techniques are needed. Understanding structure-property relationships requires advanced characterization techniques like X-ray diffraction, mechanical testing, and electron microscopy.

**Perspectives:** HEA-based composites can be designed to possess multiple functionalities, including shape memory, electrical conductivity, and self-healing, by integrating suitable reinforcement phases and managing microstructural characteristics. These multipurpose materials can be used in a variety of industries, including electronics, healthcare, and energy storage. HEA-based composites provide the ability to modify the composition, processing parameters, and types of reinforcement, thereby customizing properties like strength, ductility, thermal conductivity, and corrosion resistance. This adaptability creates chances for numerous applications in various industries. The development of sustainable manufacturing processes, encompassing recycling and waste reduction strategies, for HEA-based composites can aid in mitigating environmental impact and advancing the principles of the circular economy. Advanced applications in harsh environments, like aerospace, energy, and defence, where high performance under difficult conditions is needed, show promise for HEA-based composites. It is anticipated that more innovation and research will open up new opportunities in these fields. Because computational modelling and simulation can predict the microstructural evolution, mechanical behaviour, and performance of HEA-based composites under various loading conditions, they are essential tools for accelerating the development of these materials. This makes it possible to optimise composite designs and explore composition, processing, and property relationships efficiently. HEAs with a lot of non-toxic, readily available elements can help create environmentally friendly material solutions. HEA-based composites provide a viable route towards more environmentally friendly and sustainable material technologies by substituting rare or harmful elements with more widely available and sustainable substitutes.

## 8. Future scope

This review article describes a brief historical development in high entropy alloy reinforced metal matrix composites through various fabrication methods. The literature shows that the researchers are exploring the metal matrix composite reinforced with high entropy alloy. Mechanical properties and microstructural evaluation are areas to focus more on different aspects of HEA-reinforced MMCs. Based on the study performed following future scope can be developed in the direction of HEAs-MMCs.

- From the review, it comes to know that in solid-state manufacturing of HEA-MMCs, fabrication through the hybrid microwave sintering process is much less reported as compared to other processes. Therefore, research can be focused on developing HEA-reinforced MMC materials developed by a hybrid microwave sintering powder metallurgy process.

- Integration of HEAs and MMCs into advanced manufacturing processes like additive manufacturing processes can enable the creation of complex geometries and tailored structures with improved performance and reduced material waste.
- Most of the researchers used micro-sized reinforcement HEAs in different MMCs. However, very little work has been reported with nano-sized reinforced HEAp to fabricate nanocomposite material. Future work can be explored if continued development and research work done in the field of nanocomposite for high strength, toughness, and fatigue resistance. Tailoring composition and microstructure at the nanoscale could unlock new levels of performance.
- HEAs and MMCs can be engineered to exhibit unique functional properties beyond traditional metals. The research studies have shown that very few studies have been done for the aluminum 7xxx series applicable to aerospace applications.
- Applications in harsh environments, like high temperatures, corrosive environments, or radiation exposure, show promise for these materials. The nuclear, space exploration, aerospace, and energy sectors might employ them. It is possible to create biocompatible HEAs and MMCs for use in surgical instruments, prosthetics, and medical implants. They are the best options for long-lasting implants due to their exceptional strength and resistance to corrosion. Corrosion resistance observations are rarely reported by researchers, little work has been done and studies need to be conducted more.
- HEAs and MMCs can be developed into smart materials for wearable technology, aerospace sensors, and structural health monitoring by adding sensing elements or responsive phases. Wear performance and analysis are critical areas for the rubbing action and life of the material, and very little work has been found in this field for HEA-reinforced MMC.
- Thermal and electrical properties were evaluated only for the Cu matrix reinforced by HEAp, which is rarely reported. The properties of the aluminum matrix have not yet been examined by researchers.
- Only a few studies have been found on special HEAs regarding heat treatment, however, there is no literature exploring HEA-reinforced MM. Almost no studies have been found on the microstructure and mechanical properties of HEA-reinforced MMC and recrystallization after heat treatment.
- The strengthening mechanisms for improvement of matrix behavior by adding reinforcement are not much evaluated by different authors for HEA-reinforced MMCs.

## 9. Conclusions

The various HEA-MMC fabrication techniques were studied. Additional effects of HEA on metal matrix properties such as hardness, strength, wear, and corrosion are seen in research articles through hardness tests, tensile and compression tests, pin-on-disk wear tests, and 3.5 % NaCl corrosion tests. Variations in microstructure are examined by microscopic tests such as optical microscope (OM), scanning electron

microscope (SEM), energy-dispersive spectroscopy (EDS), and X-ray diffraction (XRD) tests. Thermal and electrical properties of HEA-MMCs are reviewed. Heat treatment and strengthening procedures are explored in sections of this review article.

- Many researchers use several powder metallurgy processes in all the manufacturing methods of HEA-MMCs, but ultrasonic probe-assisted stir casting is an improved technique over mechanical stir casting in liquid-state processing. Metal additive manufacturing (AM) processes are also being explored to create HEA-MMCs where laser powder bed fusion AM is widely used.
- Microstructures of HEA-MMCs are correlated with the properties of materials. It is interesting to note that core-shell structure is only observed in HEA-MMCs which are fabricated by the SPS method or treated with heat treatment process. Distribution of HEA particles along with the diffusion layer with matrix are the key factors for improvement in mechanical properties.
- As confirmed by the studies HEAs improve mechanical, physical, chemical, and other properties in various metal matrix composites. However in mechanical properties, only microhardness, tensile, and compression tests have been reported, and no studies have been made on bending tests, fatigue tests, fracture tests, and surface roughness tests in the physical aspect.
- The corrosion performance of the matrix material was improved by introducing HEA reinforcement. The matrix shows more pitting corrosion compared to the reinforcement. The improvement in corrosion resistance is due to HEA, which forms an oxide layer on the matrix and reduces the vol% of the matrix.
- The incorporation of HEAs in the matrix enhances the tribological properties of the matrix material due to the presence of hard and high wear resistance elements of HEAs. The diffusion layer and bonding of elements with the matrix are the mechanisms for high-performing material development. However actual fabrication of components and testing in real-time conditions is a future research direction in this field.
- The thermal properties of HEA-Cu composite do not deteriorate after using HEA compared to ceramic reinforcement due to the low imbalance of CTE value. Both the thermal diffusion coefficient and thermal conductivity of the HEA-Cu alloy improved after annealing compared to pure copper and the unannealed composite material.
- The electrical conductivity of HEA-Cu decreases while the strength and hardness increase with the addition of HEA wt% in the composite.
- The study of change in thermal and electrical properties of the material due to the presence of HEAs has just started on copper only. But in high-temperature applications such as the aerospace field, it has too many possibilities to explore.
- Heat treatment is a fruitful phenomenon to enhance the mechanical properties of HEA-MMC after the fabrication of MMC. The diffusion layer developed between the matrix and reinforcement phases influences improving the stiffness and strength of HEA-MMCs.

- Strengthening mechanisms are available to identify the mechanism for enhanced performance of HEA-MMC. Fine grain strengthening, Orowan strengthening, and Coefficient of thermal expansion (CTE) mismatch strengthening are the most convincing strengthening mechanisms of HEA-MMCs.
- The strengthening mechanism is the concept for the in-depth research study of HEA-MMC composites. However, the complete study of all strengthening mechanisms of any HEAs separately and with composite are not identified by researchers, which will be helpful to new research learners.

**Acknowledgment:** The authors would like to thank the Department of Science and Technology-Science and Engineering Research Board (DST-SERB), New Delhi, India, for supporting this work under the Empowerment and Equity Opportunities for Excellence in Science Scheme (File No. EEQ/2021/000047).

## References:

- [1] M. Radetzki, Seven thousand years in the service of humanity-the history of copper, the red metal, Resour. Policy 34 (2009) 176–184. <https://doi.org/10.1016/j.resourpol.2009.03.003>.
- [2] J.M. Torralba, P. Alvaredo, A. García-junceda, High-entropy alloys fabricated via powder metallurgy . A critical review, Powder Metall. 0 (2019) 1–31. <https://doi.org/10.1080/00325899.2019.1584454>.
- [3] J.W. Yeh, S.K. Chen, S.J. Lin, J.Y. Gan, T.S. Chin, T.T. Shun, C.H. Tsau, S.Y. Chang, Nanostructured high-entropy alloys with multiple principal elements: Novel alloy design concepts and outcomes, Adv. Eng. Mater. 6 (2004) 299–303. <https://doi.org/10.1002/adem.200300567>.
- [4] Y. Zhang, T.T. Zuo, Z. Tang, M.C. Gao, K.A. Dahmen, P.K. Liaw, Z.P. Lu, Microstructures and properties of high-entropy alloys, Prog. Mater. Sci. 61 (2014) 1–93. <https://doi.org/10.1016/j.pmatsci.2013.10.001>.
- [5] Y.Y. Chen, T. Duval, U.D. Hung, J.W. Yeh, H.C. Shih, Microstructure and electrochemical properties of high entropy alloys-a comparison with type-304 stainless steel, Corros. Sci. 47 (2005) 2257–2279. <https://doi.org/10.1016/j.corsci.2004.11.008>.
- [6] Z. Tang, T. Yuan, C.W. Tsai, J.W. Yeh, C.D. Lundin, P.K. Liaw, Fatigue behavior of a wrought Al0.5CoCrCuFeNi two-phase high-entropy alloy, Acta Mater. 99 (2015) 247–258. <https://doi.org/10.1016/j.actamat.2015.07.004>.
- [7] B. Gludovatz, A. Hohenwarter, D. Catoor, E.H. Chang, E.P. George, R.O. Ritchie, A fracture-resistant high-entropy alloy for cryogenic applications, Science (80-. ). 345 (2014) 1153–1158. <https://doi.org/10.1126/science.1254581>.
- [8] C. Hsu, J. Yeh, S. Chen, T. Shun, Wear resistance and high-temperature compression strength of Fcc CuCoNiCrAl, Metall. Mater. Trans. A, Phys. Metall. Mater. Sci. 35 (2004) 1465–1469.
- [9] B. Cantor, I.T.H. Chang, P. Knight, A.J.B. Vincent, Microstructural development in equiatomic multicomponent alloys, Mater. Sci. Eng. A 375–377 (2004) 213–218. <https://doi.org/10.1016/j.msea.2003.10.257>.

- [10] S. Ranganathan, Alloyed pleasures : Multimetallic cocktails, 85 (2003) 10–12.
- [11] N. Kaushik, A. Meena, High entropy alloy synthesis , characterisation , manufacturing & potential applications : a review, Mater. Manuf. Process. 00 (2021) 1–25. <https://doi.org/10.1080/10426914.2021.2006223>.
- [12] A. Kumar, M. Gupta, An Insight into Evolution of Light Weight High Entropy Alloys : A Review, Metals (Basel). (2016). <https://doi.org/10.3390/met6090199>.
- [13] E.J. Pickering, N.G. Jones, High-entropy alloys: a critical assessment of their founding principles and future prospects, Int. Mater. Rev. 6608 (2016). <https://doi.org/10.1080/09506608.2016.1180020>.
- [14] M. Tsai, J. Yeh, High-Entropy Alloys: A Critical Review, Mater. Res. Lett. 3831 (2014). <https://doi.org/10.1080/21663831.2014.912690>.
- [15] M. Tsai, Physical Properties of High Entropy Alloys, Entropy (2013) 5338–5345. <https://doi.org/10.3390/e15125338>.
- [16] N.D. Stepanov, D.G. Shaysultanov, R.S. Chernichenko, D.M. Ikornikov, V.N. Sanin, S. V. Zhrebtssov, Mechanical properties of a new high entropy alloy with a duplex ultra-fine grained structure, Mater. Sci. Eng. A 728 (2018) 54–62. <https://doi.org/10.1016/j.msea.2018.04.118>.
- [17] S.J. Sun, Y.Z. Tian, H.R. Lin, S. Lu, H.J. Yang, Z.F. Zhang, Modulating the prestrain history to optimize strength and ductility in CoCrFeMnNi high-entropy alloy, 163 (2019) 111–115. <https://doi.org/10.1016/j.scriptamat.2019.01.012>.
- [18] Y.F. Kao, T.J. Chen, S.K. Chen, J.W. Yeh, Microstructure and mechanical property of as-cast, -homogenized, and -deformed Al<sub>x</sub>CoCrFeNi (0 ≤ x ≤ 2) high-entropy alloys, J. Alloys Compd. 488 (2009) 57–64. <https://doi.org/10.1016/j.jallcom.2009.08.090>.
- [19] B.S. Murty, J.W. Yeh, S. Ranganathan, P.P. Bhattacharjee, High-entropy alloys., 2019.
- [20] M.C. Gao, J. Qiao, High-entropy alloys (Heas), Metals (Basel). 8 (2018). <https://doi.org/10.3390/met8020108>.
- [21] D. Kim, S. Surendran, Y. Jeong, Y. Lim, S. Im, S. Park, J.Y. Kim, S. Kim, T. Kim, B. Koo, K. Jin, U. Sim, Electrosynthesis of Low Pt-Loaded High Entropy Catalysts for Effective Hydrogen Evolution with Improved Acidic Durability, Adv. Mater. Technol. 2200882 (2023) 1–8. <https://doi.org/10.1002/admt.202200882>.
- [22] S. Im, D. Kim, S. Surendran, J. Choi, D.J. Moon, J.Y. Kim, H. Lee, D. Nam, U. Sim, High entropy alloy : From theoretical evaluation to electrocatalytic activity of hydrogen evolution reaction, Curr. Opin. Electrochem. 39 (2023) 101293. <https://doi.org/10.1016/j.coelec.2023.101293>.
- [23] T. Dippong, E. Levei, D. Toloman, L. Barbu-tudoran, O. Cadar, Investigation on the formation , structural and photocatalytic properties of mixed Mn-Zn ferrites nanoparticles embedded in SiO<sub>2</sub> matrix, J. Anal. Appl. Pyrolysis 158 (2021) 105281. <https://doi.org/10.1016/j.jaap.2021.105281>.
- [24] T. Dippong, E.A. Levei, F. Goga, O. Cadar, Influence of Mn<sup>2+</sup> substitution with Co<sup>2+</sup> on structural, morphological and coloristic properties of MnFe<sub>2</sub>O<sub>4</sub>/SiO<sub>2</sub> nanocomposites, Mater. Charact. (2020) 110835. <https://doi.org/10.1016/j.matchar.2020.110835>.

- [25] T. Dippong, E.A. Levei, I.G. Deac, I. Petean, G. Borodi, O. Cadar, Sol-Gel Synthesis , Structure , Morphology and Magnetic Properties of Ni<sub>0.6</sub>Mn<sub>0.4</sub>Fe<sub>2</sub>O<sub>4</sub> Nanoparticles Embedded in SiO<sub>2</sub> Matrix, *Nanomaterials* (2021) 1–15.
- [26] T. Dippong, D. Toloman, M. Dan, E. Andrea, O. Cadar, Structural, morphological and photocatalytic properties of Ni-Mn ferrites : Influence of the Ni : Mn ratio, *J. Alloys Compd.* 913 (2022) 1–9. <https://doi.org/10.1016/j.jallcom.2022.165129>.
- [27] C. Mn, O. Fe, T. Dippong, E. Andrea, C. Leostean, O. Cadar, Impact of annealing temperature and ferrite content embedded in SiO<sub>2</sub> matrix on the structure, morphology and magnetic characteristics of (Co<sub>0.4</sub>Mn<sub>0.6</sub>Fe<sub>2</sub>O<sub>4</sub>)<sub>δ</sub> (SiO<sub>2</sub>)<sub>100-δ</sub> nanocomposites, *J. Alloys Compd.* 868 (2021) 159203. <https://doi.org/10.1016/j.jallcom.2021.159203>.
- [28] M. Stoia, M. Stefanescu, P. Barvinschi, Low temperature synthesis of Co<sub>2</sub>SiO<sub>4</sub>/SiO<sub>2</sub> nanocomposite using a modified sol-gel method, *J. Sol-Gel Sci. Technol.* (2010) 49–56. <https://doi.org/10.1007/s10971-010-2156-2>.
- [29] T. Dippong, M. Stoia, STUDY ON THE OBTAINING OF COBALT OXIDES BY THERMAL DECOMPOSITION OF SOME COMPLEX COMBINATIONS , UNDIS- PERSED AND DISPERSED IN SiO<sub>2</sub> MATRIX, *J. Therm. Anal. Calorim.* 94 (2008) 389–393.
- [30] H. Wang, W. Ren, G. Li, H. Wen, C. Wang, J. Chen, Y. Zhao, G. Chen, X. Kai, Microstructure and properties of FeCoNi1.5CrCu/2024Al composites prepared by microwave sintering, *Mater. Sci. Eng. A* 801 (2021). <https://doi.org/10.1016/j.msea.2020.140406>.
- [31] J. Chen, P. Niu, T. Wei, L. Hao, Y. Liu, X. Wang, Y. Peng, Fabrication and mechanical properties of AlCoNiCrFe high-entropy alloy particle reinforced Cu matrix composites, *J. Alloys Compd.* 649 (2015) 630–634. <https://doi.org/10.1016/j.jallcom.2015.07.125>.
- [32] R.K. Prabakaran, A.N. Sait, V. Senthilkumar, Synthesis and characterization of high entropy alloy (CrMnFeNiCu) reinforced AA6061 aluminium matrix composite, *Mech. Mech. Eng.* 21 (2017) 415–424.
- [33] E. Ananiadis, K.T. Argyris, T.E. Matikas, A.K. Sfikas, A.E. Karantzalis, Microstructure and corrosion performance of aluminium matrix composites reinforced with refractory high-entropy alloy particulates, *Appl. Sci.* 11 (2021) 1–12. <https://doi.org/10.3390/app11031300>.
- [34] M.S. Venkatesh, G.S.V. Raghavan, An overview of microwave processing and dielectric properties of agri-food materials, *Biosyst. Eng.* 88 (2004) 1–18. <https://doi.org/10.1016/j.biosystemseng.2004.01.007>.
- [35] S.A.A. Alem, R. Latifi, S. Angizi, F. Hassanaghaei, M. Aghaahmadi, E. Ghasali, M. Rajabi, Microwave sintering of ceramic reinforced metal matrix composites and their properties: a review, *Mater. Manuf. Process.* 35 (2020) 303–327. <https://doi.org/10.1080/10426914.2020.1718698>.
- [36] Y. Makino, T. Ohmae, Y. Setsuhara, S. Miyake, S. Sano, Sintering of Al<sub>2</sub>O<sub>3</sub>-ZrO<sub>2</sub> Composites Using Millimeter-Wave Radiation, *Key Eng. Mater.* 161–163 (1998) 41–44. <https://doi.org/10.4028/www.scientific.net/kem.161-163.41>.

- [37] D. Agrawal, Microwave sintering of ceramics, composites and metallic materials, and melting of glasses, *Trans. Indian Ceram. Soc.* 65 (2006) 129–144. <https://doi.org/10.1080/0371750X.2006.11012292>.
- [38] R.R. Mishra, S. Rajesha, A.K. Sharma, Microwave Sintering of Pure Metal Powders – A Review, 4 (2014) 315–322.
- [39] L. Zong, S. Zhou, N. Sgriccia, M.C. Hawley, L.C. Kempel, A Review of Microwave-Assisted Polymer Chemistry (MAPC), *J. Microw. Power Electromagn. Energy* 38 (2003) 49–74. <https://doi.org/10.1080/08327823.2003.11688487>.
- [40] S. Vongpradubchai, P. Rattanadecho, The microwave processing of wood using a continuous microwave belt drier, *Chem. Eng. Process. Process Intensif.* 48 (2009) 997–1003. <https://doi.org/10.1016/j.cep.2009.01.008>.
- [41] M. Oghbaei, O. Mirzaee, Microwave versus conventional sintering: A review of fundamentals, advantages and applications, *J. Alloys Compd.* 494 (2010) 175–189. <https://doi.org/10.1016/j.jallcom.2010.01.068>.
- [42] V.S.S. Venkatesh, Microstructure and mechanical properties comparison between spark plasma sintered and microwave sintered Al-(SiC + B<sub>4</sub>C) composite, *Mater. Lett.* 366 (2024) 136496. <https://doi.org/10.1016/j.matlet.2024.136496>.
- [43] N.K. Bhoi, H. Singh, S. Pratap, P.K. Jain, Microwave material processing: A clean, green, and sustainable approach, Elsevier Inc., 2019. <https://doi.org/10.1016/B978-0-12-816564-5.00001-3>.
- [44] R.R. Mishra, A.K. Sharma, Structure-property correlation in Al–Zn–Mg alloy cast developed through in-situ microwave casting, *Mater. Sci. Eng. A* 688 (2017) 532–544. <https://doi.org/10.1016/j.msea.2017.02.021>.
- [45] R.R. Mishra, A.K. Sharma, A Review of Research Trends in Microwave Processing of Metal-Based Materials and Opportunities in Microwave Metal Casting, *Crit. Rev. Solid State Mater. Sci.* 41 (2016) 217–255. <https://doi.org/10.1080/10408436.2016.1142421>.
- [46] R. Roy, D. Agrawal, J. Cheng, S. Gedevanishvili, Full sintering of powdered-metal bodies, *Nature* 399 (1999) 668–670.
- [47] S. Sharma, S.R. Parne, S. Srihari, S. Panda, S. Gandi, Progress in microwave absorbing materials : A critical review, *Adv. Colloid Interface Sci.* 327 (2024) 103143. <https://doi.org/10.1016/j.cis.2024.103143>.
- [48] N. V. Abhijith, S. Phutela, D. Kumar, D. Kalyanasundaram, Transitional and refractory elements-based high entropy alloy developed through mechanical alloying and microwave sintering: Tribological and corrosion responses, *Vacuum* 222 (2024) 113061. <https://doi.org/10.1016/j.vacuum.2024.113061>.
- [49] P. Cavaliere, B. Sadeghi, A. Shabani, Spark plasma sintering: Process fundamentals, *Spark Plasma Sinter. Mater. Adv. Process. Appl.* (2019) 3–20. <https://doi.org/10.1007/978-3-030-05327-7>.
- [50] N. Saheb, Z. Iqbal, A. Khalil, A.S. Hakeem, N. Al Aqeeli, T. Laoui, A. Al-Qutub, R. Kirchner, Spark

- plasma sintering of metals and metal matrix nanocomposites: A review, *J. Nanomater.* 2012 (2012). <https://doi.org/10.1155/2012/983470>.
- [51] X. Yang, P. Dong, Z. Yan, B. Cheng, X. Zhai, H. Chen, H. Zhang, W. Wang, AlCoCrFeNi high-entropy alloy particle reinforced 5083Al matrix composites with fine grain structure fabricated by submerged friction stir processing, *J. Alloys Compd.* 836 (2020) 155411. <https://doi.org/10.1016/j.jallcom.2020.155411>.
- [52] Z. Li, Y. Zhang, H. Xiong, C. Kong, H. Yu, Fabrication of particle-reinforced aluminum alloy composite: role of casting and rolling, *Mater. Manuf. Process.* 37 (2022) 90–98. <https://doi.org/10.1080/10426914.2021.1944198>.
- [53] K. Luo, H. Xiong, Y. Zhang, H. Gu, Z. Li, C. Kong, H. Yu, AA1050 metal matrix composites reinforced by high-entropy alloy particles via stir casting and subsequent rolling, *J. Alloys Compd.* 893 (2022) 162370. <https://doi.org/10.1016/j.jallcom.2021.162370>.
- [54] Y. Zhang, X. Li, H. Gu, R. Li, P. Chen, C. Kong, H. Yu, Insight of high-entropy alloy particles-reinforced 2219 Al matrix composites via the ultrasonic casting technology, *Mater. Charact.* 182 (2021) 111548. <https://doi.org/10.1016/j.matchar.2021.111548>.
- [55] Y. Zhang, G. Lei, K. Luo, P. Chen, C. Kong, H. Yu, Tribological behavior of high-entropy alloy particle reinforced aluminum matrix composites and their key impacting factors, *Tribol. Int.* 175 (2022) 107868. <https://doi.org/10.1016/j.triboint.2022.107868>.
- [56] J.K. Tiwari, A. Mandal, N. Sathish, A.K. Agrawal, A.K. Srivastava, Investigation of porosity, microstructure and mechanical properties of additively manufactured graphene reinforced AlSi10Mg composite, *Addit. Manuf.* 33 (2020) 101095. <https://doi.org/10.1016/j.addma.2020.101095>.
- [57] J.K. Tiwari, A. Mandal, N. Sathish, S. Kumar, M. Ashiq, M. Nagini, R.K. Sharma, A.K. Agrawal, P. Rajput, A.K. Srivastava, Effect of graphene addition on thermal behavior of 3D printed graphene/AlSi10Mg composite, *J. Alloys Compd.* 890 (2022) 161725. <https://doi.org/10.1016/j.jallcom.2021.161725>.
- [58] A. Mandal, J.K. Tiwari, B. AlMangour, N. Sathish, S. Kumar, M. Kamaraj, M. Ashiq, A.K. Srivastava, Tribological behavior of graphene-reinforced 316L stainless-steel composite prepared via selective laser melting, *Tribol. Int.* 151 (2020) 106525. <https://doi.org/10.1016/j.triboint.2020.106525>.
- [59] Y.T. Ang, S.L. Sing, J.C.W. Lim, Process study for directed energy deposition of 316L stainless steel with TiB<sub>2</sub> metal matrix composites, *Mater. Sci. Addit. Manuf.* 1 (2022) 13. <https://doi.org/10.18063/msam.v1i2.13>.
- [60] J. Karimi, P. Ma, Y.D. Jia, K.G. Prashanth, Linear patterning of high entropy alloy by additive manufacturing, *Manuf. Lett.* 24 (2020) 9–13. <https://doi.org/10.1016/j.mfglet.2020.03.003>.
- [61] Z.U. Arif, M.Y. Khalid, E. ur Rehman, Laser-aided additive manufacturing of high entropy alloys: Processes, properties, and emerging applications, *J. Manuf. Process.* 78 (2022) 131–171. <https://doi.org/10.1016/j.jmapro.2022.04.014>.

- [62] Z. Xu, H. Zhang, X. Du, Y. He, H. Luo, G. Song, Corrosion resistance enhancement of CoCrFeMnNi high-entropy alloy fabricated by additive manufacturing, *Corros. Sci.* 177 (2020) 108954. <https://doi.org/10.1016/j.corsci.2020.108954>.
- [63] S. Chen, Y. Tong, P.K. Liaw, Additive Manufacturing of High-Entropy Alloys : A Review, *Entropy* (2018). <https://doi.org/10.3390/e20120937>.
- [64] K. Zhou, Z. Wang, F. He, S. Liu, J. Li, J. Kai, J. Wang, A precipitation-strengthened high-entropy alloy for additive manufacturing, *Addit. Manuf.* 35 (2020) 101410. <https://doi.org/10.1016/j.addma.2020.101410>.
- [65] J. He, Y. Qiao, R. Wang, Y. Tang, S. Li, X. Liu, Y. Ye, L. Zhu, Z. Wang, S. Bai, State and effect of oxygen on high entropy alloys prepared by powder metallurgy, *J. Alloys Compd.* 891 (2021) 161963. <https://doi.org/10.1016/j.jallcom.2021.161963>.
- [66] P. Xie, M. Yin, Y. Zhao, Y. Liu, Y. Qi, X. Li, C. Li, G. Wu, Removal of covered metallic stents with a bullet head for bronchopleural fistula using a fluoroscopy-assisted interventional technique, *Clin. Radiol.* (2020) 1–6. <https://doi.org/10.1016/j.crad.2020.07.034>.
- [67] M. Tekin, G. Polat, Y.E. Kalay, H. Kotan, Grain size stabilization of oxide dispersion strengthened CoCrFeNi-Y<sub>2</sub>O<sub>3</sub> high entropy alloys synthesized by mechanical alloying, *J. Alloys Compd.* 887 (2021) 161363. <https://doi.org/10.1016/j.jallcom.2021.161363>.
- [68] G.M. Karthik, S. Panikar, G.D.J. Ram, R.S. Kottada, Additive manufacturing of an aluminum matrix composite reinforced with nanocrystalline high-entropy alloy particles, *Mater. Sci. Eng. A* 679 (2017) 193–203. <https://doi.org/10.1016/j.msea.2016.10.038>.
- [69] J. Li, S. Xiang, H. Luan, A. Amar, X. Liu, S. Lu, Y. Zeng, G. Le, X. Wang, F. Qu, C. Jiang, G. Yang, Additive manufacturing of high-strength CrMnFeCoNi high-entropy alloys-based composites with WC addition, *J. Mater. Sci. Technol.* 35 (2019) 2430–2434. <https://doi.org/10.1016/j.jmst.2019.05.062>.
- [70] S. Riva, A. Tudball, S. Mehraban, N.P. Lavery, S.G.R. Brown, K. V Yusenko, A novel High-Entropy Alloy-based composite material, *J. Alloys Compd.* 730 (2018) 544–551. <https://doi.org/10.1016/j.jallcom.2017.09.274>.
- [71] X. Li, Additive Manufacturing of Advanced Multi-Component Alloys : Bulk Metallic Glasses and High Entropy Alloys, *Adv. Eng. Mater.* 1700874 (2017) 1–18. <https://doi.org/10.1002/adem.201700874>.
- [72] D. Svetlizky, B. Zheng, A. Vyatskikh, M. Das, S. Bose, A. Bandyopadhyay, J.M. Schoenung, E.J. Lavernia, N. Eliaz, A Laser-based directed energy deposition ( DED-LB ) of advanced materials, *Mater. Sci. Eng. A* 840 (2022) 142967. <https://doi.org/10.1016/j.msea.2022.142967>.
- [73] D. Shim, G. Baek, J. Seo, G. Shin, K. Kim, K. Lee, Effect of layer thickness setting on deposition characteristics in direct energy deposition ( DED ) process, *Opt. Laser Technol.* 86 (2016) 69–78. <https://doi.org/10.1016/j.optlastec.2016.07.001>.
- [74] M. Schmidt, M. Merklein, D. Bourell, D. Dimitrov, T. Hausotte, K. Wegener, L. Overmeyer, F.

- Vollertsen, G.N. Levy, Laser based additive manufacturing in industry and academia, CIRP Ann. 66 (2017) 561–583. <https://doi.org/10.1016/j.cirp.2017.05.011>.
- [75] N. Guo, M.C. Leu, Additive manufacturing: Technology, applications and research needs, *Front. Mech. Eng.* 8 (2013) 215–243. <https://doi.org/10.1007/s11465-013-0248-8>.
- [76] W.E. Frazier, Metal additive manufacturing: A review, *J. Mater. Eng. Perform.* 23 (2014) 1917–1928. <https://doi.org/10.1007/s11665-014-0958-z>.
- [77] M.K. Thompson, G. Moroni, T. Vaneker, G. Fadel, R.I. Campbell, I. Gibson, A. Bernard, J. Schulz, P. Graf, B. Ahuja, F. Martina, Design for Additive Manufacturing: Trends, opportunities, considerations, and constraints, *CIRP Ann. - Manuf. Technol.* 65 (2016) 737–760. <https://doi.org/10.1016/j.cirp.2016.05.004>.
- [78] W. Gao, Y. Zhang, D. Ramanujan, K. Ramani, Y. Chen, C.B. Williams, C.C.L. Wang, Y.C. Shin, S. Zhang, P.D. Zavattieri, The status, challenges, and future of additive manufacturing in engineering, *CAD Comput. Aided Des.* 69 (2015) 65–89. <https://doi.org/10.1016/j.cad.2015.04.001>.
- [79] D.G. Ahn, Direct metal additive manufacturing processes and their sustainable applications for green technology: A review, *Int. J. Precis. Eng. Manuf. - Green Technol.* 3 (2016) 381–395. <https://doi.org/10.1007/s40684-016-0048-9>.
- [80] D.G. Ahn, Applications of laser assisted metal rapid tooling process to manufacture of molding & forming tools - state of the art, *Int. J. Precis. Eng. Manuf.* 12 (2011) 925–938. <https://doi.org/10.1007/s12541-011-0125-5>.
- [81] D. Ding, Z. Pan, D. Cuiuri, H. Li, Wire-feed additive manufacturing of metal components: technologies, developments and future interests, *Int. J. Adv. Manuf. Technol.* 81 (2015) 465–481. <https://doi.org/10.1007/s00170-015-7077-3>.
- [82] W.J. Sames, F.A. List, S. Pannala, R.R. Dehoff, S.S. Babu, F.A. List, S. Pannala, R.R. Dehoff, S.S.B. The, W.J. Sames, F.A. List, S. Pannala, R.R. Dehoff, S.S. Babu, The metallurgy and processing science of metal additive manufacturing, *Int. Mater. Rev.* 6608 (2016). <https://doi.org/10.1080/09506608.2015.1116649>.
- [83] A. Dass, A. Moridi, State of the Art in Directed Energy Deposition : From, *Coatings* (2019). <https://doi.org/doi.org/10.3390/coatings9070418>.
- [84] A. Singh, S. Kapil, M. Das, A Comprehensive Review of the Methods and Mechanisms for Powder Feedstock Handling in Directed Energy Deposition, *Addit. Manuf.* (2020) 101388. <https://doi.org/10.1016/j.addma.2020.101388>.
- [85] S.L. Sing, W.Y. Yeong, Laser powder bed fusion for metal additive manufacturing : perspectives on recent developments, *Virtual Phys. Prototyp.* (2020) 359–370. <https://doi.org/10.1080/17452759.2020.1779999>.
- [86] J.P. Oliveira, A.D. Lalonde, J. Ma, Processing parameters in laser powder bed fusion metal additive manufacturing, *Mater. Des.* 193 (2020) 1–12. <https://doi.org/10.1016/j.matdes.2020.108762>.
- [87] F. Concli, A. Gilioli, Numerical and experimental assessment of the mechanical properties of 3D

- printed 18-Ni300 steel trabecular structures produced by Selective Laser Melting—a lean design approach, *Virtual Phys. Prototyp.* 14 (2019) 267–276. <https://doi.org/10.1080/17452759.2019.1565596>.
- [88] C. Zhang, J. Zhu, C. Ji, Y. Guo, R. Fang, S. Mei, S. Liu, Laser powder bed fusion of high-entropy alloy particle-reinforced stainless steel with enhanced strength, ductility and corrosion resistance, *Mater. Des.* 209 (2021) 109950. <https://doi.org/10.1016/j.matdes.2021.109950>.
- [89] A. Poulia, E. Georgatis, A. Lekatou, A. Karantzalis, Dry-Sliding Wear Response of MoTaWNbV High Entropy Alloy, *Adv. Eng. Mater.* 19 (2017) 1–10. <https://doi.org/10.1002/adem.201600535>.
- [90] L. Zhang, R. Li, R. Jiang, L. Zhang, X. Li, A Comparative Study on the Effect of Four-Source Ultrasonic Power on the Microstructure and Mechanical Properties of Large-Scale 2219 Aluminum Ingots, *Jom* 71 (2019) 2063–2071. <https://doi.org/10.1007/s11837-019-03459-y>.
- [91] Z. Yuan, W. Tian, F. Li, Q. Fu, Y. Hu, X. Wang, Microstructure and properties of high-entropy alloy reinforced aluminum matrix composites by spark plasma sintering, *J. Alloys Compd.* 806 (2019) 901–908. <https://doi.org/10.1016/j.jallcom.2019.07.185>.
- [92] Z. Tan, L. Wang, Y. Xue, P. Zhang, T. Cao, X. Cheng, High-entropy alloy particle reinforced Al-based amorphous alloy composite with ultrahigh strength prepared by spark plasma sintering, *Mater. Des.* 109 (2016) 219–226. <https://doi.org/10.1016/j.matdes.2016.07.086>.
- [93] Y. Liu, J. Chen, Z. Li, X. Wang, X. Fan, J. Liu, Formation of transition layer and its effect on mechanical properties of AlCoCrFeNi high-entropy alloy/Al composites, *J. Alloys Compd.* 780 (2019) 558–564. <https://doi.org/10.1016/j.jallcom.2018.11.364>.
- [94] Z. Yuan, W. Tian, F. Li, Q. Fu, X. Wang, W. Qian, W. An, Effect of heat treatment on the interface of high-entropy alloy particles reinforced aluminum matrix composites, *J. Alloys Compd.* 822 (2020) 153658. <https://doi.org/10.1016/j.jallcom.2020.153658>.
- [95] Z. Yuan, H. Liu, Z. Ma, X. Ma, K. Wang, X. Zhang, Microstructure and properties of high entropy alloy reinforced titanium matrix composites, *Mater. Charact.* 187 (2022) 111856. <https://doi.org/10.1016/j.matchar.2022.111856>.
- [96] N. Wang, B. Wu, W. Wu, J. Li, C. Ge, Y. Dong, L. Zhang, Y. Wang, Microstructure and properties of aluminium-high entropy alloy composites fabricated by mechanical alloying and spark plasma sintering, *Mater. Today Commun.* 25 (2020). <https://doi.org/10.1016/j.mtcomm.2020.101366>.
- [97] D. Zhu, T. Chen, X. Jin, H. Wen, Z. Fu, S. Qu, Quasi-static and dynamic deformation of aluminum matrix composites reinforced by core-shell Al 35 Ti 15 Cu 10 Mn 20 Cr 20 high-entropy alloy particulates, *J. Mater. Res. Technol.* 30 (2024) 1009–1019. <https://doi.org/10.1016/j.jmrt.2024.03.119>.
- [98] P. Xiao, Q. Zhao, Y. Gao, H. Yang, W. Wu, Interface characteristics and tensile fracture behavior of CoCrFeNi / 6061Al matrix composites fabricated via spark plasma sintering and heat treatment, *Mater. Charact.* 208 (2024) 113685. <https://doi.org/10.1016/j.matchar.2024.113685>.
- [99] P. Li, Z. Wang, B. Zhu, Y. Zhang, B. Wu, Enhancing strength-ductility synergy of thermally oxidized

- dual-phase HEA particles reinforced aluminum matrix composites via heterogeneous interface, *J. Mater. Res. Technol.* 30 (2024) 3929–3940. <https://doi.org/10.1016/j.jmrt.2024.04.096>.
- [100] F. Zhang, Z. He, K. Lu, Z. Zhan, Z. Li, X. Wang, Interfacial microstructure and mechanical properties of 2124 aluminum alloy reinforced by AlCoCrFeNi high entropy alloy, *J. Mater. Res. Technol.* 26 (2023) 8846–8856. <https://doi.org/10.1016/j.jmrt.2023.09.184>.
- [101] S. Salifu, P. Apata, L. Teffo, Phase stability and microstructural properties of high entropy alloy reinforced aluminium matrix composites consolidated via spark plasma sintering, *Heliyon* 10 (2024) e24498. <https://doi.org/10.1016/j.heliyon.2024.e24498>.
- [102] K.G.P. P. V. Satyanarayana, R. Sokkalingam, P. K. Jena, K. Sivaprasad, Tungsten Matrix Composite Reinforced with CoCrFeMnNi High-Entropy Alloy : Impact of Processing Routes on Microstructure and Mechanical Properties, (2019) 1–12. <https://doi.org/https://doi.org/10.3390/met9090992>.
- [103] I. Moravcik, J. Cizek, L.D.A. Gouvea, J. Cupera, I. Guban, Nitrogen Interstitial Alloying of CoCrFeMnNi High Entropy Alloy through Reactive Powder Milling, (2019) 1–7. <https://doi.org/10.3390/e21040363>.
- [104] K.S. Tun, M. Gupta, Enhanced mechanical properties and near unity yield asymmetry in equiatomic high entropy alloy particles reinforced magnesium composites, *J. Alloys Compd.* 810 (2019) 151909. <https://doi.org/10.1016/j.jallcom.2019.151909>.
- [105] M.J. Shen, X.J. Wang, C.D. Li, M.F. Zhang, X.S. Hu, M.Y. Zheng, K. Wu, Effect of bimodal size SiC particulates on microstructure and mechanical properties of AZ31B magnesium matrix composites, *Mater. Des.* 52 (2013) 1011–1017. <https://doi.org/10.1016/j.matdes.2013.05.067>.
- [106] E.A. Ball, P.B. Prangnell, Tensile-compressive yield asymmetries in high strength wrought magnesium alloys, *Scr. Metall. Mater.* 31 (1994) 111–116. [https://doi.org/10.1016/0956-716X\(94\)90159-7](https://doi.org/10.1016/0956-716X(94)90159-7).
- [107] B. Inem, Dynamic recrystallization in a thermomechanically processed metal matrix composite, *Mater. Sci. Eng. A* 197 (1995) 91–95. [https://doi.org/10.1016/0921-5093\(94\)09753-4](https://doi.org/10.1016/0921-5093(94)09753-4).
- [108] J. Chen, T. Xiang, W. Bao, B. Yu, J. Li, Y. Wang, T. Zhou, P. Du, G. Xie, Novel strength-electrical conductivity synergy in Cu-based composites reinforced with TiZrNbTa high entropy alloy, *Mater. Sci. Eng. A* 878 (2023) 145210. <https://doi.org/10.1016/j.msea.2023.145210>.
- [109] C.S. Kim, K. Cho, M.H. Manjili, M. Nezafati, Mechanical performance of particulate-reinforced Al metal-matrix composites (MMCs) and Al metal-matrix nano-composites (MMNCs), *J. Mater. Sci.* 52 (2017) 13319–13349. <https://doi.org/10.1007/s10853-017-1378-x>.
- [110] X. Yang, H. Zhang, B. Cheng, Y. Liu, Z. Yan, P. Dong, W. Wang, Microstructural, Microhardness and tribological analysis of cooling-assisted friction stir processing of high-entropy alloy particles reinforced aluminum alloy surface composites, *Surf. Topogr. Metrol. Prop.* 8 (2020). <https://doi.org/10.1088/2051-672X/abade4>.
- [111] J. Gao, S. Zhang, H. Jin, Y. Shen, Fabrication of Al7075/PI composites base on FSW technology, *Int. J. Adv. Manuf. Technol.* 104 (2019) 4377–4386. <https://doi.org/10.1007/s00170-019-04235-7>.

- [112] I. Dinaharan, S. Zhang, G. Chen, Q. Shi, Titanium particulate reinforced AZ31 magnesium matrix composites with improved ductility prepared using friction stir processing, *Mater. Sci. Eng. A* 772 (2020) 138793. <https://doi.org/10.1016/j.msea.2019.138793>.
- [113] A. Heydarian, K. Dehghani, T. Slamkish, Optimizing powder distribution in production of surface nano-composite via friction stir processing, *Metall. Mater. Trans. B Process Metall. Mater. Process. Sci.* 45 (2014) 821–826. <https://doi.org/10.1007/s11663-014-0025-z>.
- [114] E.R.I. Mahmoud, K. Ikeuchi, M. Takahashi, Fabrication of SiC particle reinforced composite on aluminium surface by friction stir processing, *Sci. Technol. Weld. Join.* 13 (2008) 607–618. <https://doi.org/10.1179/136217108X333327>.
- [115] A. Poulia, E. Georgatis, A. Lekatou, A.E. Karantzalis, Microstructure and wear behavior of a refractory high entropy alloy, *Int. J. Refract. Met. Hard Mater.* 57 (2016) 50–63. <https://doi.org/10.1016/j.ijrmhm.2016.02.006>.
- [116] K.P. Kumar, M.G. Krishna, J.B. Rao, N.R.M.R. Bhargava, Fabrication and characterization of 2024 aluminium - high entropy alloy composites, *J. Alloys Compd.* (2024). <https://doi.org/10.1016/j.jallcom.2015.03.093>.
- [117] S. Cai, X. Ma, H. Tang, In situ WAl 12 particle-reinforced Al matrix composites synthesized by combining mechanical alloying and vacuum hot pressing technology, *J. Alloys Compd.* 520 (2012) 170–173. <https://doi.org/10.1016/j.jallcom.2011.12.168>.
- [118] Y. Lu, X. Gao, L. Jiang, Z. Chen, T. Wang, J. Jie, H. Kang, Y. Zhang, S. Guo, H. Ruan, Y. Zhao, Z. Cao, T. Li, Directly cast bulk eutectic and near-eutectic high entropy alloys with balanced strength and ductility in a wide temperature range, *Acta Mater.* 124 (2017) 143–150. <https://doi.org/10.1016/j.actamat.2016.11.016>.
- [119] Y. Lu, X. Gao, Y. Dong, T. Wang, H.L. Chen, H. Mao, Y. Zhao, H. Jiang, Z. Cao, T. Li, S. Guo, Preparing bulk ultrafine-microstructure high-entropy alloys: Via direct solidification, *Nanoscale* 10 (2018) 1912–1919. <https://doi.org/10.1039/c7nr07281c>.
- [120] S. Sankaranarayanan, V. Hemanth Shankar, S. Jayalakshmi, N. Quy Bau, M. Gupta, Development of high performance magnesium composites using Ni50Ti50metallic glass reinforcement and microwave sintering approach, *J. Alloys Compd.* 627 (2015) 192–199. <https://doi.org/10.1016/j.jallcom.2014.12.009>.
- [121] S. Scudino, G. Liu, K.G. Prashanth, B. Bartusch, K.B. Surreddi, B.S. Murty, J. Eckert, Mechanical properties of Al-based metal matrix composites reinforced with Zr-based glassy particles produced by powder metallurgy, *Acta Mater.* 57 (2009) 2029–2039. <https://doi.org/10.1016/j.actamat.2009.01.010>.
- [122] P. Yu, K.B. Kim, J. Das, F. Baier, W. Xu, J. Eckert, Fabrication and mechanical properties of Ni-Nb metallic glass particle-reinforced Al-based metal matrix composite, *Scr. Mater.* 54 (2006) 1445–1450. <https://doi.org/10.1016/j.scriptamat.2006.01.001>.
- [123] T. Lu, W. Chen, Z. Li, T. He, B. Li, R. Li, Z. Fu, S. Scudino, Processing and mechanical properties

of fine grained Al matrix composites reinforced with a uniform dispersion of nanocrystalline high-entropy alloy particles, *J. Alloys Compd.* 801 (2019) 473–477. <https://doi.org/10.1016/j.jallcom.2019.06.157>.

- [124] W. Chen, Z. Li, T. Lu, T. He, R. Li, B. Li, B. Wan, Z. Fu, S. Scudino, Effect of ball milling on microstructure and mechanical properties of 6061Al matrix composites reinforced with high-entropy alloy particles, *Mater. Sci. Eng. A* 762 (2019) 138116. <https://doi.org/10.1016/j.msea.2019.138116>.
- [125] X. Huang, J. Zhang, J. Miao, E. Cinkilic, Q. Wang, A.A. Luo, On the interactions between molten aluminum and high entropy alloy particles during aluminum matrix composite processing, *J. Alloys Compd.* 895 (2022) 162712. <https://doi.org/10.1016/j.jallcom.2021.162712>.
- [126] Q. Zhou, S. Sheikh, P. Ou, D. Chen, Q. Hu, S. Guo, Corrosion behavior of Hf0.5Nb0.5Ta0.5Ti1.5Zr refractory high-entropy in aqueous chloride solutions, *Electrochim. Commun.* 98 (2019) 63–68. <https://doi.org/10.1016/j.elecom.2018.11.009>.
- [127] V. Pandian, S. Kannan, Effect of high entropy particle on aerospace-grade aluminium composite developed through combined mechanical supersonic vibration and squeeze infiltration technique, *J. Manuf. Process.* 74 (2022) 383–399. <https://doi.org/10.1016/j.jmapro.2021.12.024>.
- [128] A. Zhang, J. Han, B. Su, P. Li, J. Meng, Microstructure, mechanical properties and tribological performance of CoCrFeNi high entropy alloy matrix self-lubricating composite, *Mater. Des.* 114 (2017) 253–263. <https://doi.org/10.1016/j.matdes.2016.11.072>.
- [129] Y.H. Çelik, K. Seçilmiş, Investigation of wear behaviours of Al matrix composites reinforced with different B4C rate produced by powder metallurgy method, *Adv. Powder Technol.* 28 (2017) 2218–2224. <https://doi.org/10.1016/j.apt.2017.06.002>.
- [130] A. Baradeswaran, A. Elaya Perumal, Influence of B4C on the tribological and mechanical properties of Al 7075-B4C composites, *Compos. Part B Eng.* 54 (2013) 146–152. <https://doi.org/10.1016/j.compositesb.2013.05.012>.
- [131] A. Manochehrian, A. Heidarpour, Y. Mazaheri, S. Ghasemi, On the surface reinforcing of A356 aluminum alloy by nanolayered Ti3AlC2 MAX phase via friction stir processing, *Surf. Coatings Technol.* 377 (2019) 124884. <https://doi.org/10.1016/j.surfcoat.2019.08.013>.
- [132] P.J. Mane, M. Shantharaja, B. Manne, B.S. Raju, Effect of FeCoNiMnCr High-Entropy Alloy Reinforcement on Mechanical, Wear, and Thermal Expansion Behavior of Copper Matrix Composites, *Jom* 75 (2023) 4421–4434. <https://doi.org/10.1007/s11837-023-06066-0>.
- [133] T. Schubert, B. Trindade, T. Weißgärber, B. Kieback, Interfacial design of Cu-based composites prepared by powder metallurgy for heat sink applications, *Mater. Sci. Eng. A* 475 (2008) 39–44. <https://doi.org/10.1016/j.msea.2006.12.146>.
- [134] M.R. Akbarpour, E. Salahi, F. Alikhani Hesari, H.S. Kim, A. Simchi, Effect of nanoparticle content on the microstructural and mechanical properties of nano-SiC dispersed bulk ultrafine-grained Cu matrix composites, *Mater. Des.* 52 (2013) 881–887. <https://doi.org/10.1016/j.matdes.2013.05.072>.
- [135] G. Laplanche, P. Gadaud, O. Horst, F. Otto, G. Eggeler, E.P. George, Temperature dependencies of

the elastic moduli and thermal expansion coefficient of an equiatomic, single-phase CoCrFeMnNi high-entropy alloy, J. Alloys Compd. 623 (2015) 348–353. <https://doi.org/10.1016/j.jallcom.2014.11.061>.

- [136] K. Dash, S. Sukumaran, B.C. Ray, The behaviour of aluminium matrix composites under thermal stresses, Sci. Eng. Compos. Mater. 23 (2016) 1–20. <https://doi.org/10.1515/secm-2013-0185>.
- [137] J. Zang, H. Li, J. Sun, Y. Shen, N. Su, X. Feng, Microstructure and thermal conductivity of Cu-Cu<sub>2</sub>AlNiZnAg/diamond coatings on pure copper substrate via high-energy mechanical alloying method, Surfaces and Interfaces 21 (2020) 100742. <https://doi.org/10.1016/j.surfin.2020.100742>.
- [138] C. Lu, X. Feng, Y. Shen, Y. Tian, J. Jiang, L. Hu, Wear resistance and thermal conductivity of diamond/Cu-1Cr mechanical milled coatings after high temperature annealing, Diam. Relat. Mater. 97 (2019) 107438. <https://doi.org/10.1016/j.diamond.2019.05.023>.
- [139] J.M. Park, J. Moon, J.W. Bae, J. Jung, S. Lee, H.S. Kim, Effect of annealing heat treatment on microstructural evolution and tensile behavior of Al0.5CoCrFeMnNi high-entropy alloy, Mater. Sci. Eng. A 728 (2018) 251–258. <https://doi.org/10.1016/j.msea.2018.05.041>.
- [140] A. Shabani, M.R. Toroghinejad, A. Shafyei, R.E. Logé, Evaluation of the mechanical properties of the heat treated FeCrCuMnNi high entropy alloy, Mater. Chem. Phys. 221 (2019) 68–77. <https://doi.org/10.1016/j.matchemphys.2018.09.033>.
- [141] H. Liu, J. Liu, X. Li, P. Chen, H. Yang, J. Hao, Effect of heat treatment on phase stability and wear behavior of laser clad AlCoCrFeNiTi0.8 high-entropy alloy coatings, Surf. Coatings Technol. 392 (2020). <https://doi.org/10.1016/j.surfcoat.2020.125758>.
- [142] A. Munitz, S. Salhov, S. Hayun, N. Frage, Heat treatment impacts the micro-structure and mechanical properties of AlCoCrFeNi high entropy alloy, J. Alloys Compd. 683 (2016) 221–230. <https://doi.org/10.1016/j.jallcom.2016.05.034>.
- [143] A. Faraji, M. Farvizi, T. Ebadzadeh, H.S. Kim, Microstructure, wear performance, and mechanical properties of spark plasma-sintered AlCoCrFeNi high-entropy alloy after heat treatment, Intermetallics 149 (2022) 107656. <https://doi.org/10.1016/j.intermet.2022.107656>.
- [144] Q. Li, S. Zhao, X. Bao, Y. Zhang, Y. Zhu, C. Wang, Y. Lan, Y. Zhang, T. Xia, Effects of AlCoCrFeNiTi high-entropy alloy on microstructure and mechanical properties of pure aluminum, J. Mater. Sci. Technol. 52 (2020) 1–11. <https://doi.org/10.1016/j.jmst.2020.04.008>.
- [145] K. Luo, S. Liu, H. Xiong, Y. Zhang, C. Kong, H. Yu, Mechanical Properties and Strengthening Mechanism of Aluminum Matrix Composites Reinforced by High - entropy Alloy Particles, Met. Mater. Int. 28 (2022) 2811–2821. <https://doi.org/10.1007/s12540-021-01159-4>.
- [146] Y. Liu, G. Zheng, The Design of Aluminum-Matrix Composites Reinforced with AlCoCrFeNi High-Entropy Alloy Nanoparticles by First-Principles Studies on the Properties of Interfaces, (2022). <https://doi.org/https://doi.org/10.3390/nano12132157>.
- [147] Y. Liu, J. Chen, J. Liu, P. Zhang, Y. Wang, Core-shell structure mediated microstructure and mechanical properties of high entropy alloy CoCrFeNi / Al composites, Vacuum 192 (2021) 110454.

[https://doi.org/10.1016/j.vacuum.2021.110454.](https://doi.org/10.1016/j.vacuum.2021.110454)

- [148] K.S. Prakash, P.M. Gopal, M. Purusothaman, M. Sasikumar, FABRICATION AND CHARACTERIZATION OF METAL-HIGH ENTROPY ALLOY COMPOSITES, *Int. J. Met.* (2019). <https://doi.org/10.1007/s40962-019-00383-4>.
- [149] C. Gao, Q. Wang, M. Wei, H. Fan, L. Zhao, Y. Wei, Q. Ma, Effects of Reinforcement Volume Fraction on Mechanical Properties and Microstructures of 7075Al Matrix Composites Reinforced by FeCoCrNiAl High-Entropy Alloy Particles, *Metals (Basel)*. 12 (2022). <https://doi.org/10.3390/met12050851>.
- [150] I. Basu, J. Th, M. De Hosson, Strengthening mechanisms in high entropy alloys : Fundamental issues, *Scr. Mater.* 187 (2020) 148–156. <https://doi.org/10.1016/j.scriptamat.2020.06.019>.
- [151] N. Srivastava, G.P. Chaudhari, Strengthening in Al alloy nano composites fabricated by ultrasound assisted solidification technique, *Mater. Sci. Eng. A* 651 (2016) 241–247. <https://doi.org/10.1016/j.msea.2015.10.118>.
- [152] H. Su, W. Gao, Z. Feng, Z. Lu, Processing, microstructure and tensile properties of nano-sized Al<sub>2</sub>O<sub>3</sub> particle reinforced aluminum matrix composites, *Mater. Des.* 36 (2012) 590–596. <https://doi.org/10.1016/j.matdes.2011.11.064>.
- [153] J. Zhu, W. Jiang, G. Li, F. Guan, Y. Yu, Z. Fan, Microstructure and mechanical properties of SiCnp/Al6082 aluminum matrix composites prepared by squeeze casting combined with stir casting, *J. Mater. Process. Technol.* 283 (2020) 116699. <https://doi.org/10.1016/j.jmatprotec.2020.116699>.
- [154] W. Jiang, Z. Fan, Y. Dai, C. Li, Effects of rare earth elements addition on microstructures, tensile properties and fractography of A357 alloy, *Mater. Sci. Eng. A* 597 (2014) 237–244. <https://doi.org/10.1016/j.msea.2014.01.009>.
- [155] J. Liu, Z. Liu, Z. Dong, X. Cheng, Q. Zheng, J. Li, S. Zuo, Z. Huang, Y. Gao, J. Xing, Q. Han, On the preparation and mechanical properties of in situ small-sized TiB<sub>2</sub>/Al-4.5Cu composites via ultrasound assisted RD method, *J. Alloys Compd.* 765 (2018) 1008–1017. <https://doi.org/10.1016/j.jallcom.2018.06.303>.
- [156] Z. Zhang, D.L. Chen, Consideration of Orowan strengthening effect in particulate-reinforced metal matrix nanocomposites: A model for predicting their yield strength, *Scr. Mater.* 54 (2006) 1321–1326. <https://doi.org/10.1016/j.scriptamat.2005.12.017>.
- [157] T. Wang, Z. Chen, Y. Zheng, Y. Zhao, H. Kang, L. Gao, Development of TiB<sub>2</sub> reinforced aluminum foundry alloy based in situ composites - Part II: Enhancing the practical aluminum foundry alloys using the improved Al-5wt%TiB<sub>2</sub> master composite upon dilution, *Mater. Sci. Eng. A* 605 (2014) 22–32. <https://doi.org/10.1016/j.msea.2014.03.021>.
- [158] L. Liu, Y. Wu, H. Gong, S. Li, A.S. Ahmad, A physically based constitutive model and continuous dynamic recrystallization behavior analysis of 2219 aluminum alloy during hot deformation process, *Materials (Basel)*. 11 (2018). <https://doi.org/10.3390/ma11081443>.
- [159] M. Alizadeh, Strengthening mechanisms in particulate Al/B<sub>4</sub>C composites produced by repeated roll

- bonding process, J. Alloys Compd. 509 (2011) 2243–2247. <https://doi.org/10.1016/j.jallcom.2010.11.004>.
- [160] Q. Zhang, D.L. Chen, A model for predicting the particle size dependence of the low cycle fatigue life in discontinuously reinforced MMCs, Scr. Mater. 51 (2004) 863–867. <https://doi.org/10.1016/j.scriptamat.2004.07.006>.
- [161] C.S. Goh, J. Wei, L.C. Lee, M. Gupta, Properties and deformation behaviour of Mg-Y<sub>2</sub>O<sub>3</sub> nanocomposites, Acta Mater. 55 (2007) 5115–5121. <https://doi.org/10.1016/j.actamat.2007.05.032>.
- [162] S.Z. Zhu, D. Wang, B.L. Xiao, Z.Y. Ma, Suppressed negative effects of natural aging by pre-aging in SiCp/6092Al composites, Compos. Part B Eng. 212 (2021). <https://doi.org/10.1016/j.compositesb.2021.108730>.
- [163] R. Gupta, G.P. Chaudhari, B.S.S. Daniel, Strengthening mechanisms in ultrasonically processed aluminium matrix composite with in-situ Al<sub>3</sub>Ti by salt addition, Compos. Part B Eng. 140 (2018) 27–34. <https://doi.org/10.1016/j.compositesb.2017.12.005>.
- [164] F. Chen, Z. Chen, F. Mao, T. Wang, Z. Cao, TiB<sub>2</sub> reinforced aluminum based in situ composites fabricated by stir casting, Mater. Sci. Eng. A 625 (2015) 357–368. <https://doi.org/10.1016/j.msea.2014.12.033>.
- [165] A. Sanaty-Zadeh, Comparison between current models for the strength of particulate-reinforced metal matrix nanocomposites with emphasis on consideration of Hall-Petch effect, Mater. Sci. Eng. A 531 (2012) 112–118. <https://doi.org/10.1016/j.msea.2011.10.043>.
- [166] Z. Yan, D. Wang, X. He, H. Zhang, P. Dong, C. Li, Y. Li, J. Zhou, Z. Liu, L. Sun, Deformation Behaviors and Cyclic Strength Assessment of AZ31B Magnesium Alloy Based on Steady Ratcheting Effect, Mater. Sci. Eng. A (2018). <https://doi.org/10.1016/j.msea.2018.03.023>.
- [167] L.H. Dai, Z. Ling, Y.L. Bai, Size-dependent inelastic behavior of particle-reinforced metal - matrix composites, 61 (2001) 1057–1063.
- [168] S. Jayalakshmi, S. Gupta, S. Sankaranarayanan, S. Sahu, M. Gupta, Structural and mechanical properties of Ni 60 Nb 40 amorphous alloy particle reinforced Al-based composites produced by microwave-assisted rapid sintering, Mater. Sci. Eng. A 581 (2013) 119–127. <https://doi.org/10.1016/j.msea.2013.05.072>.
- [169] S. Dixit, S. Rodriguez, M.R. Jones, P. Buzby, R. Dixit, N. Argibay, F.W. DelRio, H.H. Lim, D. Fleming, Refractory High-Entropy Alloy Coatings for High-Temperature Aerospace and Energy Applications, J. Therm. Spray Technol. 31 (2022) 1021–1031. <https://doi.org/10.1007/s11666-022-01324-0>.
- [170] T.R. Prabhu, M. Arivarasu, Y. Chodancar, N. Arivazhagan, G. Sumanth, R.K. Mishra, Tribological Behaviour of Graphite-Reinforced FeNiCrCuMo High-Entropy Alloy Self-Lubricating Composites for Aircraft Braking Energy Applications, Tribol. Lett. 67 (2019) 1–15. <https://doi.org/10.1007/s11249-019-1193-4>.
- [171] A.E. Afolabi, A.P.I. Popoola, O.M. Popoola, High Entropy Alloys: Advance Material for Landing

- Gear Aerospace Applications, Handb. Nanomater. Nanocomposites Energy Environ. Appl. (2020) 1–27. [https://doi.org/10.1007/978-3-030-11155-7\\_179-1](https://doi.org/10.1007/978-3-030-11155-7_179-1).
- [172] S.T. Mileiko, A new look at the application of metal matrix composites in a future aviation engine, J. Phys. Conf. Ser. 1891 (2021). <https://doi.org/10.1088/1742-6596/1891/1/012029>.
- [173] Y. Yasenchuk, E. Marchenko, G. Baigonakova, S. Gunther, O. Kokorev, V. Gunter, T. Chekalkin, E. Topolnitskiy, A. Obrosov, J.H. Kang, Study on tensile, bending, fatigue, and in vivo behavior of porous SHS-TiNi alloy used as a bone substitute, Biomed. Mater. 16 (2021). <https://doi.org/10.1088/1748-605X/aba327>.
- [174] G.A. dos Santos, The Importance of Metallic Materials as Biomaterials, Adv. Tissue Eng. Regen. Med. Open Access 3 (2017) 1–4. <https://doi.org/10.15406/atroa.2017.03.00054>.
- [175] A. Rashidy Ahmady, A. Ekhlaei, A. Nouri, M. Haghbin Nazarpak, P. Gong, A. Solouk, High entropy alloy coatings for biomedical applications: A review, Smart Mater. Manuf. 1 (2023) 100009. <https://doi.org/10.1016/j.smmf.2022.100009>.

### Declaration of Interests Statement

The authors declare that they have no known competing financial interests or personal relationships that could have appeared to influence the work reported in this paper.